IMBALANCE RESPONSE OF A ROTOR SUPPORTED ON SEALED INTEGRAL DAMPERS

by

Oscar De Santiago
Dr. Luis San Andrés

May 1998

TRC-SFD-1-98

IMBALANCE RESPONSE OF A ROTOR SUPPORTED ON SEALED INTEGRAL DAMPERS

TABLE OF CONTENTS

IMBALANCE RESPONSE OF A ROTOR SUPPORTED ON SEALED INTEGRAL DAMPERS

O. De Santiago and L. San Andrés

EXECUTIVE SUMMARY

High performance turbomachinery demands appropriate means to ensure structural isolation of components and stringent rotor vibration limits with tolerance to sudden imbalance loads due to blade loss events, shock and maneuver actions. Squeeze film dampers (*SFDs*) are the only effective mean to reduce vibrations and to suppress instabilities in high performance aeroengine systems. Integral squeeze film dampers (*ISFDs*) offer distinct advantages such as reduced overall weight and length of the damper structure with less number of parts, accuracy of positioning (centering), and a split segment construction allowing easier assembly, inspection and retrofit than with any other type of damper.

The experimental research program aims to identify the damping coefficients of sealed *ISFDs* from measurements of the imbalance response of a massive rotor supported on two (identical) integral dampers. Experiments are conducted on dampers with end plate seals of known clearance. The amplitudes of synchronous rotor response at the first critical speed, for increasing levels of imbalance, allow the determination of system amplification factors and the evaluation of system damping coefficients. In addition, (coupled) imbalance masses fixed at two rotor planes excite the rotor/bearing conical mode of vibration. Measurements of the rotor synchronous amplitude response at the second critical speed allow the estimation of the system angular damping coefficients.

The detailed measurements, impact tests and imbalance response tests, demonstrate that end gap seals render a substantial increase in the *ISFD* viscous damping coefficients and without a severe penalty in the flow through the dampers. The sealed integral dampers generate viscous damping coefficients larger than two times the values obtained earlier for open ended dampers. Conventional (cylindrical) sealed *SFDs* restrict substantially the through flow and determine minimal increments in the damping coefficients because the lubricant viscosity decreases as the operating film temperature raises. The experiments further demonstrate that the amplitudes of rotor synchronous response at the first and second critical speeds are proportional to the imbalance displacements. No subsynchronous frequencies or (nonlinear) jump phenomenon are ever observed in any of the tests. *FEM* predictions of the viscous damping coefficients for the end sealed *ISFDs* agree favorably with the identified damping coefficients when accounting for the effect of air entrainment in the analysis. The experimental verification and theoretical validation of the damping capability of sealed *ISFDs* demonstrates the benefits of this novel technology for application in high performance turbomachinery.

NOMENCLATURE

A_{df}	Amplitudes of rotor responses at the drive and free end planes at the second critical speed
A_x	Fast Fourier transform of acceleration $\ddot{x}(t)$
B	Squeeze film damper bearing parameter
c	*ISFD* radial clearance [0.229 mm, 0.009 in]
c_s	*ISFD* end seal clearance [0.127, 0.102, 0.076 mm, 0.005, 0.004, 0.003 in]
C	System damping coefficient for the cylindrical mode [N-s/m (lbf-s/in)]
C_θ	System angular damping coefficient for the conical mode [N-m-s/rad (lbf-in-s/rad)]
C_R	Rotational system damping coefficient [N-m^2 (lbf-in^2)]
C_{dry}	Dry or structural system damping coefficient [N-s/m (lbf-s/in)]
Cc	System critical damping [N-s/m (lbf-s/m)]
Cc_θ	System angular critical damping [N-m-s/rad (lbf-in-s/rad)]
C_L	Local end seal coefficient [(m^2/s)/Pa]
$\overline{C}_L$	Local end seal coefficient empirical correction factor
d	Inlet orifice port diameter [1.59 mm (0.063 in)]
$d_{1,2}$	Distance from rotor cg to drive end and free end disks [66.73, 101.9 mm (2.613, 4.012 in)]
d_{df}	Distance between drive and free end measurement planes [266.7 mm (10.5 in)]
$d_{D,F}$	Distance from rotor cg to bearing supports centerline. Drive end, Free end.[189.4, 217.0 mm (7.457, 8.543 in)]
e	Rotor orbit amplitude [m (in)]
f	Frequency ratio ω/ω_n
F	Excitation force [N (lbf)]
$\mathcal{F}$	Fast Fourier transform of excitation force $F(t)$
H	Transfer function of displacement/load (dynamic flexibility) [m/N (in/lbf)]
H_{acc}	Transfer function of acceleration/load (accelerance) [N-m/s^2 (lbf-in/s^2)]
I_p	Rotor polar moment of inertia [0.286 Kg-m^2 (979.4 lbm-in^2)]
I_t	Rotor modal mass moment of inertia for second mode of vibration [0.624 Kg-m^2 (2,136 lbm-in^2)]
j	$\sqrt{-1}$
J_{xx}	$= m_1 d_1 r_1 + m_2 d_2 r_2$ .Excitation cross moment of inertia from coupled imbalance masses [Kg-m^2 (lbm-in^2)]
$K_{V,H}$	System stiffness coefficients for the first, cylindrical mode of vibration [N/m, (lbf/m)]
$K_{V2,H2}$	Supports effective stiffness coefficient for the second mode of vibration, vertical and horizontal [N/m, (lbf/m)]
l	Inlet orifice port length [11.8 mm (0.465 in)]
l_s	End seal radial length [3.0 mm (0.118 in)]
L	Damper land axial length [23.0 mm (0.910 in)]
L_s	Empirical correction factor for the flow through the sealed *ISFDs*
m	Imbalance mass attached to rotor middle disk [gr.]
$m_{1,2}$	Imbalance masses attached to rotor drive and free end disks [gr.]
M	Rotor modal mass for the first mode of vibration [45.22 kg, 99.7 lbm]
P_a	Ambient pressure [Pa, (psi)]
P_s	Lubricant supply pressure to the bearing housings [Pa, (psi)]
P_{cav}	Lubricant cavitation pressure [Pa, (psi)]
Q	System amplification factor at rotor first critical speed
Q_θ	System amplification factor at rotor second critical speed
$Q_{pad\ open}$	Pad flow through open ended *ISFD* [m^3/s, (gpm)]
$Q_{pad\ sealed}$	Pad flow through sealed *ISFD* [m^3/s, (gpm)]
$Q_{ISFD\ open}$	Overall flow through open ended *ISFD* [m^3/s, (gpm)]
$Q_{ISFD\ sealed}$	Overall flow through sealed *ISFD* [m^3/s, (gpm)]
r	Rotor middle disk radius for location of imbalance masses [114.3 mm (4.5 in)]
$r_{1,2}$	Rotor drive and free end disks radii for location of imbalance masses [114.3, 95.25 mm (4.5, 3.75 in)]
R	*ISFD* journal radius [48.26 mm (1.9 in)]
$R_{pad\ open}$	Pad flow resistance of open ended *ISFD* [Pa-s/m^3]

$R_{pad\ sealed}$	Pad flow resistance of sealed *ISFD* [Pa-s/m^3]
$R_{ISFD\ open}$	Total flow resistance of open ended *ISFD* [Pa-s/m^3]
$R_{ISFD\ sealed}$	Total flow resistance of sealed *ISFD* [Pa-s/m^3]
R_o	Flow resistance of the inlet orifice port [Pa-s/m^3]
t	Time (sec)
u	$= m \bullet r/M$, Imbalance distance [m (in)]
x, y, z	Cartesian coordinates
X	Amplitude of rotor vibration [m (in)]
β	Coupled imbalance angle of excitation [°, rad]
β_{eff}	$= \beta - \beta_o$ Effective couple imbalance angle of excitation [°, rad]
β_o	Remnant couple imbalance angle of excitation [°, rad]
$\chi(\omega)$	Fast Fourier transform of time response $x(t)$
γ	Pad arc length [52°, 0.908 rad]
ΔP	Total pressure drop across *ISFD* [Pa (psi)]
ΔP_0	Pressure drop across *ISFD* land [Pa (psi)]
μ	Lubricant viscosity [Pa-s]
θ	Angle of rotor response to coupled imbalance [°, rad]
τ	System time constant [sec]
ω	Frequency of excitation force and synchronous with rotor speed [rad/s]
ω_n	Rotor bearing system natural frequency [rad/s]
ξ	System damping ratio
ξ_θ	Angular system damping ratio

Subscripts

i	Direction of subindexed variable (vertical or horizontal)
V, H	Vertical, horizontal direction
max	Maximum value of subindexed variable
θ	Refers to angular (conical mode) rotor motions

LIST OF TABLES

LIST OF FIGURES

INTRODUCTION

Squeeze film dampers (*SFDs*) reduce rotor vibration and load transmissibility in rotating machines allowing smooth operation and enhanced performance. A squeeze film damper consists of a cylindrical housing and an inner journal separated by a thin lubricant film filling the small annular clearance. A rolling element bearing connects the rotor and the journal allowing for rotor spin, and a locking pin or elastic support prevents the journal from rotation. The elastic support provides structural stiffness and allows for rotor centering within the annular gap. As the rotor spins, centrifugal forces due to machine imbalance or other sources drive the rotor into a whirling (vibratory) motion that produces a squeezing action in the lubricant film. Hydrodynamic pressures generate reaction forces and fluid viscous shear stresses dissipate energy to dampen the journal motions. Force transmissibility into the support foundation is also reduced, resulting in a smoother rotor operation. Several operating conditions and design parameters affect the performance of *SFDs*. The *SFD* geometry (diameter, length, and film clearance), the lubricant viscosity, feeding and discharge grooves, type of end seals, levels of supply pressure, fluid inertia, and the extent and type of lubricant cavitation affect the dynamic forced response of *SFDs* (Zeidan, et al., 1996).

The most commonly employed *SFD* design (here after referred as a conventional *SFD*) incorporates a squirrel cage as the elastic structural support. The most distinctive feature of this damper configuration is the relatively large axial space required for the elastic support in comparison to the damper hydrodynamic length. Squirrel cages often require three to four times as much space as the *SFD* (De Santiago, et al., 1997).

Wire electrical discharge machining (EDM) enables the manufacturing of integral squeeze film dampers (*ISFDs*). These dampers, as shown in Figure 1, are comprised of several segmented pads instead of a cylindrical journal. Thin structured webs attach the inner and outer rings and perform the function of elastic supports. The thin gap between the pads and the outer ring forms the squeeze film lands. Each pad can be manufactured with a different clearance to counter the static deflection due to rotor weight. *ISFDs* have been applied successfully in the petrochemical industry as retrofit components adding more damping to (nearly) unstable rotor / bearing system (Zeidan, 1995). *ISFDs* may develop less damping than similar size conventional *SFDs* due mainly to the reduced area of the film pads decreasing the circumferential film extent. End seals restricting the axial flow through the film lands dampers provide the means to increase the damping coefficients by raising the hydrodynamic pressure in a pad film land.

The present experimental research programs aims to determine the damping coefficients of sealed *ISFDs* from measurements of the imbalance response of a massive rotor supported on this type of compact damper. Experiments are conducted on dampers with end gap plate seals of known clearance. The amplitudes of synchronous rotor response at the first critical speed, for increasing levels of imbalance, allow the determination of system amplification factors and the identification of system damping coefficients.

In addition, (coupled) imbalance masses fixed at two rotor planes excite the rotor/bearing conical mode of vibration. Measurements of the rotor synchronous amplitude response at the second critical speed allow the estimation of the system angular damping coefficient. The experiments evaluate the effectiveness of *ISFDs* in attenuating the rotor/bearing system response for both cylindrical and conical modes of vibration.

The integral damper force coefficients are estimated from the experimental system damping coefficients less the structural (remnant) damping coefficients determined earlier from rap tests on the rotor and without lubricant in the film lands. The test damping coefficients are compared with predictions from a finite element method (*FEM*) computational analysis. The experimental verification of the damping capacity of the sealed *ISFDs* aims to further the application of this novel technology to high performance turbomachinery.

A Brief Review of the Literature

Mohan and Hahn (1974) provide design charts for the response of rigid rotors supported on centralized open-ended *SFDs*. A nonlinear theoretical model for the rotor-*SFDs* demonstrates the likeliness of different modes of operation of the rotor-bearing system above the system natural frequency as determined by the magnitude of rotor imbalance and rotational speed. Rotors supported on *SFDs* can operate with large (uninverted mode) or small (inverted mode) stable orbits. The inverted mode is associated with low force transmissibility and is the desired design goal. However, sudden jumps from small to large orbits or vice-versa, depending on the rotor acceleration, are likely to occur in *SFDs* with lubricant cavitation, i.e. without a full film. Sufficiently large rotor imbalances can cause this highly nonlinear behavior and with the consequent increase in force transmissibility and reduction in the life of the rolling bearing elements. Nonsynchronous orbits with violent journal excursions (high eccentricity) are also a possibility for rotor-*SFDs* with very little damping. The literature indicates that a bearing parameter[1], $B = \frac{\mu R}{2M\omega}\left(\frac{L}{c}\right)^3$, must be on the order of 10^{-2} for this phenomenon to occur. Thomsen and Andersen (1974) present an experimental parametric study of a vertical rotor supported on *SFDs*. The experiments show that the damping coefficient is independent of the journal instantaneous position for orbits smaller than 25% of the radial clearance. Tonnessen (1976) studies the effects of oil supply pressure and journal static eccentricity on the *SFD* forced response. In general, increasing oil supply pressure brings a beneficial effect to rotor response (i. e. increase in effective damping) by reducing the lubricant

[1] B is defined by the lubricant viscosity (μ), the journal radius (R), the rotor mass (M) taken by the *SFD*, the synchronous whirl frequency (ω), the film length (L), and the damper radial clearance (c).

cavitation extent in the *SFD* film circumference. Predictions of damping coefficients from a linearized model are good relative to the experiments for small amplitude orbits about the journal static position.

Vance and Kirton (1975) report tests performed with piston-ring type sealed *SFDs* and compare experimental pressure measurements with the long-bearing solution of the Reynolds equation. The model fails to properly predict the amplitude of the squeeze film pressure, although the shape of the pressure wave is well represented. This difference is attributed primarily to the fact that the long-bearing model does not allow for variations of pressure along the axial direction thus preventing a realistic boundary condition for the end seals leakage restriction.

Marmol and Vance (1978) introduce a finite difference analysis of the squeeze film flow, which allows for more adequate boundary conditions. Theoretical results are presented for three different types of end seals: piston ring seals, radial O-rings and axial face O-rings[2]. With the finite different analysis, predictions with prior experimental data improve considerably (Jones (1973), Vance and Kirton (1974), Feder, et al. (1977), and Botman (1976)). However, the complexity of the method is suitable mainly for computerized calculations.

Dede, et al. (1986) introduce side leakage factors to model end-plate seals and develop closed-form expressions for the circumferential pressure distribution from which *SFD* damping forces are calculated. Dede, et al. also present experimental results for a cylindrical (360° land) damper with end-plate type seals. The end seals increase the pressure field within the damper land by restricting the axial flow (i.e. reducing the exit area at the film land ends), thus conducting to a raise in the damping forces. Experiments reveal an effective increase in damping forces for sealing gaps smaller than one half of the damper radial clearance. A shortcoming of the analysis is that the leakage factor cannot be readily inferred from the end seal geometry.

San Andrés and Vance (1984) introduce local end seal coefficients directly related to the seal geometry characteristics. End plate seals, piston ring type seals and other complex geometries are included in the analysis. These coefficients allow the specification of appropriate boundary conditions to the Reynolds equation. However, the end seal coefficients may still need of empirical correction factors which require calibration to experimental results.

The forces developed by the oil film determined the dynamic performance of *SFDs*. Theoretically these forces are highly nonlinear functions of the instantaneous journal eccentricity (Mohan and Hahn, 1974). Linearization of *SFD* forces about a fixed journal position is often useful for rotor-bearing system stability predictions.

Several test methodologies for estimation of *SFD* force coefficients are currently in use and cover specific needs and purposes. Measurements of system synchronous response to calibrated imbalances in rotor/bearings supported on *SFDs* is one of the most popular (and simplest) types of tests for the estimation of the system effective damping coefficient. These measurements can also be conducted in

[2] Axial face O-rings do not support the weight of the rotor, and consequently, are less prone to show permanent deformation and sag.

actual rotor-bearing systems and allow the rapid identification of bearing parameters for design or response verification purposes.

Thomsen and Andersen (1974) extract damping coefficients of open ended, spring-centered *SFDs* from measurements of the transmitted structural force and the velocity of the damper sleeve in a test rig excited by imbalance weights fixed in the rotor midspan disc. Experiments show that the damping coefficient is constant for damper journal amplitudes less than 25% of the radial clearance. The test results correlate well with a full (2π) film model. However, the analytical results underpredict largely the measured damping coefficients for larger journal orbital motions, in spite of the likelihood of lubricant cavitation in the test *SFD*.

Rotordynamic analysis coupled with simplified hydrodynamic lubrication models predict the possibility of multiple-valued rotor response regions when the lubricant cavitates (vapor or gasous) due to the squeeze film action. Simandiri and Hahn (1979) describe a pivot type test rig consisting of a massive rigid rotor supported by an open-ended *SFD* in one end and a self-aligning ball bearing on the opposite end. Experimental rotor responses confirm predictions of the journal amplitude of motion and the eventual occurrence of the rotor orbit jump phenomena. Here, steady orbits suddenly resize at certain characteristic speeds and under specific operating conditions, mainly increasing imbalances.

Classical hydrodynamic lubrication theory also predicts that *SFD* film forces grow unbounded for journal eccentricities near the film land clearance. Chu and Holmes (1996) present a study on the response of a flexible rotor supported on *SFDs*. Imbalance response curves show that the critical speeds relocate when the amount of imbalance produces large rotor orbits. The shift of the critical speeds is attributed to the large *SFD* cross-coupled damping coefficient acting as a hardening stiffness on the rotor/bearing system.

Kuzdzal and Hustak (1996) describe a flexible rotor supported on *SFDs* test rig to represent the rotordynamics of a commercial compressor application. Different *SFD* configurations are investigated, namely O-ring centered-dampers, spring centered-dampers, and bottom resting dampers. Measured rotor amplification factors at the first critical speed from rotor imbalance responses aid to evaluate the *SFDs* dynamic forced performance. The experiments show that off-centered dampers attenuate the rotor response more than centered dampers thus validating theoretical predictions. However, off-centered dampers are unable to adequately suppress subsynchronous vibrations induced by external elements, including fluid film seals and aerodynamic forces. The tests also demonstrate that excessive damping can "lock-up" the bearings and produce large orbits at the midspan of the flexible rotor.

San Andrés and Lubell (1997) perform experiments in a three-disk rigid rotor supported on conventional open ended *SFDs*, and report damping force coefficients estimated from the amplitude of synchronous rotor response at the first system critical speed. Contrary to the observations by Chu and Holmes (1996), the experimental measurements show the rotor amplitude of motion to be nearly proportional to the amount of imbalance, rendering nearly uniform damping coefficients for rotor orbit motions up to 50% of the clearance. The tests show the absence of any rotor jump phenomena. San

Andrés and Lubell stress the importance of an adequate identification of the structural damping and bearing support stiffness coefficients for the appropriate estimation of the *SFD* force coefficients from imbalance response measurements.

Murphy, et al. (1996) implement integral *SFDs* in a compensated pulsed alternator (compulsator) rotor. The supports design requirements demand specific stiffness and damping coefficients, in addition to tight restrictions in the axial space available. The four-pad damper utilizes *L*-shaped thin beams as the structural support elements. The measured damper stiffness differs considerably from the design stiffness, the first one being eight times larger than the desired value. The rotor-bearing system presents a satisfactory linear response with no jumps although critical speeds relocate due to the difference in stiffness.

De Santiago, et al. (1997) identify the damping coefficients of open ended *ISFDs* from measurements of rotor synchronous imbalance responses and utilizing the same test rig used by San Andrés and Lubell (1997). Static and dynamic measurements of the integral damper stiffness elements verify the design values. The tests demonstrate that the synchronous response of the rotor-integral *SFD* is linear and nearly proportional to the amount of imbalance for rotor amplitudes as large as 75% of the damper radial clearance. The rotor response is also free of any jump or subsynchronous vibrations. Correlations of theoretical and experimental *ISFD* damping coefficients show a reasonable agreement. The novel technology of *ISFDs* requires of further measurements to quantify the effects of end gap seals on the damper flow rate and the increase of the viscous damping coefficient.

DESCRIPTION OF TEST RIG AND MAJOR SYSTEM COMPONENTS

Figure 2 shows a schematic side view of the test apparatus and the foundation where the rotor/bearings assembly rests. The test apparatus consists mainly of a base plate, two identical support housings, a test rotor, a driving motor and a flexible coupling. The test rotor consists of a steel rigid shaft with a diameter of 76.2 mm (3.0 in) and 673 mm (53.0 in) long. Three disks 25.4 mm (1 in) thick are press-fitted in the shaft. The total rotor mass, including the shaft and the disks, is 41.7 kg (91.8 lb). The disks are equally spaced (63.5 mm, 2.5 in) and the middle disk is located at the midpoint of the bearing span. The two disks close to the drive end are 279.4 mm (11 in) in diameter while the free end disk is 228.6 mm (9 in) in diameter. The bigger disks have twelve equally spaced threaded holes at a radius (r) equal to 114.3 mm (4.5 in) for installation of imbalance masses and the smallest disk also has twelve threaded holes but at a radius of 95.25 mm. The bearing span is equal to 406 mm (16 in). The precision ball bearings are installed with interference fit at the shaft's bearing races of diameter equal to 25 mm (0.984 in). The rotor and *ISFDs*, once installed on the shaft, become a single unit. Figure 3 depicts the test rotor and its main dimensions.

The support housings are split horizontally for easiness in the rotor installation. The housings have a centered slot into which the dampers fit. The external shape of the dampers creates a plenum chamber for oil supply after installation of the rotor into the supports. Oil enters each damper housing at one of its sides and drains at the bottom of the housing back into the reservoir. Axial holes in the housings allow accurate alignment of both supports using precision straight bars. Flexible hoses fixed to the housing inner race replace lip elastomeric seals and exert a minimal influence on the dynamic rotor response.

A 7.5 kW (10 hp) DC variable speed motor drives the test rotor. A power supply feeds current to the driving motor to a top speed of 10,000 rpm. An isolated steel base resting on the foundation table supports the motor, and a flexible coupling connects the motor to the test rotor. A drawn cup roller clutch drives the rotor in one direction only, and allows the rotor to decelerate freely when disconnected from the motor. Similar rates of rotor deceleration are obtained in different tests as will be shown later.

The test apparatus (including the driving motor and a safety cover) lays on a desktop steel plate that is part of a concrete base supported by four structural columns. The base plate, supporting the housings and the rotor, rests on a vibration isolation pad and is bolted to the foundation by four rods of 12.7 mm (0.500 in) in diameter. A steel box covering the rotor and components is attached to the base table. The cover reduces noise, prevents oil from leaking out of the apparatus, and provides protection when the test rig is operating. A cooling air jet dissipates heat from the coupling in the roller clutch region, thereby extending the life of the mechanical elements. The air jet also avoids localized rotor overheating due to the sliding friction in the rolling clutch near the coupling. The structural legs of the base table rest on a 12.7 mm (0.500 in) plate and is separated from the laboratory floor by a rubber pad for vibration isolation.

The lubrication system depicted in Figure 4 contains a variable speed main pump, a 150-lt. (40-gal) oil reservoir, 19.1 mm (0.750 in) hydraulic lines, flowmeters and pressure gauges. A relief valve limits the

maximum pressure of the lubrication system. Valves directing the flow towards the return line serve to control the feed pressure. A turbine-type flow meter displays the overall flow going into the dampers, and a second flow meter shows the amount of lubricant entering the drive end damper. Pressure gauges connected to the bearing feeding grooves indicate the lubricant pressure at the plenum chamber inside the bearing housings. A return pump sends the oil from the housings back into the reservoir. An electric heater and a forced-air cooler are available to keep the lubricant at a preset temperature as needed. An ISO VG 10 lubricant is employed in all tests.

The integral dampers consist of a journal supported by eight structural *S*-shaped thin webs grouped in four pairs as shown in Figure 5. Precision rolling element bearings are installed on the inner race of the journal. The structural webs, manufactured by the EDM method, are attached to the outer ring of the damper thus forming a single unit with the journal and the outer ring. The springs are designed to provide a damper radial stiffness of 3.506 MN/m (20,000 lbf/in). The design value has been verified by both static and dynamic force measurements (see De Santiago, et al. 1997).

Four identical pads, 52° in extent, form the squeeze film land between the journal and the outer ring. The pads clearance are manufactured unevenly so that the overall radial clearance (c) becomes 0.229 mm (9 mils) after the springs deform statically under the rotor weight. The pad arc radius (R) is 48.26 mm (1.900 in) and the damper land axial length (L) is 23.0 mm (0.910 in). A feeding groove in the outside of the damper ring forms a plenum chamber. The damper has four equally spaced radial orifices at the damper axial middle plane. The holes' diameter (d) is equal to 1.59 mm (0.063 in) and length (l) equal to 11.8 mm (0.465 in). The orifices serve as lubricant inlet ports to the squeeze film lands. Each side of the outer damper ring has six threaded holes for installation of end plate seals. These seals consist of two semi-circular plates attached to both sides of the damper outer ring and restricting the axial flow coming out from the film lands. Calibrated stock shims with the same shape as the end plates provide the end seal gap (see Figure 6).

Instrumentation and Data Acquisition System

The test apparatus is instrumented to measure the rotor response at three axial locations (drive end, midspan, and free end) and in two orthogonal directions (vertical and horizontal). Six displacement eddy-current sensors measure the rotor displacements and two accelerometers measure the bearing supports motion. The accelerometers are located at different positions (vertical or horizontal), depending on the test conducted. An optical keyphasor pointing to the coupling generates electric pulses for the tachometer and serves as a reference for measurements of rotor phase angle. Type-K thermocouples measure the temperature of the oil at the reservoir, the damper pad exits, and the motor and ambient temperatures.

Three oscilloscopes in a control rack display the orbits described by the rotor at the three axial locations (drive end, free end, and midspan) and another oscilloscope displays the supports accelerations. A two-channel frequency analyzer displays the power frequency spectrum of a selected signal (either

displacement or acceleration) for the duration of a test. An ad-hoc console contains the controls for the pumps and the preset lubricant temperatures, and also displays the measured temperatures and rotor speed.

A Bently Nevada ADRE V2.2 for Windows software and an eight channel data acquisition interface unit displays and records the (6) rotor displacements, the (2) bearing supports' accelerations, and the (1) rotor speed during the rotor coast down. After a test is finished, the acquisition system creates a database with the test information. Analysis tools are available such as bode plots, cascade and waterfall plots, polar plots, orbit display at any speed, and time waveform plots. The acquisition system is able to compensate the rotor response for shaft runout (slow roll vector) as well as for remnant imbalance at every rotor speed. The synchronous rotor response represents the isolated effect of the imbalance mass after the vector compensation, and it allows the estimation of the system damping coefficients as described later. The assumption of equal contribution of both dampers acting in parallel together with previously identified structural damping coefficients permits the identification of the damping coefficients for each integral damper.

EXPERIMENTAL PROCEDURES FOR THE IDENTIFICATION OF SYSTEM PARAMETERS

Identification of System Damping Coefficients from Impact Response Tests

Measurements of rotor dynamic response to sudden loads (impacts) and periodic loads (as those resulting from the centrifugal force due to the imbalance in a rotating structure) can be utilized for identification of the mass, stiffness and damping parameters of a mechanical system.

Impact response measurements on a stationary rotor are hereby employed to identify the system damping coefficients generated by the lubricant film in the integral dampers. The impact load tests are conducted for a dry condition, i.e. without lubricant flowing through the dampers, and for lubricant flow condition at an operating supply pressure (P_s) equal to 68.7 kPa (10 psig). The dry impact tests serve to estimate the structural system damping coefficients acting in parallel with the viscous damping coefficients generated by the oil film in the dampers.

Figure 7 depicts the test set-up and instrumentation employed for the impact response measurements. An impact hammer with an integral piezoelectric load cell is used to rap the test rotor at a location near its center of gravity cg, i.e. the rotor middle disk, so as to excite the cylindrical fundamental mode of vibration. A small piezoelectric accelerometer fixed in the opposite side of the middle disk measures the rotor acceleration resulting from the impact. The load cell and the accelerometer amplified signals are input into a signal analyzer which performs the fast Fourier transform (FFT) of both signals and renders the transfer function of acceleration/load in the frequency domain.

The impact response measurements indicate that the rotor motion could be analyzed as a simple rigid mass resting on elastic supports and without cross-coupling effects in the two planes of vibration. The equation of motion defining the dynamic response of a single degree of freedom system is:

$$M\ddot{x} + C\dot{x} + Kx = F(t) \tag{1}$$

where $F(t)$ is an excitation force, $x(t)$ is the time response, and M, C, and K are the system mass, damping and stiffness coefficients, respectively. For the present tests, $F(t)$ is an impact from a calibrated hammer able to excite a range of frequencies determined by the stiffness of the contacting surfaces and the mass of the impact hammer head (Ewins, 1986).

The system transfer function of displacement over load or *dynamic flexibility*, $H(\omega)$, is equal to :

$$H(\omega) = \frac{\chi(\omega)}{\mathcal{F}(\omega)} = \frac{1}{K - M\omega^2 + jC\omega} \tag{2}$$

where $\chi(\omega)$ and $\mathcal{F}(\omega)$ represent the Fast Fourier Transforms of the time response, $x(t)$, and applied external load, $F(t)$, respectively, and $j = \sqrt{-1}$. At a frequency (ω) equal to the system undamped natural frequency, $\omega_n = (K/M)^{1/2}$, the dynamic flexibility reduces to

$$H(\omega_n) = \frac{1}{jC\omega_n} \tag{3}$$

From this expression, the system damping coefficient (C) is obtained as:

$$C = \left| \frac{1}{jH(\omega_n)\omega_n} \right| \tag{4}$$

The acceleration $\ddot{x}(t)$ time response to the excitation load is used in the current experiments. Let $A_x = FFT(\ddot{x}(t))$. The acceleration and displacement are related in the frequency domain by:

$$A_x(\omega) = \omega^2 \chi(\omega) \tag{5}$$

The system transfer function of Acceleration/Load, $H_{acc}(\omega)$, also known as inertance or accelerance, is related to the dynamic flexibility $H(\omega)$ by:

$$H(\omega) = \frac{1}{\omega^2} H_{acc}(\omega) \tag{6}$$

and the system damping coefficient is estimated from a combination of equations (4) and (6) as:

$$C = \left| \frac{\omega_n}{jH_{acc}(\omega_n)} \right| \tag{7}$$

In the procedure detailed, independent impacts are imparted in two orthogonal directions, the system transfer functions are obtained, and the damping force coefficients are identified for motions in the vertical and horizontal directions. First, *dry* damping coefficients are estimated for the system without lubricant. Next, *wet* damping coefficients are obtained for lubricant flowing through the *ISFD* and at increasing oil temperatures. The viscous damping coefficients from the integral dampers are obtained by

subtraction of the *dry* damping coefficients from the *wet* damping coefficients, representing the overall system damping.

In general, the force coefficients from a viscous fluid film damper are functions of the instantaneous journal eccentricity. Thus when the rotor is at rest, as in the impact tests, the smallest values of damping coefficients are expected. Values of damping coefficient estimated from imbalance tests are usually larger because the rotor executes motions away from the static (centered) equilibrium position.

Identification of System Damping Coefficients from Measurements of Rotor Imbalance Responses

Gyroscopic effects become important as the rotor spins, and their influence increases with rotational speed. It is difficult to account for these additional effects directly from simple impact tests measurements. Thus, imbalance response measurements in which the rotor actually spins and traverses critical speeds provide a better technique for evaluation of the system damping coefficients under operating conditions.

Measurements of rotor displacements in the vertical and horizontal directions at the rotor-bearing system first critical speed allow identification of the system damping coefficients. The measurements demonstrate that the fundamental mode of vibration is cylindrical and corresponding closely to motions of a rigid rotor supported on the damper elastic webs and bearing supports. The vertical (V) and horizontal (H)motions, $x_V(t)$ and $x_H(t)$, can be described by the linear governing equation of motion:

$$M\ddot{x}_i + C_i\dot{x}_i + K_i x_i = Mu\omega^2 e^{j\omega t} \quad ; i = V,H \tag{8}$$

where M is the rotor modal mass, and (C_i , K_i) are the corresponding modal damping and stiffness coefficients, u is the imbalance distance, and ω is the frequency of the excitation force and synchronous with the rotor speed. The fundamental theory of linear vibrations establishes the relationship between the amplitude of the response X_i and the excitation as:

$$X_i = \frac{u f_i^{\,2}}{\left[(1-f_i^{\,2})^2 + (2\xi_i f_i)^2\right]^{\frac{1}{2}}} \quad ; i = V,H \tag{9}$$

where f_i is the frequency ratio ω/ω_{n_i}, and ξ_i is the system damping ratio $\dfrac{C_i}{2\sqrt{K_i M}}$.

For sufficiently small damping ratios the resonance peak amplitude occurs near the system natural frequency ($f \approx 1$). Thus, at this frequency the rotor amplitude of vibration $(X_i)_{max}$ can be written as:

$$(X_i)_{max} = \frac{u}{2\xi_i} \quad at \quad \omega = \omega_{n_i} \tag{10}$$

and,

$$\xi_i = \frac{u}{2(X_i)_{max}} \tag{11}$$

The ratio $(X_i)_{max}/u$ is known as the amplification factor Q_i; and the damping ratio ξ_i is estimated as:

$$\xi_i = \frac{1}{2Q_i} \tag{12}$$

A more precise expression when accounting for the shift in the critical speed due to the influence of damping is given by:

$$\xi_i^2 = \frac{-1 \pm \sqrt{1 + 1/Q_i^2}}{2} \qquad (13)$$

The system damping coefficient is then readily estimated since the rotor-bearing system properties are known,

$$C_i = Cc_i \xi_i \quad ; \quad i = V, H \qquad (14)$$

where the system critical damping Cc_i is:

$$Cc_i = 2\sqrt{K_i M} \qquad (15)$$

for the fundamental (cylindrical) mode of vibration.

The effective viscous damping coefficient from the *ISFDs* is estimated by subtracting the structural damping coefficient, identified by dry impact tests, from the system damping coefficient ($C_{V,H}$). In addition, for the first mode of vibration, each support is assumed to contribute equally to the system damping coefficient. The nearly identical amplitudes of motion measured at the three positions (drive end, near middle disk and free end) along the rotor verify this assumption. Thus, each integral damper contributes with one half of the total effective damping coefficient. The identified values of the effective damping coefficient in each *ISFD* are further compared with predictions from a finite element method (*FEM*) program.

Simple Flow Models for the Integral Dampers

Measurements of oil flow through the *ISFDs* for different levels of supply pressure are performed for the open ended and the sealed configurations when the rotor is at rest (zero speed). These measurements are useful in determining the flow requirements from the lubrication system, and can also be used to estimate the amount of heat that the lubricant can remove from the damper under operating conditions.

The amount of lubricant leaving the *ISFD* is estimated from the static pressure distribution in the film lands. The simple model considers an incompressible lubricant of uniform density and viscosity, and the flow as laminar, inertialess and adiabatic. Two different pressure distributions in the film lands of an arcuate squeeze film pad are assumed for the open ended and the sealed ends configurations, respectively (Figure 8). In the open ended configuration, the flow is mainly axial and the pressure distribution from the pad middle plane to the exit sides is as shown in Figure 8(a). The expressions for the pad flow ($Q_{pad\ open}$) and the pad flow resistance ($R_{pad\ open}$) are given by:

$$Q_{padopen} = \frac{c^3 R \gamma}{6 \mu L} \Delta P_D \qquad R_{padopen} = \frac{6 \mu L}{c^3 R \gamma} \qquad (16)$$

where ΔP_D is the pressure drop across the damper land, c is the radial clearance (0.229 mm , 9 mils), μ is the lubricant viscosity, R is the journal radius (48.26 mm, 1.900 in), γ is the pad arc extent (0.907 rad, 52°), and L is the pad axial length (23.0 mm ,0.910 in). The feeding orifices are modeled as a capillary

tube since the flow is laminar at low Reynolds numbers. Accounting for the pressure drop across the inlet orifices, the overall flow through an *ISFD*, ($Q_{ISFDopen}$), is

$$Q_{ISFDopen} = \frac{\Delta P}{R_{ISFDopen}} \tag{17}$$

where ΔP is the total pressure drop, and equal to the feed pressure minus the ambient pressure. The overall flow resistance, $R_{ISFDopen}$ is:

$$R_{ISFD\,open} = \frac{R_o + R_{padopen}}{4} \tag{18}$$

where R_o is the orifice resistance,

$$R_o = \frac{128\mu l}{\pi d^4} \tag{19}$$

where (l) and (d) are the inlet orifice length and diameter, and equal to 11.8 mm (0.465 in) and 1.59 mm (0.063 in), respectively. For a viscosity (μ) equal to 16.0 centiPoise at 22.6°C (71.6°F), the overall flow resistance of the test *ISFD* is:

$$R_{ISFD\,open} = 1.36 \times 10^9 \quad Pa\text{-}s/m^3$$

Figure 9 shows a comparison of predicted and measured overall flow rate versus oil pressure. Notice that the model underpredicts slightly the test flow rates. The difference is attributed to the lubricant exiting the film lands also in the circumferential direction and not accounted for in the model.

The end plate seals on the integral dampers change the flow direction from mainly axial into almost exclusively circumferential due to the construction of the *ISFD* (see detail in Figure 10). The assumed pressure distribution is as shown in Figure 8(b). In this case the flow through each pad and the flow resistance are given by:

$$Q_{padsealed} = \frac{c^3 L}{3\mu R\gamma} L_s \Delta P_D \qquad R_{padsealed} = \frac{3\mu R\gamma}{c^3 L} \frac{1}{L_s} \tag{20}$$

where L_s is a correction factor accounting for side leakage. ($L_s \rightarrow 1$ when the sealing gap $\rightarrow 0$). This correction factor applies only to the pad flow resistance and not to the overall flow resistance. An interesting result is that

$$R_{padsealed} = \frac{1}{2}\left(\frac{R\gamma}{L}\right)^2 \frac{1}{L_s} R_{padopen} \tag{21}$$

in this case:

$$R_{pad\,sealed} = \frac{.181}{L_s} R_{pad\,open} \tag{22}$$

i.e.,

$$R_{pad\,sealed} > R_{pad\,open} \tag{23}$$

as expected, since the values of L_s are usually very close to unity (see below). The overall pad flow rate for the sealed condition is then given as:

$$Q_{ISFD\ sealed} = \frac{\Delta P}{R_{ISFD\ sealed}} \tag{24}$$

$$R_{ISFD\ sealed} = \frac{R_o + R_{pad\ sealed}}{4} \tag{25}$$

The overall flow resistance, $R_{ISFD\ sealed}$, has been calibrated from experiments at 51.5 kPa (7.5 psig) average inlet pressure for the three different end seals gaps tested (76.2, 101.6 and 127.0 mm; 3, 4 and 5 mils). Figure 11 shows the overall flow rate versus the inlet pressure for the open ended and sealed damper configurations. The open ended damper shows the largest flow rates. However, the most notable finding is related to the invariance of the flow rate with the end seal gap. In fact, the measured flow rates are essentially identical irrespective of the end seal clearance, thus indicating that the flow entering the squeeze film pad leaves in the circumferential direction. The important implication of this finding will become relevant later when the identified force coefficients for the sealed dampers are presented.

The correction factor (L_s) found from the measurements is equal to

End seal gap mm (mils)	L_s
0.127 (5 mils)	1.430
0.101 (4 mils)	1.412
0.076 (3 mils)	1.378

and the value of the overall *ISFDs* resistance for the different end seal conditions is:

End seal gap mm (mils)	$R_{ISFD\ sealed}$ (Pa-s/m^3)
0.127 (5 mils)	1.690×10^9
0.101 (4 mils)	1.657×10^9
0.076 (3 mils)	1.640×10^9
Open ends	1.360×10^9

Figure 12 shows predictions of the oil flow through the *ISFDs* for the case of 0.076 mm (3 mils) end seal gap and using the correction factor (L_s = 1.378). The overlap with the experimental results is a result of the calibration procedure explained above.

Rotor-bearing system parameters for the first mode of vibration

De Santiago, et al. (1997) report the fundamental test rotor-bearing parameters for the first (cylindrical) mode of vibration. Table 1 summarizes the identified system mass (M), support equivalent stiffness coefficients (K_V,K_H), natural frequencies (ω_{nV}, ω_{nH}), and critical damping coefficients (Cc_V, Cc_H), in the vertical and horizontal planes. Bearing support asymmetry results in slightly different natural frequencies in the vertical and horizontal directions.

Although the measured *ISFDs* structural stiffnesses are very close to the design value of 3.506 MN/m (20,000 lbf/in), the bearing support stiffness acting in series with the integral dampers stiffness reduces the effective stiffness thus relocating the system natural frequencies. Impact tests on the supports confirm the values of support stiffness acting in series with the *ISFDs* structural stiffness estimated from the measurements of natural frequency.

Impact Response Measurements on the Rotor Supported on Sealed Integral Dampers

Impact response (rap) tests on the rotor supported on the integral dampers are conducted for sealed conditions with different end seal gaps equal to 0.0762, 0.102 and 0.127 mm (3, 4 and 5 mils). Averaged transfer functions of acceleration/load allow the estimation of the system damping coefficients at zero rotational speed and for different lubricant viscosity. Table 2 shows the values of lubricant viscosity (ISO VG 10 oil) for a range of temperatures from measurements using a spindle viscometer.

Figure 13 shows the rotor acceleration time response in the vertical and horizontal directions due to impact loads exerted at the middle disk. The figures also include typical acceleration/load transfer functions and the coherence functions as averages of 10 impacts. The coherence results demonstrate an excellent correlation of the rotor response to the applied impact for excitation of the fundamental natural frequency.

Table 3 shows the identified system damping coefficients (C_V, C_H) from the impact response tests for the three seal gaps and at different lubricant viscosity values (increasing oil temperatures). Figures 14 show a comparison of the system damping coefficients (vertical and horizontal) estimated from the rap tests versus the lubricant viscosity. The figures include the test results for the dry (structural) damping and the open ended *ISFDs* as determined by De Santiago, et al. (1997). As expected, the system damping coefficients decrease (almost linearly) as the lubricant viscosity decreases (i.e., increasing lubricant temperatures).

The experiments also reveal that the damping coefficients increase with tighter end seals, i.e. the end seal clearance decreases, for the viscosity range of 9 to 17 centipoises. Increments in system damping coefficients for the tightest sealed *ISFDs* are as large as 2.5 times the value of damping coefficient for the open ended dampers. Thus, the measurements demonstrate the effectiveness of the end plate seals without a penalty in the through flow rate (see Figure 11).

Imbalance Response Measurements on the Rotor Supported on Sealed Integral Dampers

Rotor imbalance response tests are conducted for the rotor supported on the dampers sealed with end gaps equal to 0.0762, 0.102 and 0.127 mm (3, 4 and 5 mils). Increasing levels of imbalance excite the first mode of vibration (cylindrical) of the rotor-bearing system. Imbalance masses (m) are attached in the rotor

middle disk at a radius (r) of 114.3 mm (4.5 in). Table 4 summarizes the imbalance conditions for each end seal gap, the test oil temperature, and the effective imbalance distance, $u = (m \times r)/M$, where (M) is the rotor modal mass for the first mode of vibration (see Table 1). Each test condition is performed twice to ensure that the rotor response is repeatable.

A typical coast down imbalance test consists of driving the rotor to a top speed of 8,000 rpm, and then suddenly shutting down the power to the motor. The motor angular speed rapidly decreases due to friction in the motor brushes, but the roller clutch allows the rotor to begin a free coast down. When the motor stops, the rotor continues its deceleration and the only torques dragging the rotor arise from the disks windage friction, friction in the precision rolling element bearings, the friction in the needles of the roller clutch and the tube-type seals in the supports' faces.

Figures 15 show the synchronous rotor responses, vertical and horizontal, versus rotational speed for measurements near the middle disk and for the three end seal gaps, (a) 5 mils, (b) 4 mils, (c) 3 mils. The figures show the increase in the rotor amplitude of response as the imbalance (u) increases. The tightest end seal condition allows the measurements to be conducted with larger levels of imbalance. Figure 16 presents a comparison of the vertical and horizontal rotor imbalance responses for the tree end seal gaps and under similar imbalance conditions. The measurements evidence that the end sealed *ISFDs* reduce the maximum amplitude of vibration while traversing the first critical speed. An increase in the damping coefficients produces a small shift in the critical speed, as evidence from the response comparisons (Figure 16).

Measurements of the rotor speed versus time while the rotor decelerates from the top speed to rest allow estimation of the system time constant (τ). Figure 17depicts the rotor speed time decay curves following a nearly exponential decay, thus suggesting a viscous first order rotational system. The time constant (τ) is given by the expression:

$$\tau = \frac{I_p}{C_R} = \frac{(t_1 - t_2)}{\ln\left(\frac{\dot{\theta}_0}{\dot{\theta}_1}\right)} \tag{26}$$

where (I_p) is the polar mass moment of inertia of the rotor, and (C_R) is the system rotational damping coefficient. The time constant is estimated from the elapsed time when the rotor reaches 36.7% of its initial speed. Table 5 presents the estimated time constants for several test conditions, including the open ended *SFDs*. The rotor speed decay curves confirm the repeatability of the tests since it is apparent that the rotor speed decreases in a similar way for different end seal gaps. Thus, response peaks at the first critical speed can be compared since about the same rotor deceleration occurred for each test condition. The order of the system time constant is approximately 250 sec (4.16 min.), and demonstrates that it takes about 10 minutes (average value) for the rotor to come to decelerate from top speed to rest, further demonstrating the quality of the test rig and of the measurements performed.

Table 6 shows the synchronous maximum amplitudes (peak to peak) of rotor response at each measurement plane (drive end, free end and midspan) and at the first critical speed. The average value is

obtained directly from the drive end, near middle disk and free end measurement planes. The similitude of rotor amplitudes of vibration at the different locations of measurement confirms the cylindrical mode motion performed by the rotor when traversing the first critical speed. Note also that due to the support asymmetry, the critical speed in the horizontal direction is different from that in the vertical direction.

Figure 18 shows the synchronous average amplitudes of rotor response, vertical and horizontal, at the first critical speed versus the imbalance distance (u) for each end seal configuration. Note the linear trends in all cases, thus demonstrating the rotor response is proportional to the imbalance (u) for rotor amplitudes of vibration up to 70% of the damper radial clearance (0.230 mm). The vertical amplitudes are consistently smaller than the horizontal amplitudes, thus denoting larger system damping coefficients in the vertical direction. Note also that tighter end gap seals allow experiments to be conducted with larger imbalances.

System Damping Coefficients from Synchronous Peak Rotor Responses

The synchronous amplitudes of rotor motion at the first critical speed allow estimation of the system damping coefficient. Table 7 shows values of the amplification factor (Q) and the damping ratio (ξ) determined from the peak rotor responses for each end seal and imbalance conditions. Values for motion in the vertical and horizontal directions are noted. The known values of system critical damping (Cc), see Table 1, allow the evaluation of the rotor-bearing system damping coefficient, $(C_i = Cc_i\, \xi_i)_{i=V,H}$.

Figure 19 depicts the average system damping coefficients, vertical and horizontal, versus the end seal gaps. The damping coefficients for the open ended dampers are also included. The values plotted correspond to the arithmetic average of damping coefficients for all imbalance conditions. The vertical bars indicate the variability of the system damping coefficients as noted for the corresponding dimensionless rotor eccentricities (e/c). Note the almost linear decrease in damping coefficients as the end gap seal clearance increases.

Figure 20 shows the estimated system damping coefficients for the different end seals versus the rotor dimensionless eccentricity (from measurements of the maximum amplitude of motion at the first critical speed). In all cases a tighter end seal gap provides an increase in the system damping coefficients for any value of rotor eccentricity, thus confirming the beneficial effect of the end seals on attenuating the rotor response. The values of system damping coefficient at zero eccentricity ($e/c = 0$) correspond to the impact response tests at null rotation. In addition, the increase in damping coefficients due to the end seals appears to be more important at small rotor amplitude motions rather than for large rotor excursions.

The system damping coefficients estimated from the rotor imbalance peak response (see Table 7) are equal to the sum of the viscous damping coefficients provided by the *ISFDs* and the structural (dry) damping coefficients[3]. Thus, the value of the effective damping coefficient provided solely by the integral

[3] This assumption implies the linearity of the mechanical system investigated, i.e. the damping elements structural and hydrodynamic act in parallel at the support locations of the rotor-bearing system. The assumption is, of course, supported by the measurements.

dampers is evaluated by subtracting the structural damping from the identified system damping coefficients. Recall that the *dry* damping coefficients are C_{dryV} = 1,686.39 N-s/m (9.62 lbf-s/in) and C_{dryH} = 950.13 N-s/m (5.42 lbf-s/in) in the vertical and horizontal directions, respectively (from De Santiago, et al 1997). Viscous damping coefficients for the *ISFDs* are just ½ the value of the system damping coefficients obtained since there are two identical dampers in the system. The measurements of rotor displacements at the three axial planes and which show nearly identical amplitudes of rotor vibration validate this assumption (see Table 6). Table 8 summarizes the values of the viscous damping coefficient from the integral dampers, in the vertical and horizontal directions, for the different end seal gaps. Figure 21a depicts the values of viscous damping coefficient, vertical and horizontal, for the sealed integral dampers versus the rotor dimensionless eccentricities. Figure 21b shows normalized viscous damping coefficients as the ratio of the physical damping to the coefficient for the open ended *ISFD* estimated from the rap measurements. The open ended damping coefficients are 720.5 N-s/m (4.11 lb-s/in) and 708.1 N-s/m (4.04 lb-s/in), in the vertical and horizontal directions, respectively. The graphical results aid to appreciate the benefit obtained by sealing the *ISFDs* with respect to the open ends case.

Predictions of Viscous Damping Coefficients from a *FEM* Analysis

A finite element method (FEM) program is used to predict the integral damper viscous damping coefficients for each end seal gap condition. De Santiago, et al. (1997) detail the fundaments of the analysis and computer program. The end seal is modeled as a local seal coefficient C_L , whose value is a function of the seal clearance (c_s) and seal radial length (l_s = 3.00 mm, 0.118 in), and the lubricant viscosity (μ = 0.016 Pa-s at 22.6° C), i.e. (San Andrés and Vance, 1984):

$$C_L = \frac{c_s^{\,3}}{12\mu l_s}\overline{C}_L \qquad (27)$$

where $\overline{C}_L$ is an empirical correction factor. The seal geometry renders values of the local seal coefficient (C_L) equal to

End seal clearance	Local end seal coefficient C_L (m²/s)/Pa
0.127 mm (5 mils gap)	$35.4\text{x}10^{-10}\ \overline{C}_L$
0.102 mm (4 mils gap)	$18.1\text{x}10^{-10}\ \overline{C}_L$
0.076 mm (3 mils gap)	$7.65\text{x}10^{-10}\ \overline{C}_L$

The measurements suggest that air entrains the squeeze film lands when the hydrodynamic pressure tends to be lower than the ambient pressure. Thus, in the analysis, any calculated pressures below ambient are disregarded and do not provide any contribution to the squeeze film forces. Predictions are calculated for a journal describing circular centered orbits at a whirl frequency equal to the rotor/bearing system

natural frequency (~55 Hz). A unit empirical correction factor ($\overline{C}_L$) is used for the sealed integral dampers.

Table 9 summarizes the predictions of the sealed *ISFDs* direct viscous damping coefficients. The analysis shows that the fluid film forces have a stationary component and a periodic variation since the damper is composed of four segments or pads. Figure 22 shows the comparison of the test and predicted viscous damping coefficients for each sealed condition and including the open ended *SFD*. In general, the predicted viscous damping coefficients are in close agreement with the experimental results for the sealed *ISFDs*. However, predictions for the open ended *SFD* compare more favorably with a full film model (De Santiago, et al. 1997) since in these tests the axial flow through the damper prevents the ingestion of air.

Closure

The detailed measurements, impact tests and imbalance response tests, demonstrate that end gap seals render a substantial increase in the *ISFD* viscous damping coefficients and without a severe reduction in the flow through the damper. Conventional (cylindrical) tightly sealed *SFDs* restrict substantially the through flow and determine minimal increments in the damping coefficients since the lubricant viscosity decreases because the operating film temperature raises.

Tighter end seals (i. e. reduced end plate seal clearances) consistently increase the viscous damping coefficients for rotor excursions up to 60% and 80% of the damper radial clearance in the vertical and horizontal planes, respectively. Increments of more than twice the damping coefficient with respect to the open ended *ISFD* are obtained for the end seal of clearance equal to 0.076 mm (3 mils). The measurements further demonstrate that the amplitude of rotor synchronous response at the first critical speeds is proportional to the amount of mass imbalance. No subsynchronous frequencies or (nonlinear) jump phenomenon are ever observed in any of the experiments.

FEM predictions of the viscous damping coefficients for the end sealed *ISFDs* agree favorably with the identified damping coefficients when accounting for the effect of air entrainment in the analysis.

Measurements of Rotor Synchronous Response to Coupled Imbalances

Measurements of the rotor-bearing system response to coupled imbalance masses are useful to determine the effectiveness of the integral dampers in attenuating vibrations related to the conical mode of vibration. The experiments aim to estimate the system angular damping coefficients for the second mode of vibration of the test rotor supported on **open ended** *ISFDs*. Imbalance masses are fixed to the rotor drive and free end disks and 180° apart from each other (see Figure 23). A cross-moment of inertia (J_{xz}) is then generated which excites the rotor conical mode of vibration, in a similar way as a single imbalance mass attached to the rotor middle disk excites the cylindrical mode of vibration. The imbalance cross-moment of inertia is given by,

$$J_{xz} = m_1 d_1 r_1 + m_2 d_2 r_2 \tag{28}$$

where m_1 and m_2 are the imbalance masses set at radii r_1 and r_2 in the drive and free end disks, respectively, and at distances d_1 and d_2 from the rotor center of mass (cg).

An analytical model for a four *DOF* rigid rotor on elastic supports and including disks gyroscopic effects governs the system for the cylindrical and conical rigid body motion modes. The coupled imbalance is expressed as an excitation imbalance angle (β) equal to the ratio of the excitation moment of inertia (J_{xz}) over the modal transverse moment of inertia (I_t = 0.624 Kg-m^2, 5.517 lbm-m^2), estimated from an undamped natural frequency analysis of the rotor-bearing system. *Appendix A* describes the rigid rotor model, which includes gyroscopic effects (San Andrés, 1997). The model enables excitation of the cylindrical and conical modes of vibration by means of an imbalance mass-distance and cross-moment of inertia, respectively (Childs, 1993). The model is programmed as a Mathcad® sheet and requires as inputs the rotor mass, the rotor transverse and polar mass moments of inertia, the distances from the cg to the bearing supports, and the support stiffness and damping coefficients in two orthogonal directions. The analysis does not include cross-coupled force coefficients at the bearings.

Measurements of the rotor response in two orthogonal planes at three axial locations (drive end, free end and near middle disk) are conducted as the rotor coasts down from a top speed of 10,000 rpm. The test conditions for four couple imbalances are summarized in Table 10. Each test is performed twice to verify the rotor response repeatability under similar imbalance conditions. The measured synchronous rotor responses contain the shaft runout (slow roll vector) as well as the response due to a remnant imbalance. The data acquisition system compensates the response for the slow roll vector (runout) and also subtracts the baseline response from the synchronous vibration component of the rotor response.

Figures 24 depict the measured synchronous rotor responses in the vertical and horizontal directions for increasing coupled imbalance angles (β). The rotor responses are shown for (a) drive end, (b) free end, and (c) near the middle disk. Note how the vibration peaks at the second critical speed are not evident for the smaller imbalance condition, but develop clearly as the coupled imbalance increases. In addition, the rotor amplitudes of vibration near the middle disk are much smaller than the amplitudes of vibration at the drive and free ends, as expected for the conical mode response. The measurements show little or no excitation of the cylindrical mode of vibration.

Table 11 shows the identified rotor (conical mode) critical speeds at each bearing support location (6,200-6,600 rpm in the vertical direction and 6,200-6,400 rpm in the horizontal direction). Prior impact response tests identify the conical mode (second) natural frequencies at 89 Hz and 88 Hz in the vertical and horizontal planes, respectively. The critical speeds are larger than the natural frequencies due to gyroscopic effects. The rigid rotor conical mode of vibration is verified by measurements of the relative phase angle between the drive end and free end vibration signatures as will be shown later. The large amplitude (peak) responses around 5,500 rpm, very close to the 2nd critical speeds, are resonances ascribed to the bearing supports and base plate (De Santiago, et al., 1997). Table 12 summarizes the test maximum peak-peak amplitudes of rotor response at the second critical speed for each imbalance condition at the drive end, midspan and free end measurement planes. The table includes the conical mode critical speeds

for each test condition. It is important to note that the rotor orbits are not perfectly circular thus denoting a strong bearing asymmetry.

The phase angles of responses at the drive end and free end measurement planes are compared to verify the rigid rotor motion at the conical mode. Table 13 shows the relative angles of response between the rotor drive and free ends for each test condition, in the vertical and horizontal planes. The relative phase angle is very close to 180°, clearly indicating rotor motion in a conical mode. Figure 25 shows polar plots of the rotor response at the drive and free ends, vertical and horizontal planes, for the largest imbalance condition ($\beta = 0.0116°$). The graphical results evidence the rotor motion in a conical mode.

Simple geometric relationships allow to construct the rigid body motion of the test rotor, using the measured drive and free end amplitudes of response as reference points for straight lines crossing the axis of rotation. A pure rigid body conical motion is verified if the amplitude of response at the middle disk falls in the path of the straight line, as shown in Figure 26. The rotor motion in the vertical plane verifies well the conical rigid body mode, denoting little shaft bending and with null vibration near the rotor center of mass. However, rotor motions in the horizontal plane are suspicious because the straight lines connecting the drive end and free end magnitudes of vibration cross the rotor axis at a location far away from the rotor cg. Furthermore, a motion amplitude of nearly twice the experimental measurement at the drive end is obtained from the projection of the straight line joining the amplitudes near the middle disk and free end plane. The sensitivities of the displacement sensors have been verified independently without any apparent instrumental error yet found. A thorough check on the data acquisition and data processing reveal no faulty signals or procedures. In addition, a bent rotor shape is unlikely to have occurred since the measurements would imply rotor deflections only in the horizontal plane and not in the vertical plane. Perhaps, the drive end bearing support resonance is the culprit for these yet unexplained results.

Estimation of System Angular Damping Coefficients from the Test Responses

Simple trigonometric relationships allow the calculation of the angle (θ) of rotor response for the conical rigid body mode of vibration, the nodal point (null rotor motion), and the effective distance from this point to the bearing locations in the vertical and horizontal planes. Table 14 shows the estimated distances to the nodal points from the rotor cg for each test and the effective distances to the bearing support locations. The angle of response (θ) about the nodal point is calculated assuming a rigid body conical motion as:

$$\theta = arctg\left(\frac{A_f + A_d}{d_{df}}\right) \tag{29}$$

where A_d and A_f are the amplitudes of rotor response at the drive end and free end planes, and d_{df} is the distance between these two planes[4]. Figure 27 depicts the test rotor response angle (θ) to vary linearly with the imbalance excitation angle (β). A linear regression analysis determines the relationship between the maximum angle of rotor response at the second critical speed, in the vertical and horizontal directions, and the imbalance angle (β) rendering trend lines of rotor angular response. However, these trend lines do not project towards the origin of the axes, thus revealing a constant source of unknown angular excitation (most likely, a remnant rotor coupled imbalance).

The amplification factor (Q_θ) for conical rigid body motions corresponds to the slope of the trend line estimated from the maximum rotor angular amplitude (θ) at the second critical speed. The values of the amplification factor (Q_θ) are equal to 6.73 and 6.47 for the vertical and horizontal planes of rotor vibration. The correlation value (R^2) of the linear regressions are $R^2_V = 0.982$ and $R^2_H = 0.998$.

The linear theory of vibrations allows the estimation of the modal angular damping ratio (ξ_θ) from the amplification factor (Q_θ), using the well know relationship:

$$\xi_\theta{}^2 = \frac{-1 \pm \sqrt{1 + 1/Q_\theta{}^2}}{2} \qquad (30)$$

Table 15 shows the conical mode damping ratios, critical damping and system damping coefficients. The values of system angular damping coefficients (C_θ) are valid for the range of rotor eccentricities measured, approximately to 60% of the radial clearance in the open ended *ISFDs*, for the vertical direction (see Table 12). Note that similar damping magnitudes are obtained from motions in the vertical and horizontal planes.

Effective support stiffnesses at the second critical speed

Accurate prediction of the rotor-bearing system critical speeds requires precise values of the equivalent stiffnesses for the bearing supports. Table 1 highlights the fundamental system parameters and notes the effective support stiffnesses (K_V,K_H), which adequately reproduce the cylindrical mode natural frequencies and first critical speeds. These stiffnesses are equal to 2.79 MN/m (15,964 lb/in) and 2.41 MN/m (13,765 lb/in), for the vertical and horizontal directions, respectively. However, these support stiffness values render a prediction of the second (conical mode) critical speeds nearly 2,000 rpm higher than the measurements (see Table 12). The magnitudes of equivalent support stiffnesses, which predict well the measured (cylindrical mode) second critical speeds, are

$$K_{V2} = 1.75 \text{ MN/m (10,000 lb/in)}, \quad K_{H2} = 2.41 \text{ MN/m (13,765 lb/in)} \qquad (31)$$

[4] The free end and midspan amplitudes and distance between these two planes are used in the estimation of the response angle (θ) in the horizontal plane. Note that the drive end magnitudes of response appear suspicious.

The reduction in the effective support stiffness magnitude for the vertical direction is due to the resonance of the bearing supports and base plate (~5,500 rpm). That is, the inertia and elastic effects of the bearing housings and base plate contribute to reduce the effective support stiffness.

Estimation of Supports Damping Coefficients from Peak Rotor Responses

The rigid rotor model (Appendix A) for calculation of the synchronous rotor response is used to evaluate the supports' equivalent damping coefficients by matching predicted peak responses at the second critical speed to the measured magnitudes of rotor motion at the free end (vertical direction). Recall that the measurements in the vertical plane reproduce more closely the conical mode with a nodal point very close to the rotor center of mass. In the predictions, an effective coupled imbalance excitation angle (β_{eff}) is used since the measurements indicate an unknown source of remnant coupled imbalance (β_o), see Figure 28. The effective angle of excitation (β_{eff}) is defined as:

$$\beta_{eff} = \beta - \beta_o \tag{32}$$

where β_o is equal to 2.33 x 10^{-3} °, i.e., an average value from the vertical and horizontal peak rotor responses determined from the tests results given in Figure 27. The effective cross-moment $(J_{xz})_{eff}$ of inertia is equal to ($\beta_{eff} I_t$). Note that the expression given as equation (28) assumes a remnant couple-imbalance location identical to that of the experiments.

Table 16 summarizes the predicted and measured peak amplitudes of rotor response at the second critical speed for each couple-imbalance condition. Figures 29 show a comparison of the measured and predicted rigid rotor responses for the largest imbalance condition (β = 0.0116°). The analytical predictions render a fairly good representation of the synchronous rotor amplitudes of vibration at the second critical speed. However, the agreement is poor for the rotor horizontal motions at the drive end. Recall that the simple rigid rotor model is not able to replicate the bearing support resonances. Table 16 also includes the physical magnitudes for the supports' damping coefficients as specified in the analysis. Figure 30 depicts the support damping coefficients estimated from the matching-peaks method versus the imbalance angle of excitation (β). Note that the support damping coefficients in the vertical direction are larger than in the horizontal direction, and decrease as the excitation angle increases (β). These results are in opposition to those obtained for the first (cylindrical) mode of vibration of the rotor-bearing system. Furthermore, the magnitudes of these effective support-damping coefficients (second mode of vibration) are lower than the values obtained from the imbalance response tests for the fundamental mode of vibration (cylindrical) (De Santiago, et al., 1997). The differences may be attributed to the complex behavior of the bearing supports, which show a resonance just below the second critical speed.

System angular damping coefficients $(C_\theta)_{V,H}$ are calculated from the supports translational damping coefficients, using the relationship

$$C_\theta = C_D d_D^2 + C_F d_F^2 \qquad (33)$$

where $(C,d)_{D,F}$ are the support damping coefficient and distance from bearing support to the rotor cg for the drive end and free ends, respectively. The calculated values of angular damping coefficients are given in Table 17 and compared to the test derived coefficients. Note that the theoretical average values of the system angular damping coefficients $(C_\theta)_{V,H}$ are slightly larger than the identified damping values from the measured rotor angular responses.

Closure

Measurements of the test rotor synchronous response have been conducted for a range of couple-imbalances exciting the second (conical) mode of the rotor bearing system. In these tests, the integral dampers have no end seals, i.e. open ended configuration. The experiments reveal a bearing support/base table resonance just below the second critical speed. Effective bearing support stiffness and (probably) support and *ISFD* damping coefficients affect this condition and also relocate the second critical speeds.

The measurements in the vertical plane demonstrate the rotor motion is a conical rigid body mode. However, the measurements in the horizontal plane show a peculiar behavior at the drive end plane, with amplitudes of response much lower than in the vertical plane. It is possible that the bearing support in this plane has a large motion not accounted for in the analysis. Further analysis of the bearing support accelerations may elucidate the observed phenomenon. The peak rotor amplitude responses at the second critical speeds are proportional to the couple-imbalance angle. The experimental results thus confirm a linear behavior of the test rotor for this mode of vibration.

A rigid rotor and elastic bearing supports model predicts the rotor response for increasing levels of imbalance. Effective damping coefficients for the bearing supports are estimated by matching predicted peak amplitudes of motion at the second critical speed with the test measurements at the free end (vertical plane). Angular damping coefficients for the vertical and horizontal plane conical motions are nearly identical. Predicted average system angular damping coefficients correlate well with the test values. The integral squeeze film dampers show their effectiveness in attenuating the vibratory response of the test rotor for excitations of its conical rigid body mode.

TABLES

Table 1. Identified rotor-bearing fundamental system parameters for first (cylindrical) mode of vibration.

Source: De Santiago, et al. (1997)

Rotor mass for the first mode of vibration	M	45.22 kg (99.6 lb)
Natural frequency		
Vertical direction	ω_{nV}	56 Hz
Horizontal direction	ω_{nH}	52 Hz
Effective support stiffness from natural frequency		
Vertical direction	K_V	5.596 MN/m (31,928 lb/in)
Horizontal direction	K_H	4.826 MN/m (27,530 lb/in)
System critical damping		
Vertical direction	Cc_V	31,905 N-s/m (182.0 lb-s/in)
Horizontal direction	Cc_H	29,626 N-s/m (169.0 lb-s/in)

Experimental values of *ISFDs* stiffness and supports dynamic stiffness for the first mode of vibration:

ISFDs structural stiffness:	(From static measurements)
Vertical	
Drive end:	3.655 MN/m (20,850 lb/in)
Free end:	3.497 MN/m (19,950 lb/in)
Horizontal	
Drive end:	3.796 MN/m (21,660 lb/in)
Free end:	3.527 MN/m (20,120 lb/in)
Supports dynamic stiffness for the first mode of vibration:	**(From impact tests)**
Vertical	
Drive end:	30.65 MN/m (174,868 lb/in)
Free end:	28.18 ± 5.549 MN/m (160,758 ± 31,660 lb/in)
Horizontal	
Drive end:	13.94 ± 0.716 MN/m (79,556 ± 4,087 lb/in)
Free end:	10.08 ± 0.766 MN/m (57,556 ± 4,370 lb/in)

Table 2. Measured viscosity of lubricant (ISO VG 10 oil, specific gravity: 0.85).

Temperature °C (°F)	Viscosity CentiPoise
22.6 (72.7)	16.06
25.3 (77.5)	13.95
29.4 (84.9)	12.26
34.1 (93.4)	10.14
40.0 (104.0)	8.45
44.0 (111.2)	7.65
50.4 (122.7)	6.54

Table 3. *System* damping coefficients estimated from impact tests for different lubricant viscosity (increasing temperature). Open ended, 0.127, 0.102 and 0.0762 mm (5, 4 and 3 mils) end gap seals *ISFDs*.

VERTICAL Dry (structural) system damping coefficient: 1686.39 N-s/m (9.62 lb-s/in)

Open ended				0.127 mm (5 mils) end seal			
Temperature	Viscosity	System damping coefficient		Temperature	Viscosity	System damping coefficient	
°C	cP	N-s/m	lb-s/in	°C	cP	N-s/m	lb-s/in
22.78	15.967	3,127.35	17.84	21.06	16.879	3,795.25	21.65
23.61	15.544	2,820.58	16.09	24.39	15.157	3,653.25	20.84
24.72	14.997	2,808.31	16.02	28.11	13.440	3,490.22	19.91
29.44	12.875	2,708.39	15.45	32.39	11.704	3,220.26	18.37
37.78	9.833	2,554.12	14.57	36.39	10.285	3,144.88	17.94

0.102 mm (4 mils) end seal				0.0762 mm (3 mils) end seal			
Temperature	Viscosity	System damping coefficient		Temperature	Viscosity	System damping coefficient	
°C	cP	N-s/m	lb-s/in	°C	cP	N-s/m	lb-s/in
20.94	16.945	4,417.56	25.20	20.00	17.468	6,021.56	34.35
28.06	13.462	3,961.78	22.60	23.28	15.711	5,947.93	33.93
31.94	11.876	3,611.18	20.60	26.83	14.008	5,397.49	30.79
36.83	10.140	3,593.65	20.50	32.50	11.663	4,655.97	26.56
				37.72	9.852	3,946.00	22.51

HORIZONTAL Dry (structural) system damping coefficient: 950.13 N-s/m (5.42 lb-s/in)

Open ended				0.127 mm (5 mils) end seal			
Temperature	Viscosity	System damping coefficient		Temperature	Viscosity	System damping coefficient	
°C	cP	N-s/m	lb-s/in	°C	cP	N-s/m	lb-s/in
23.61	15.544	2,387.59	13.62	21.39	16.700	2,988.87	17.05
24.72	14.997	2,114.12	12.06	26.00	14.389	2,946.79	16.81
29.44	12.875	1,902.36	10.85	29.11	13.013	2,787.27	15.90
37.78	9.833	1,730.74	9.87	32.22	11.769	2,543.60	14.51
				38.22	9.694	2,401.61	13.70

0.102 mm (4 mils) end seal				0.0762 mm (3 mils) end seal			
Temperature	Viscosity	System damping coefficient		Temperature	Viscosity	System damping coefficient	
°C	cP	N-s/m	lb-s/in	°C	cP	N-s/m	lb-s/in
21.33	16.733	3,348.23	19.10	19.72	17.626	4,179.15	23.84
27.83	13.563	3,015.16	17.20	22.78	15.967	4,007.36	22.86
31.33	12.112	2,822.33	16.10	26.11	14.338	3,896.92	22.23
38.06	9.745	2,682.09	15.30	32.00	11.853	3,546.32	20.23
				37.50	9.923	3,022.17	17.24

Table 4. Imbalance conditions for measurements of rotor synchronous response with sealed dampers.

0.127 mm (5 mils) end gap seals

Test number	Imbalance mass (m) gr	Imbalance distance (u) μm (mils)	Oil temperature °C (°F)	Viscosity cP
160	10.1	25.5 (1.00)	24.4 (76.0)	15.16
161	13.2	33.3 (1.31)	25.3 (77.5)	14.70
163	16.8	42.4 (1.67)	22.5 (72.5)	16.11
166	19.8	50.0 (1.97)	25.0 (77.0)	14.89

0.102 mm (4 mils) end gap seals

Test number	Imbalance mass (m) gr	Imbalance distance (u) μm (mils)	Oil temperature °C (°F)	Viscosity cP
181	11.8	30.0 (1.18)	24.7 (76.4)	15.01
183	14.93	37.7 (1.48)	23.3 (74.0)	15.70
184	19.03	48.1 (1.89)	25.1 (77.2)	14.80
187	23.25	58.8 (2.31)	24.9 (76.8)	14.90
188	25.25	63.8 (2.51)	26.4 (79.5)	14.21

0.076 mm (3 mils) end gap seals

Test number	Imbalance mass (m) gr	Imbalance distance (u) μm (mils)	Oil temperature °C (°F)	Viscosity cP
170	13.1	33.1 (1.30)	23.9 (75.0)	15.41
172	17.2	43.5 (1.71)	23.6 (74.5)	15.56
174	20.2	51.0 (2.01)	22.1 (71.8)	16.33
176	24.7	62.4 (2.46)	22.7 (72.8)	16.02

Table 5. Rotor-bearing system time constants (τ) for different test conditions.

Test number	End seal gap mm (mils)	Imbalance mass (gr.)	Initial shaft speed (rpm)	Second shaft speed (rpm)	Elapsed time (sec)	Time constant τ (sec)
121	Open ended	5	10,000	4,000	209	*228.1*
127	Open ended	17	10,000	4,000	207	*225.9*
160	0.127 (5)	10.1	7,000	3,000	247	*291.5*
163	0.127 (5)	16.8	7,000	3,000	245	*289.2*
184	0.102 (4)	19.0	7,000	3,000	218	*257.3*
188	0.102 (4)	25.3	7,000	3,000	203	*239.6*
172	0.076 (3)	17.2	8,000	3,000	238	*242.7*
176	0.076 (3)	24.7	8,000	3,000	259	*264.1*

Rotor polar mass moment of inertia, $I_p = 0.286$ N-s-m^2 (979.4 lbm-in^2)

Table 6. Amplitudes of rotor response at the first critical speed for increasing imbalances. Sealed *ISFDs*. Measurements at rotor drive end, near middle disk, and free end.
* (compensated synchronous amplitudes for baseline and slow roll vector at 500 rpm).

0.127 mm (5 mils) end gap seal:

Imbalance distance (microns)	Vertical (mm p-p)				Horizontal (mm p-p)			
	drive	middle	free	Average	drive	middle	free	Average.
25.53	0.167	0.161	0.155	0.161	0.202	0.210	0.181	0.198
33.36	0.213	0.202	0.199	0.205	0.267	0.276	0.237	0.260
42.46	0.249	0.236	0.234	0.240	0.316	0.323	0.282	0.307
50.05	0.286	0.270	0.274	0.277	0.373	0.382	0.329	0.361

Critical speed vertical = 3200 - 3250 rpm
Critical speed horizontal = 2900 - 2950 rpm

0.102 mm (4 mils) end gap seal:

Imbalance distance (microns)	Vertical (mm p-p)				Horizontal (mm p-p)			
	drive	middle	free	Average	drive	middle	free	Average.
30.03	0.172	0.167	0.174	0.171	0.219	0.229	0.204	0.217
37.74	0.214	0.206	0.213	0.211	0.265	0.281	0.249	0.265
48.10	0.256	0.249	0.263	0.256	0.338	0.352	0.314	0.335
58.77	0.301	0.291	0.309	0.300	0.380	0.400	0.356	0.379
63.82	0.301	0.293	0.312	0.302	0.404	0.417	0.378	0.400

Critical speed vertical = 3300 - 3400 rpm
Critical speed horizontal = 3000 - 3050 rpm

0.076 mm (3 mils) end gap seal:

Imbalance distance (microns)	Vertical (mm p-p)				Horizontal (mm p-p)			
	drive	middle	free	Average	drive	middle	free	Average.
33.11	0.167	0.164	0.171	0.167	0.199	0.215	0.192	0.202
43.48	0.211	0.208	0.217	0.212	0.280	0.297	0.267	0.281
51.06	0.242	0.233	0.241	0.239	0.315	0.334	0.303	0.317
62.43	0.265	0.257	0.281	0.268	0.388	0.407	0.370	0.388

Critical speed vertical = 3300 - 3450 rpm
Critical speed horizontal = 3050 - 3100 rpm

Table 7. Estimated *system* damping coefficients from rotor imbalance responses. Sealed *ISFDs.*

0.127 mm (5 mils) end gap seals

Vertical direction

Imbalance mass	Imbalance distance	Average amplitude X_{Vmax}	Dimensionless eccentricity e/c	Amplification factor Q_V	Damping ratio ξ_V	System damping coefficient	
(gr)	(microns)	(mm 0-p)	(-)			N-s/m	lb-s/in
10.1	25.53	0.081	0.35	3.15	0.157	4,998 ± 2.76%	28.51
13.2	33.36	0.102	0.45	3.07	0.161	5,135 ± 2.22%	29.29
16.8	42.46	0.120	0.52	2.82	0.175	5,569 ± 1.93%	31.77
19.8	50.05	0.138	0.61	2.76	0.178	5,682 ± 1.77%	32.41
					Average =	5,346	30

Horizontal direction

Imbalance mass	Imbalance distance	Average amplitude X_{Hmax}	Dimensionless eccentricity e/c	Amplification factor Q_H	Damping ratio ξ_H	System damping coefficient	
(gr)	(microns)	(mm 0-p)	(-)			N-s/m	lb-s/in
10.1	25.53	0.099	0.43	3.87	0.128	3,795 ± 2.34%	21.65
13.2	33.36	0.130	0.57	3.90	0.127	3,771 ± 1.87%	21.51
16.8	42.46	0.154	0.67	3.61	0.137	4,060 ± 1.82%	23.16
19.8	50.05	0.181	0.79	3.61	0.137	4,065 ± 1.81%	23.19
					Average =	3,923	22

0.102 mm (4 mils) end gap seals

Vertical direction

Imbalance mass	Imbalance distance	Average amplitude X_{Vmax}	Dimensionless eccentricity e/c	Amplification factor Q_V	Damping ratio ξ_V	System damping coefficient	
(gr)	(microns)	(mm 0-p)	(-)			N-s/m	lb-s/in
11.88	30.03	0.086	0.37	2.85	0.173	5,521 ± 2.60%	31.49
14.93	37.74	0.106	0.46	2.80	0.176	5,620 ± 2.15%	32.06
19.03	48.10	0.128	0.56	2.66	0.185	5,895 ± 1.82%	33.63
23.25	58.77	0.150	0.66	2.56	0.192	6,131 ± 1.76%	34.97
25.25	63.82	0.151	0.66	2.37	0.207	6,603 ± 1.75%	37.66
					Average =	5,954	34

Horizontal direction

Imbalance mass	Imbalance distance	Average amplitude X_{Hmax}	Dimensionless eccentricity e/c	Amplification factor Q_H	Damping ratio ξ_H	System damping coefficient	
(gr)	(microns)	(mm 0-p)	(-)			N-s/m	lb-s/in
11.88	30.03	0.109	0.48	3.62	0.137	4,055 ± 2.14%	23.13
14.93	37.74	0.133	0.58	3.51	0.141	4,178 ± 1.82%	23.83
19.03	48.10	0.167	0.73	3.48	0.142	4,216 ± 1.80%	24.05
23.25	58.77	0.189	0.83	3.22	0.153	4,545 ± 1.79%	25.92
25.25	63.82	0.200	0.87	3.13	0.158	4,673 ± 1.79%	26.66
					Average =	4,333	25

Table 7. continued

0.076 mm (3 mils) end gap seals

Vertical direction

Imbalance mass	Imbalance distance	Average amplitude X_{Vmax}	Dimensionless eccentricity e/c	Amplification factor Q_V	Damping ratio ξ_V	System damping coefficient	
(gr)	(microns)	(mm 0-p)	(-)			N-s/m	lb-s/in
13.1	33.11	0.084	0.37	2.53	0.194	6,197 ± 2.65%	35.35
17.2	43.48	0.106	0.46	2.44	0.201	6,414 ± 2.13%	36.59
20.2	51.06	0.119	0.52	2.34	0.209	6,681 ± 1.92%	38.11
24.7	62.43	0.134	0.59	2.14	0.227	7,256 ± 1.75%	41.39
					Average =	6,637	38

Horizontal direction

Imbalance mass	Imbalance distance	Average amplitude X_{Hmax}	Dimensionless eccentricity e/c	Amplification factor Q_H	Damping ratio ξ_H	System damping coefficient	
(gr)	(microns)	(mm 0-p)	(-)			N-s/m	lb-s/in
13.1	33.11	0.101	0.44	3.05	0.162	4,794 ± 2.26%	27.35
17.2	43.48	0.141	0.62	3.24	0.153	4,526 ± 1.79%	25.82
20.2	51.06	0.159	0.69	3.11	0.159	4,708 ± 1.79%	26.85
24.7	62.43	0.194	0.85	3.11	0.159	4,704 ± 1.78%	26.83
					Average =	4,683	27

Percent variations denote uncertainty on estimated coefficients.

Table 8. Experimental viscous damping coefficients for sealed integral dampers.

VERTICAL

Open ended			0.127 mm (5 mils) end gap seal		
Rotor dimensionless eccentricity	*ISFD* damping coefficient		Rotor dimensionless eccentricity	*ISFD* damping coefficient	
e/c	N-s/m	lb-s/in	*e/c*	N-s/m	lb-s/in
0.00	720.48	4.11	0.00	983.43	5.61
0.23	1,055.31	6.02	0.35	1,655.83	9.45
0.42	1,277.94	7.29	0.45	1,724.32	9.84
0.50	1,435.71	8.19	0.52	1,941.16	11.07
0.61	1,596.98	9.11	0.61	1,997.78	11.40

0.102 mm (4 mils) end gap seal			0.076 mm (3 mils) end gap seal		
Rotor dimensionless eccentricity	*ISFD* damping coefficient		Rotor dimensionless eccentricity	*ISFD* damping coefficient	
e/c	N-s/m	lb-s/in	*e/c*	N-s/m	lb-s/in
0.00	1,365.59	7.79	0.00	2,131.65	12.16
0.37	1,917.09	10.94	0.37	2,255.55	12.87
0.46	1,966.65	11.22	0.46	2,364.01	13.49
0.56	2,104.27	12.00	0.52	2,497.07	14.24
0.66	2,222.19	12.68	0.59	2,784.99	15.89
0.66	2,458.12	14.02			

HORIZONTAL

Open ended			0.127 mm (5 mils) end gap seal		
Rotor dimensionless eccentricity	*ISFD* damping coefficient		Rotor dimensionless eccentricity	*ISFD* damping coefficient	
e/c	N-s/m	lb-s/in	*e/c*	N-s/m	lb-s/in
0.00	708.21	4.04	0.00	1,020.25	5.82
0.28	972.92	5.55	0.43	1,422.55	8.11
0.56	979.93	5.59	0.57	1,410.60	8.05
0.66	1,123.67	6.41	0.67	1,554.89	8.87
0.79	1,286.70	7.34	0.79	1,557.58	8.89

0.102 mm (4 mils) end gap seal			0.076 mm (3 mils) end gap seal		
Rotor dimensionless eccentricity	*ISFD* damping coefficient		Rotor dimensionless eccentricity	*ISFD* damping coefficient	
e/c	N-s/m	lb-s/in	*e/c*	N-s/m	lb-s/in
0.00	1,199.05	6.84	0.00	1,528.62	8.72
0.48	1,552.68	8.86	0.44	1,921.90	10.96
0.58	1,613.72	9.21	0.62	1,787.77	10.20
0.73	1,632.73	9.31	0.69	1,878.77	10.72
0.83	1,797.26	10.25	0.85	1,876.95	10.71
0.87	1,861.52	10.62			

Table 9. Predicted viscous damping coefficients for sealed integral dampers. *FEM-SFD* model with lubricant cavitation at ambient condition. Circular centered orbits.

0.127 mm (5 mils) end seal gap

Local seal coefficient estimated from seal geometry: C_L = **35.4 x10^{-10} (m^2/s)/Pa**

Orbit radius (microns)	Dimensionless journal eccentricity *e/c*	Predicted direct damping coefficient mean (N-s/m)	Predicted direct damping coefficient Fluctuation (N-s/m)	Maximum pressure in the film around the journal (bar)
10	0.04	1,430	34.4	0.0713
80	0.35	1,530	293	0.716
100	0.43	1,610	384	1.03
120	0.52	1,730	499	1.51
140	0.61	1,910	673	2.38
160	0.70	2,230	1,030	4.22

0.102 mm (4 mils) end seal gap

Local seal coefficient estimated from seal geometry: C_L = **18.1 x10^{-10} (m^2/s)/Pa**

Orbit radius (microns)	Dimensionless journal eccentricity *e/c*	Predicted direct damping Coefficient mean (N-s/m)	Predicted direct damping Coefficient Fluctuation (N-s/m)	Maximum pressure in the film around the journal (bar)
10	0.04	1,760	50	0.0858
80	0.35	1,910	431	0.887
100	0.43	2,010	564	1.28
120	0.52	2,150	715	1.84
140	0.61	2,350	908	2.76
160	0.70	2,700	1,220	4.58

0.076 mm (3 mils) end seal gap

Local seal coefficient estimated from seal geometry: C_L = **7.65 x10^{-10} (m^2/s)/Pa**

Orbit radius (microns)	Dimensionless journal eccentricity *e/c*	Predicted direct damping Coefficient mean (N-s/m)	Predicted direct damping Coefficient Fluctuation (N-s/m)	Maximum pressure in the film around the journal (bar)
10	0.04	2,120	72.1	0.102
80	0.35	2,360	656	1.12
100	0.43	2,510	878	1.63
120	0.52	2,720	1,140	2.4
140	0.61	3,000	1,460	3.55
160	0.70	3,430	1,870	5.64

Table 10. Summary of tests conditions for couple-imbalance experiments.

Test Condition	Tests	Imbalance masses conditions*		Oil Temperature	Excitation Moment of inertia J_{xz}	Imbalance angle β
		Drive end radius r_1 114.3 mm (4.5 in)	Free end radius r_2 95.25 mm (3.75 in)	°C (°F)	N-m-s^2 x 10^{-6} (lb-in-s^2 x10^{-6})	(deg x 10^{-3})
A	146-147	2.3 gr.	2.8 gr.	22 (72.2)	44.68 (395)	4.10
B	148-149	4.6 gr.	5.4 gr.	22 (71.2)	87.09 (770)	8.00
C	154-155	5.5 gr.	6.7 gr.	23 (73.2)	106.8 (944)	9.80
D	152-153	6.5 gr.	8.0 gr.	25 (76.5)	126.7 (1120)	11.60

I_t= 0.624 Kg-m,^{2} =5.517 lbm-in^2, $J_{xz}=m_1r_1d_1+m_2r_2d_2$, $\beta=J_{xz}/I_t$

* Imbalance masses fixed 180° apart

** Distance from rotor CG to drive end disk d_1=66.73 mm (2.613 in), distance from rotor CG to free end disk d_2=101.9 mm (4.012 in)

Table 11. Identified second critical speeds and bearing supports resonance speed.

Drive end			
Vertical:	**6,600 rpm – 2^{nd} *Critical Speed***	Horizontal:	**6,200 rpm – 2^{nd} *Critical Speed***
	6,200 rpm - Support Resonance		5,800 rpm - Support Resonance
	5,500 rpm – Support Resonance		
Free end			
Vertical:	**6,600-6,900 rpm 2^{nd} *Crit. Speed***	Horizontal:	**6,400 rpm – 2^{nd} *Critical Speed***
	5,800 rpm - Support Resonance		5,600 rpm - Support Resonance

Natural frequencies for the second mode of vibration from impact tests (zero rotor speed):
Vertical: $\omega_{n0,I}$= 559.2 r/s (89 Hz), Horizontal: $\omega_{n0,II}$ = 552.9 r/s (88 Hz)

Table 12. Experimental maximum rotor (p-p) amplitudes at second critical speed. Measurements at drive end, midspan and free end planes.

Test Condition	Imbalance angle β (deg x 10^{-3})	Max. amplitudes of vibration at second critical speed (mm p-p)				
		drive end		midspan	free end	
		vertical	horizontal	horizontal	Vertical	Horizontal
A	4.10	0.037	0.0320	0.0100	0.047	0.074
B	8.00	0.135	0.0718	0.0612	0.1515	0.196
C	9.80	0.183	0.08343	0.0817	0.2088	0.2452
D	11.60	0.256	0.1207	0.0910	0.282	0.3192

Test Condition	Imbalance angle β (deg x 10^{-3})	Second critical speed (rpm)				
		drive end		midspan	free end	
		vertical	horizontal	horizontal	Vertical	horizontal
A	4.10	6,850	6,250-6,300	6250	6,900	6,300
B	8.00	6,700-6,750	6,250-6,300	6250	6,600	6,350-6,400
C	9.80	6,600-6,700	6,150-6,300	6250	6,500	6,400
D	11.60	6,600-6,650	6,200	6200	6,900	6,400

Distance between measurement planes:
vertical plane (between drive end and free end) = 266.7 mm (10.5 in)
horizontal plane (between free end and near middle disk) = 190.5 mm (7.5 in)

Table 13. Relative phase angles of rotor response between drive end and free end at the second critical speed. Vertical and horizontal directions.

Test Condition	Imbalance angle β (deg x 10^{-3})	Relative angle of response between rotor drive and free ends (deg)	
		vertical	horizontal
A	4.10	184°	181.5°
B	8.00	169°	174.5°
C	9.80	162.5°	189°
D	11.60	196°	190°

Table 14. Nodal points measured from the rotor cg and nodal distances to the bearing support locations for different levels of imbalance. Conical mode of vibration.

Imbalance angle β (deg x 10^{-3})	Node distance from rotor cg (mm)		Bearings location to nodal point. **Vertical** direction. (mm)		Bearings location to nodal point. **Horizontal** direction. (mm)	
	Vertical	Horizontal	drive end	free end	drive end	free end
4.10	-2.108	-39.07	187.3	219.07	150.4	256.0
8.00	6.087	-48.08	195.5	210.87	141.4	265.0
9.80	4.985	-51.87	175.1	231.3	137.6	268.8
11.60	7.323	-46.41	196.8	209.6	146.0	263.3

Distances from cg to bearing supports, drive end: d_D = 189 mm (7.44 in), free end d_F = 217 mm (8.54 in)
Note: Minus sign indicates direction from rotor C.G. towards drive end

Table 15. Identified *system* angular damping coefficients for conical mode of vibration.

Parameter		Vertical Plane	Horizontal Plane
Angular damping ratio	ξ_θ	0.074	0.107
Critical damping coeffic.	$Cc_\theta = 2\, I_t\, \omega_{n\theta}$	841.7 N-s-m/rad	832.3 N-s-m/rad.
undamped (second mode) natural frequencies (*)	$\omega_{n\theta}$	674 rad/s (107 Hz) at 6,6 krpm	666 rad/s (106 Hz) at 6.3 krpm
System angular damping coefficient	$C_\theta = \xi_\theta Cc_\theta$	62.7 N-s-m/rad	64.1 N-s-m/rad

I_t= 0.624 Kg-m^2 (5.517 lbm-in^2), modal transverse mass moment of inertia,
* (includes rotor spin and rotor gyroscopic effects)

Table 16. Estimated damping coefficients for bearing supports. Matching of predicted peak response from rigid rotor model to measurement at free end (vertical plane).

Imbalance angle β (deg x 10^{-3})	Amplitude of vibration (mm p-p)							
	drive end				free end			
	vertical		Horizontal		vertical**		horizontal	
	exp.	*model*	exp.	*model*	exp.	*model*	exp.	*model*
4.10	0.037	*0.0351*	0.0320	*0.0430*	0.047	*0.0449*	0.074	*0.0564*
8.00	0.135	*0.117*	0.072*	*0.142*	0.1515	*0.150*	0.196	*0.185*
9.80	0.183	*0.160*	0.083*	*0.192*	0.209	*0.205*	0.245	*0.251*
11.60	0.256	*0.220*	0.121*	*0.262*	0.282	*0.282*	0.319	*0.344*

Imbalance angle β (deg x 10^{-3})	System damping coefficients N-s/m (lb-s/in) (Matching curves procedure)			
	drive end		free end	
	vertical damping	horizontal damping	vertical damping	horizontal damping
4.10	1,290 (7.36)	684 (3.90)	1290 (7.36)	684 (3.90)
8.00	992 (5.66)	869 (4.96)	1055 (6.02)	745 (4.25)
9.80	853 (4.87)	867 (4.95)	853 (4.87)	867 (4.95)
11.60	626 (3.57)	877 (5.00)	626 (3.57)	877 (5.00)

* Suspicious of faulty reading.

** Experimental measurements utilized as benchmark for estimation of damping coefficients.

Table 17. Predicted *System* Angular damping coefficients for couple-imbalance responses.

Imbalance angle β (deg x 10^{-3})	$C_{\alpha\alpha}$ (N-m-s/rad)	$C_{\beta\beta}$ (N-m-s/rad)
4.10	102.7	60.2
8.00	84.7	69.7
9.80	71.6	79.1
11.60	51.4	79.5
Average =	**77.6**	**72.1**
From tests	62.7	64.1

FIGURES

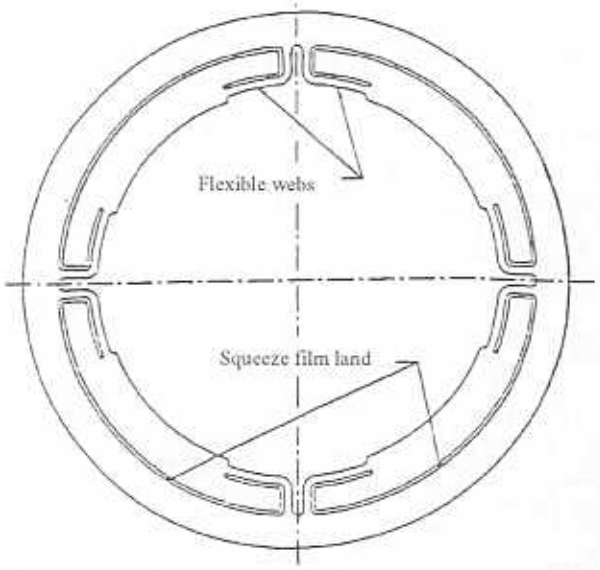

Figure 1. Schematic view of an integral centering spring *SFD*.

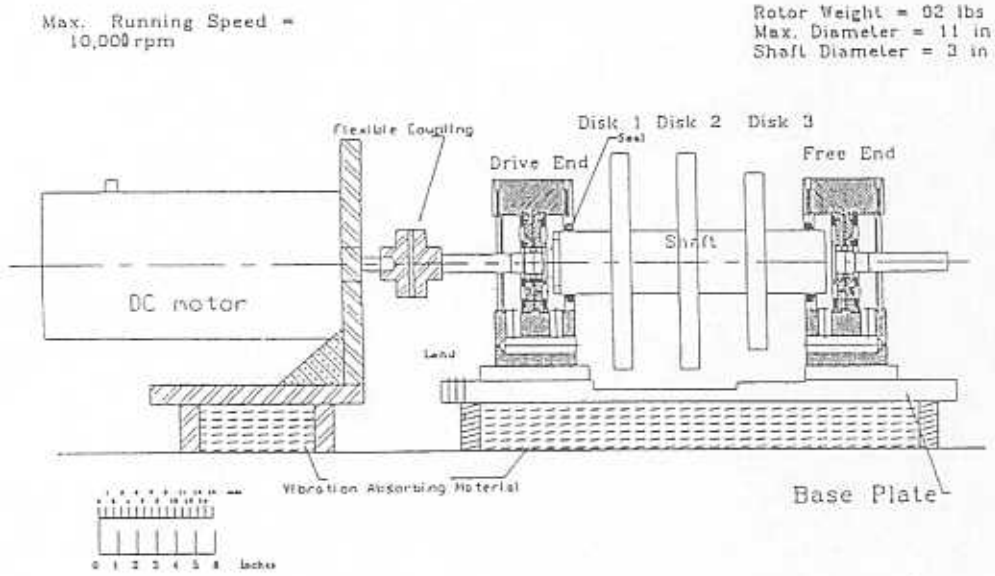

Figure 2. View of test rig. Rotor bearing supported on *ISFDs*.

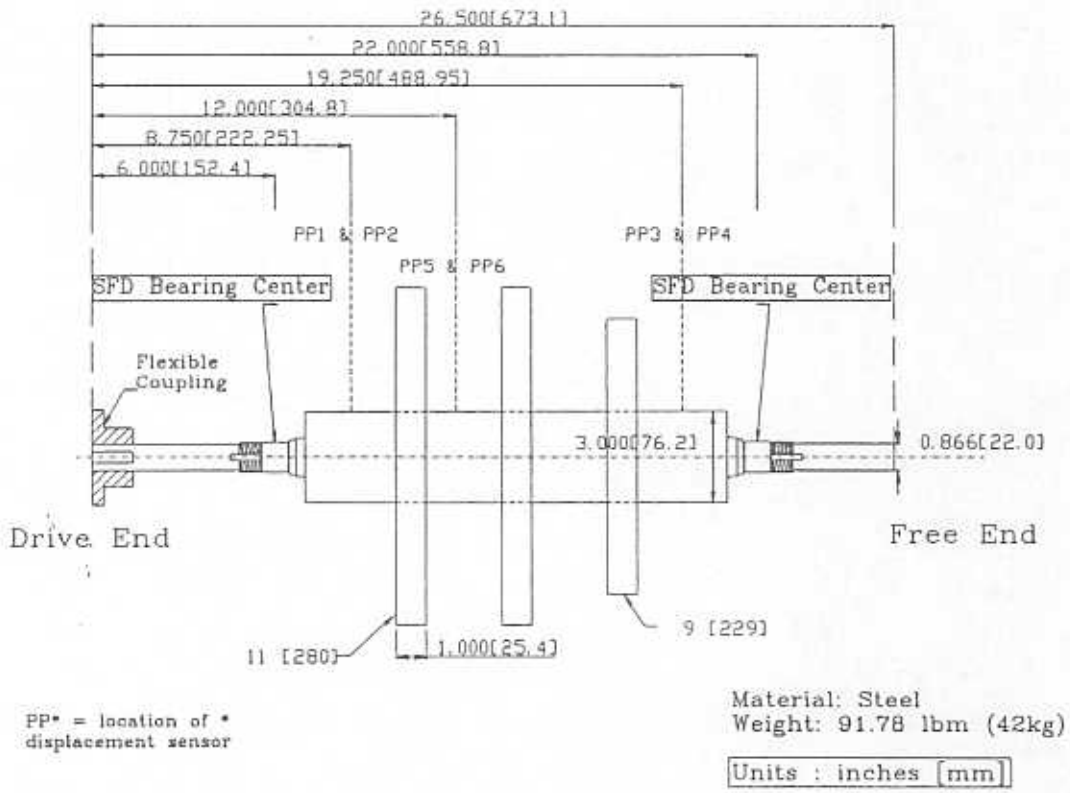

Figure 3. Test rotor dimensions and distances to bearing supports and displacement sensors.

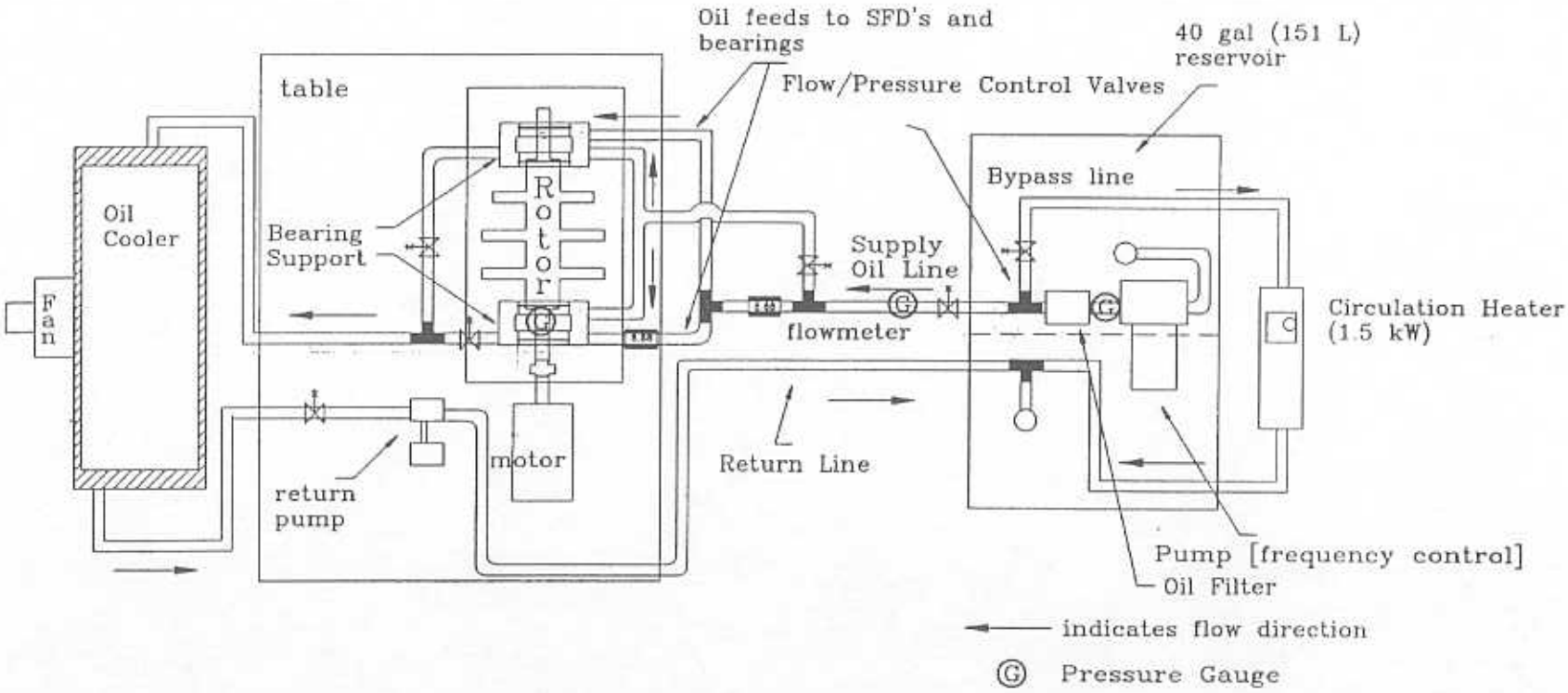

Figure 4. Lubrication system of squeeze film damper test apparatus.

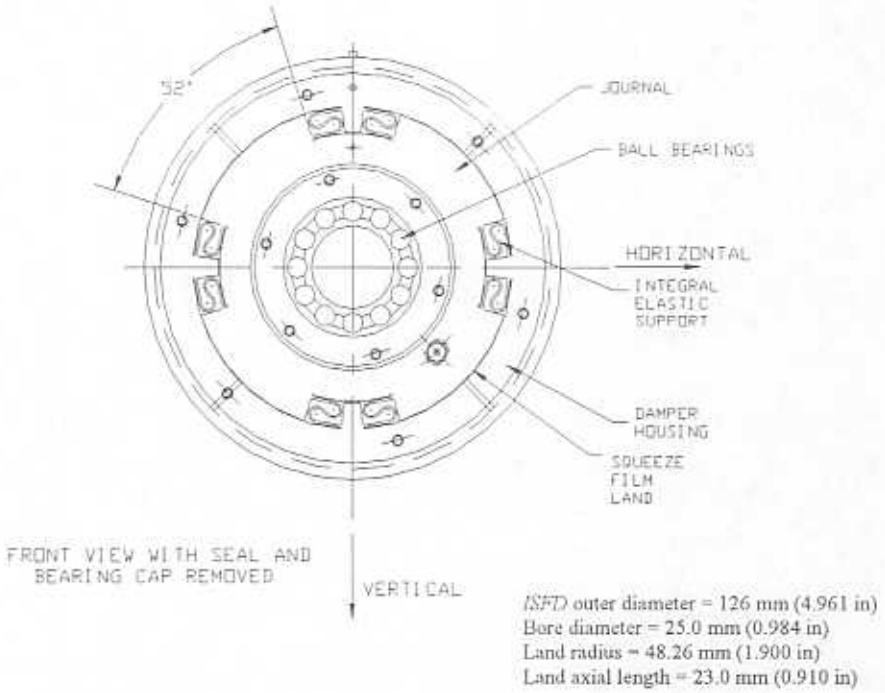

Figure 5. Integral *SFD* tested on rotor-*SFD* test rig.

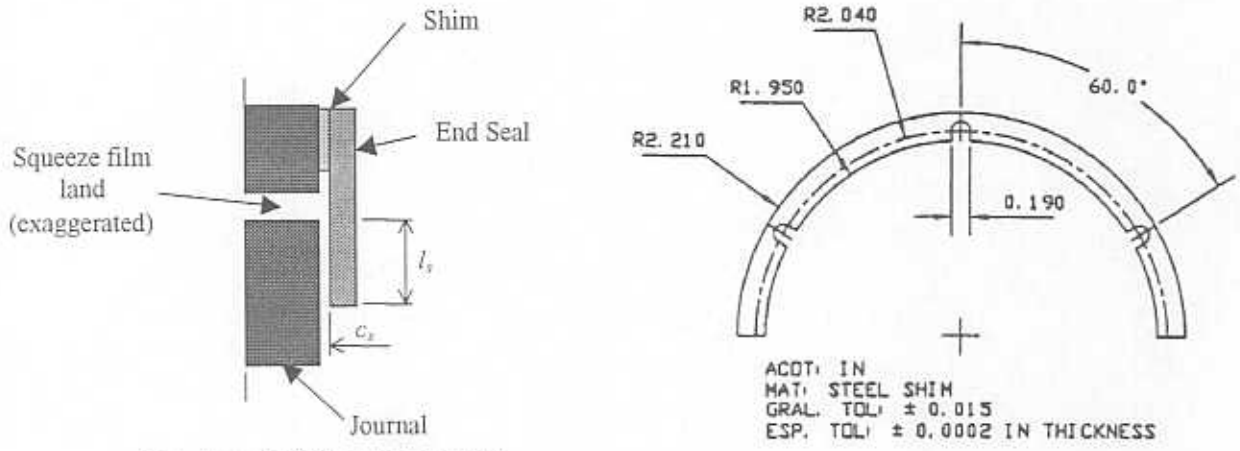

Side view of *ISFD* with end seals

Figure 6. Calibrated stainless steel stock shim and side view of the *ISFD* with end plate seal.

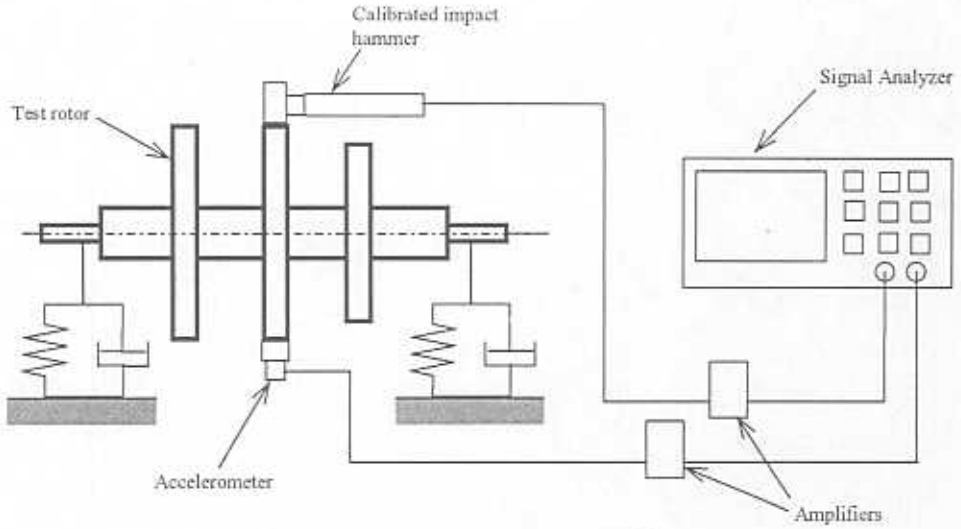

Figure 7. Instrumentation setup for impact tests.

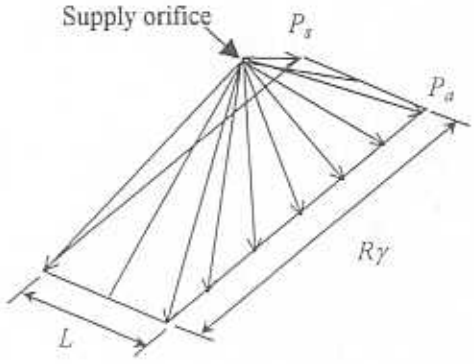

Simplified flow model for the open-ended configuration

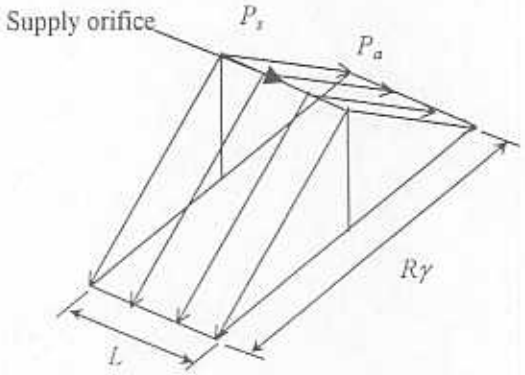

Simplified flow model for the sealed configuration

Figure 8. Flow models for the *ISFD*.

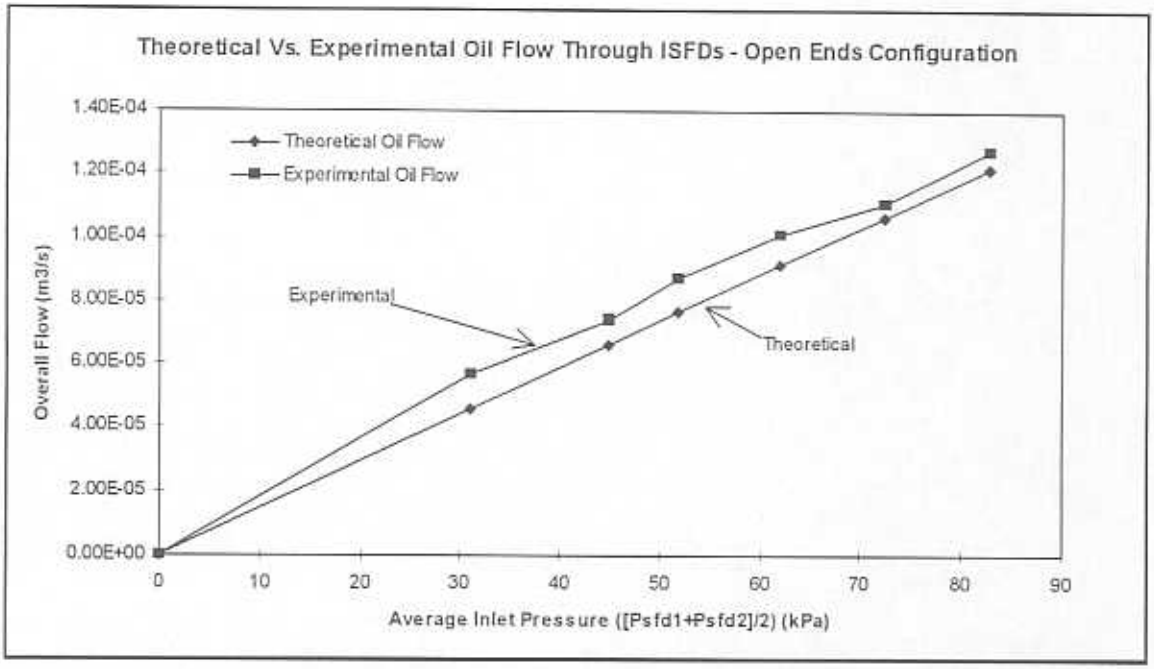

Figure 9. Comparison of *ISFD* theoretical and experimental overall oil flow rates. Open ended configuration.

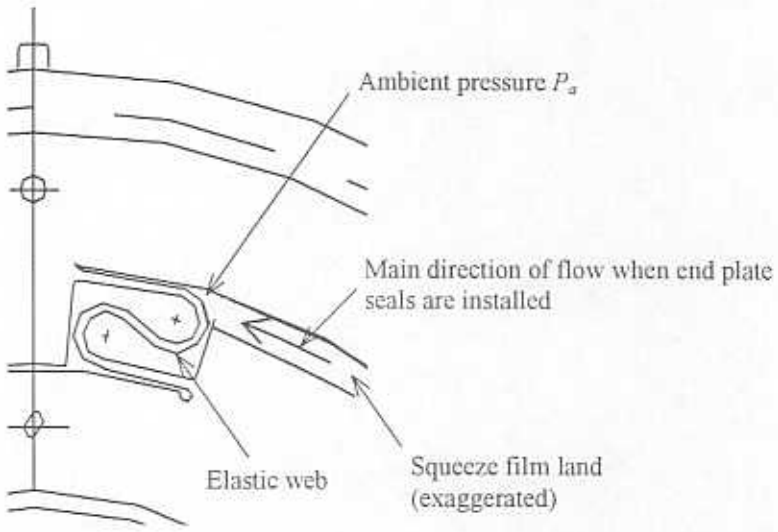

Figure 10. Detail of *ISFD* land construction.

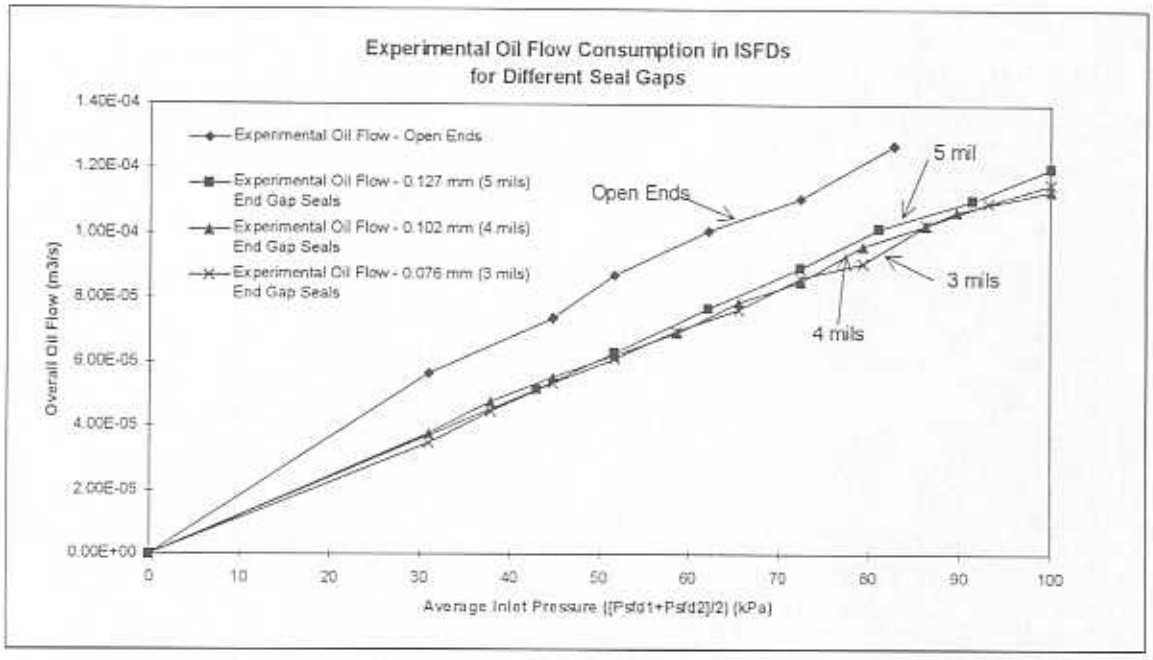

Figure 11. Experimental flow rates for different end seal gaps (*ISFDs*).

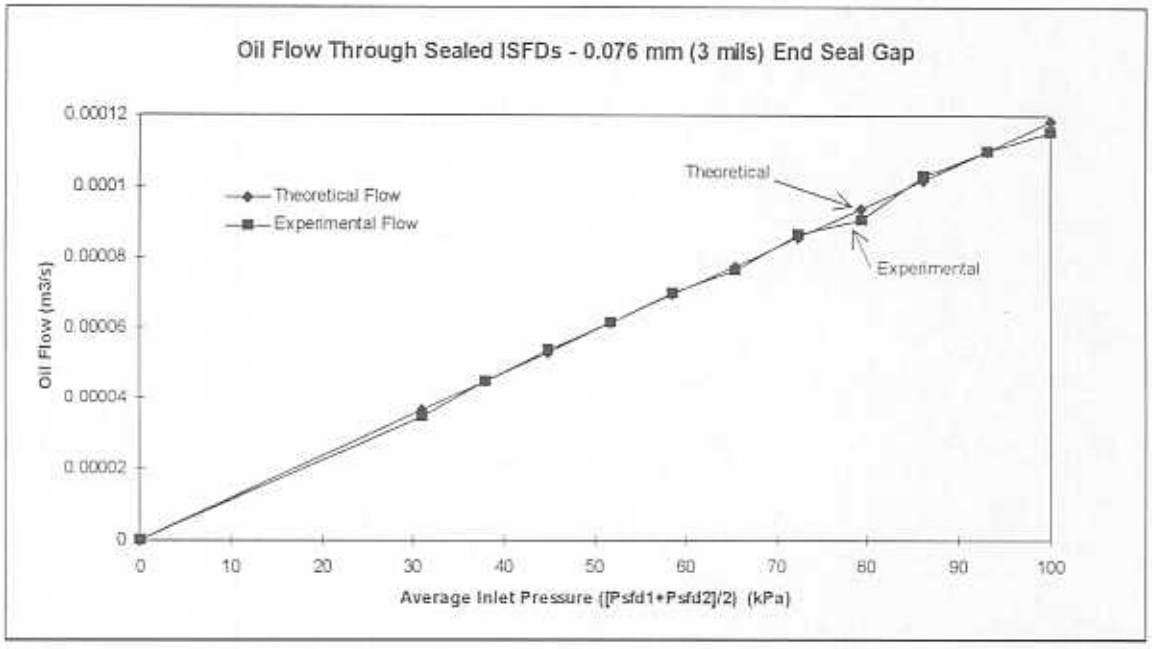

Figure 12. Comparison of *ISFD* theoretical and experimental oil flow rates.
0.076 mm (3 mils) end seal gap configuration.

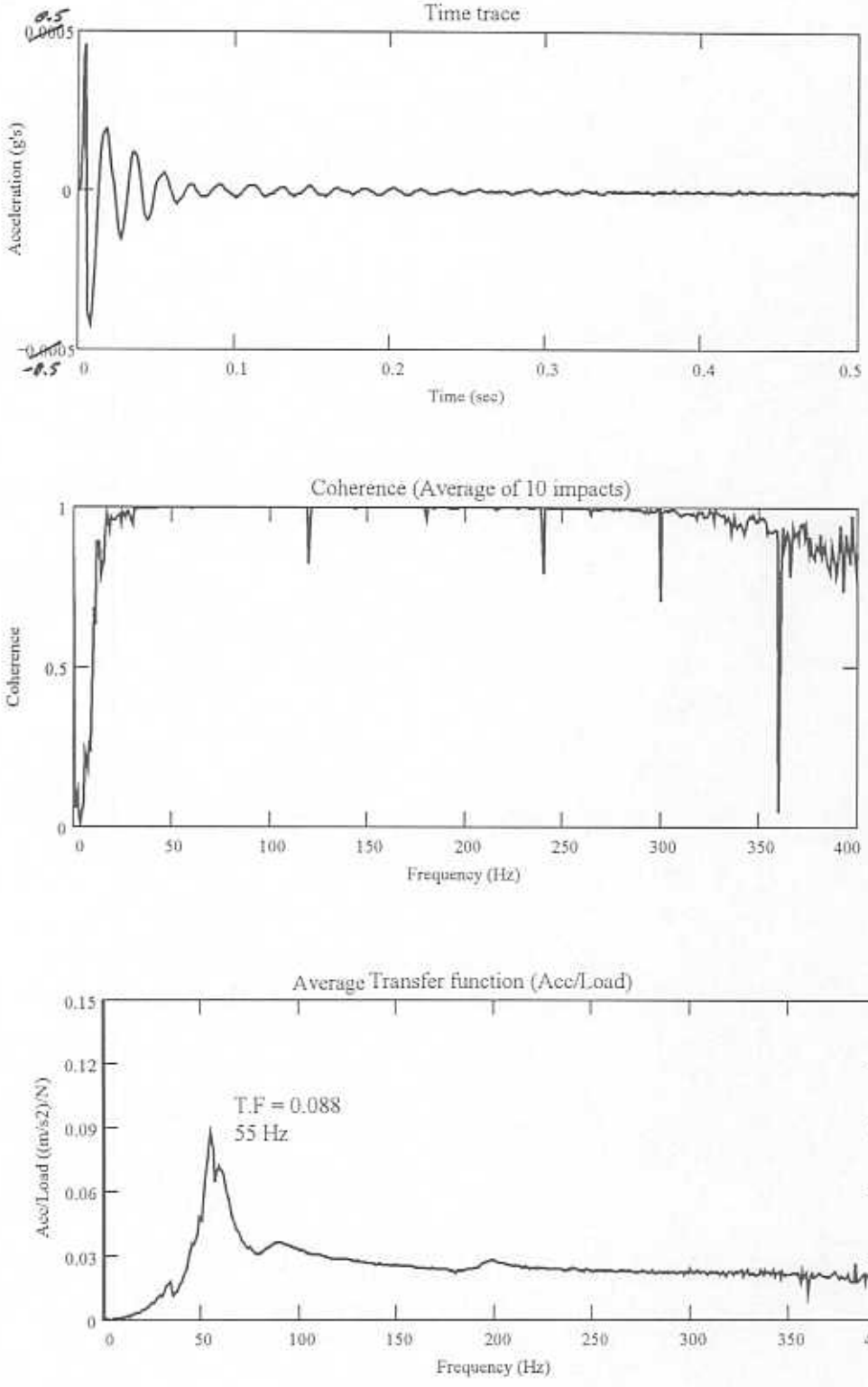

Figure 13a. Typical impact response test results. Integral dampers with 0.076 mm (3 mils) end gap seals. Vertical direction (Temperature = 37.7° C, 99.9° F).

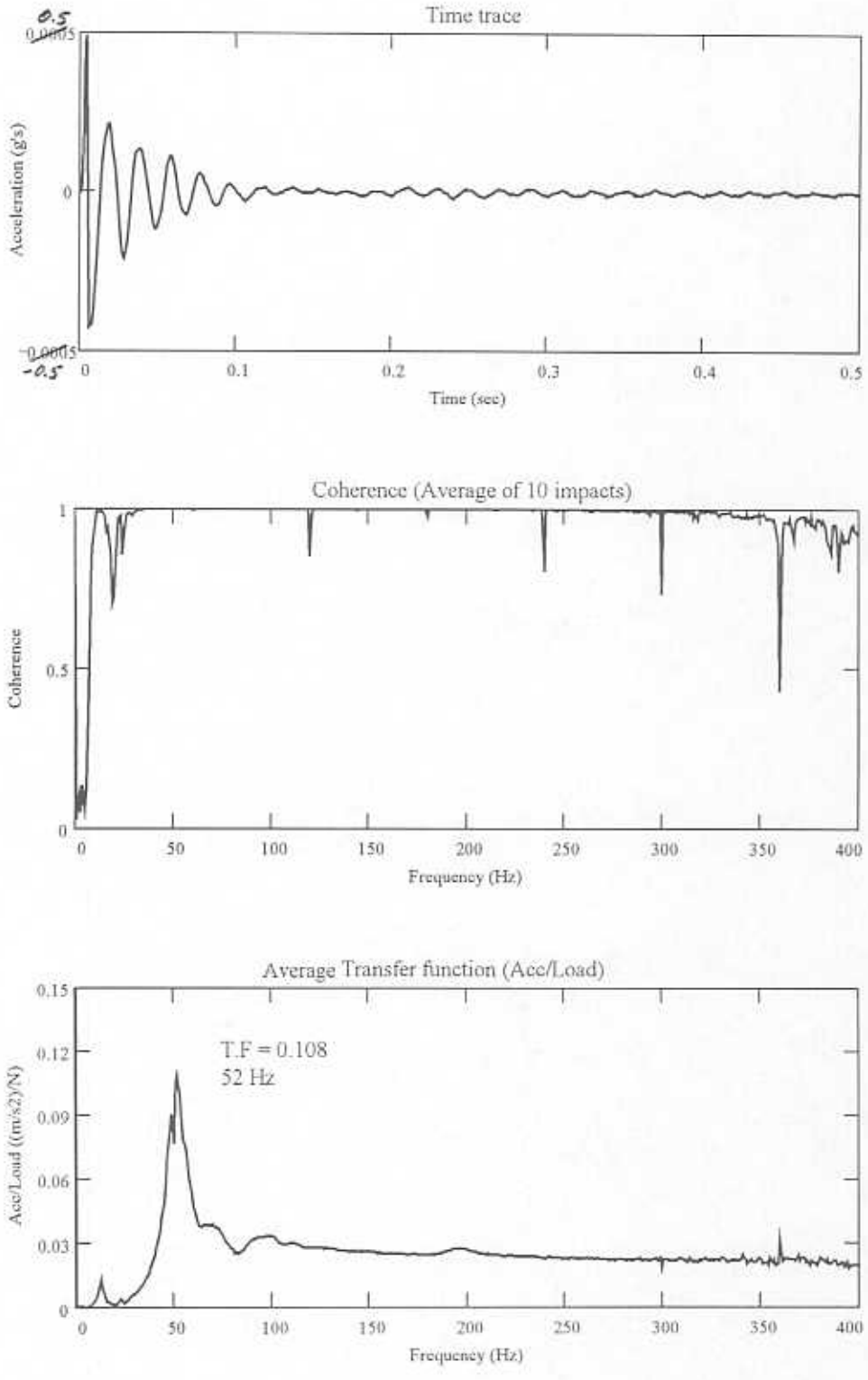

Figure 13b. Typical impact response test results. Integral dampers with 0.076 mm (3 mils) end gap seals. Horizontal direction (Temperature = 37.5° C, 99.5° F).

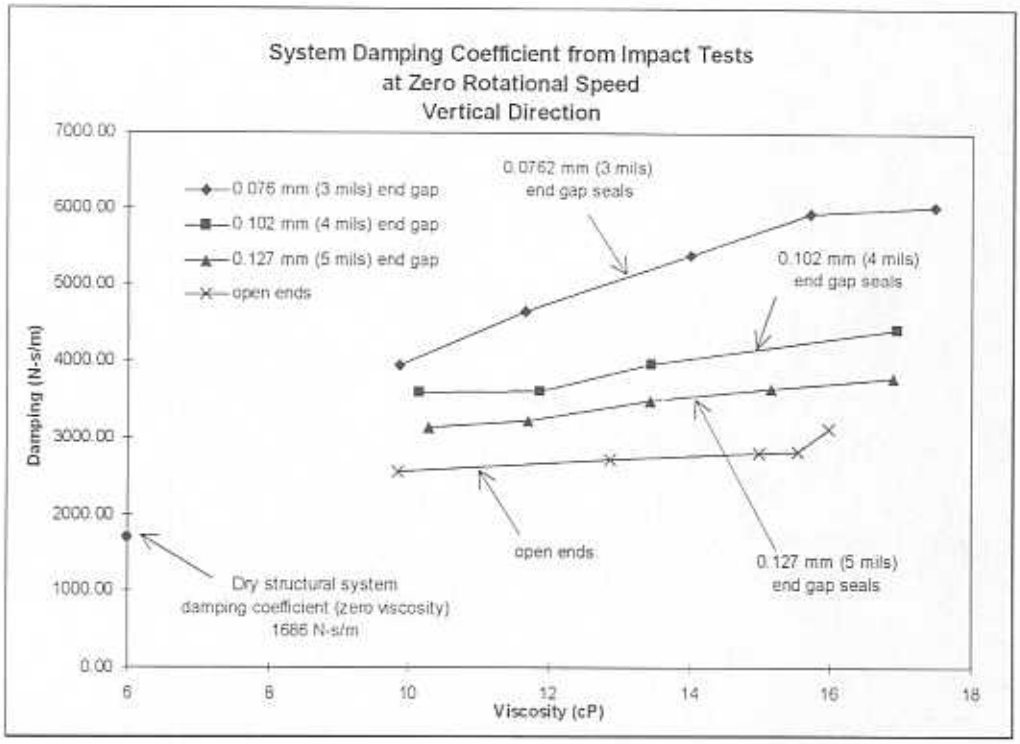

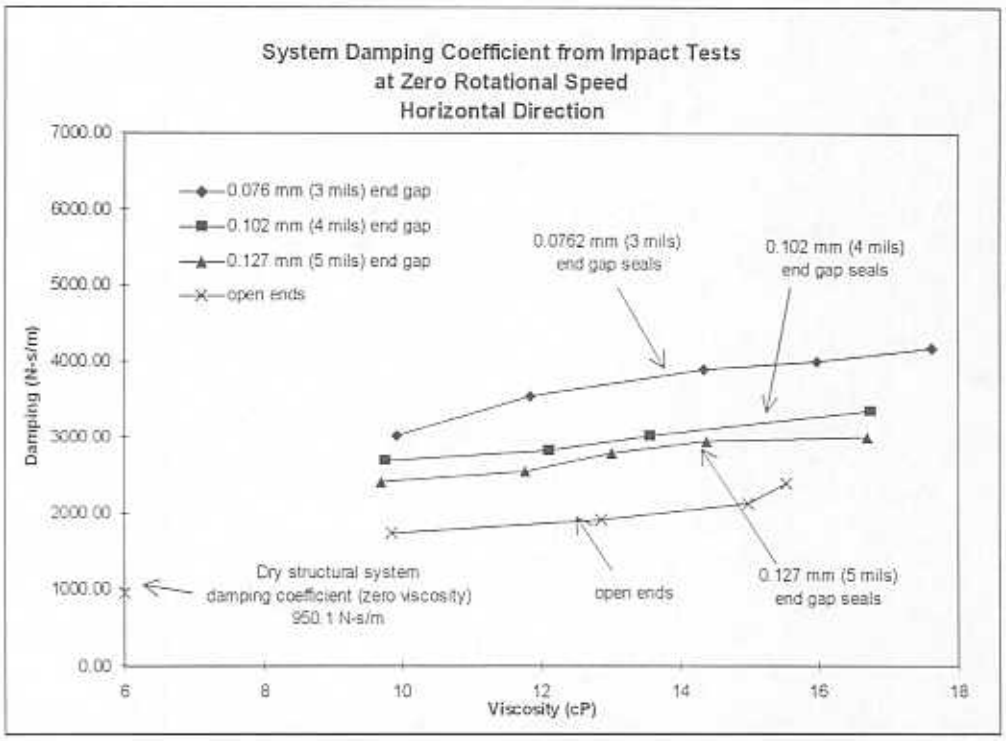

Figure 14. Summary of system damping coefficients of the rotor on sealed dampers from impact tests versus lubricant viscosity. Vertical and horizontal directions.

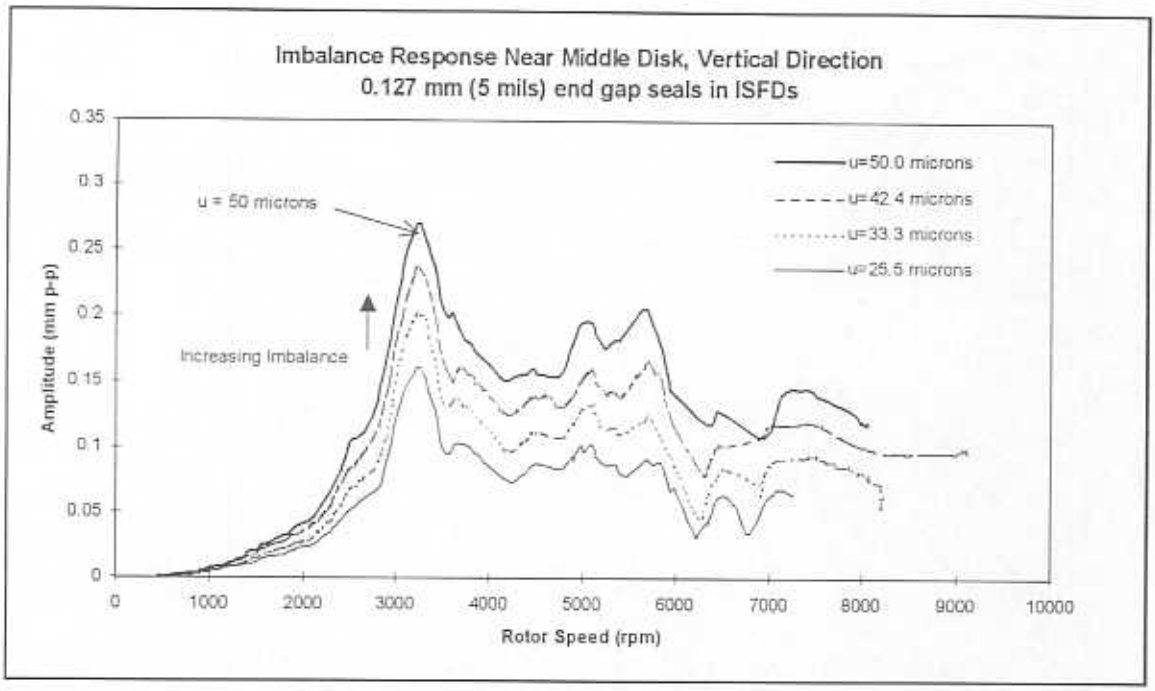

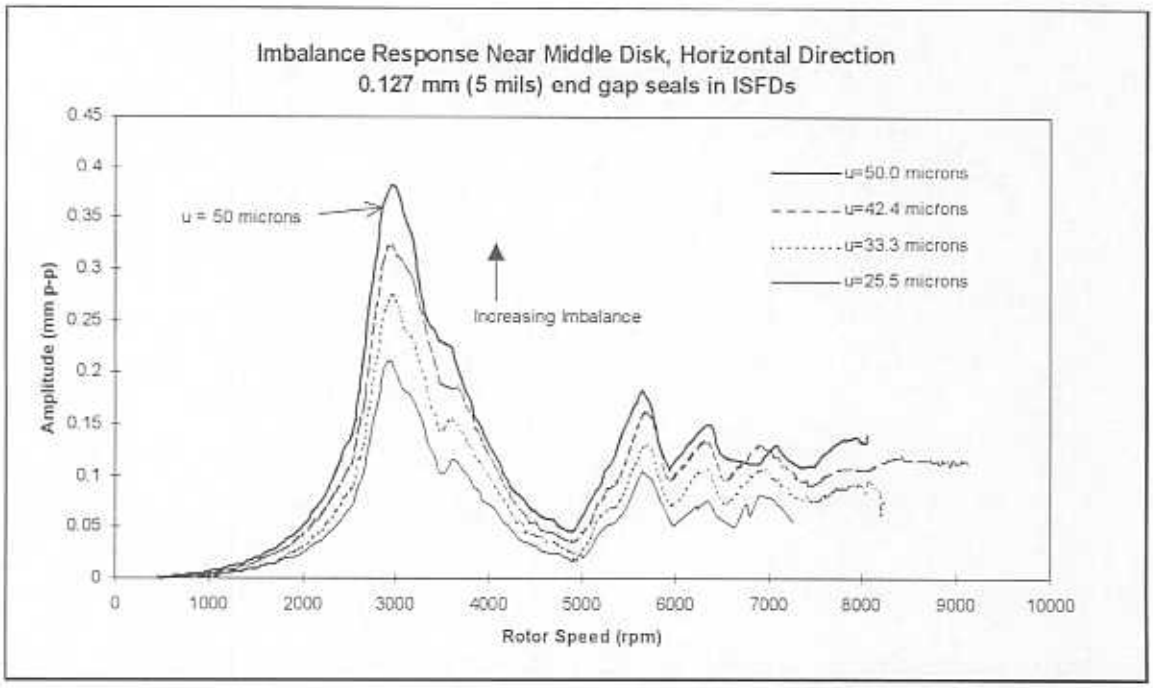

Figure 15a. Imbalance response of the test rotor supported on sealed *ISFDs* for different levels of imbalance. Vertical and horizontal directions. Measurements at near middle disk. 0.127 mm (5 mils) end gap seals.

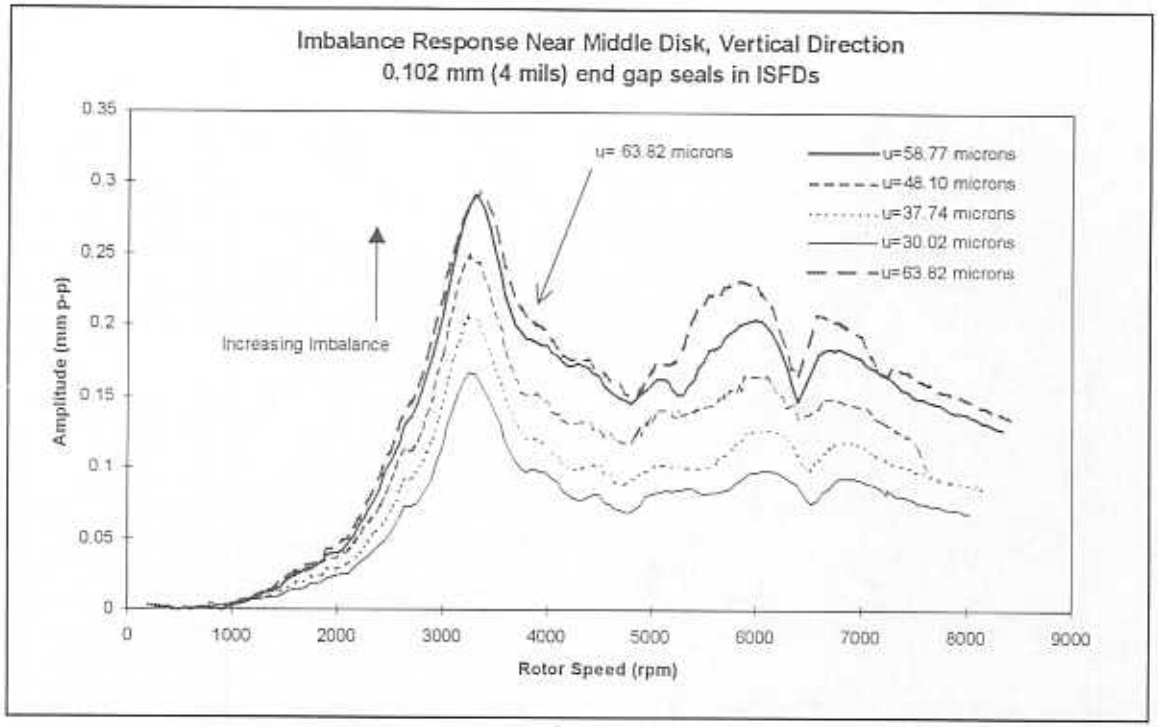

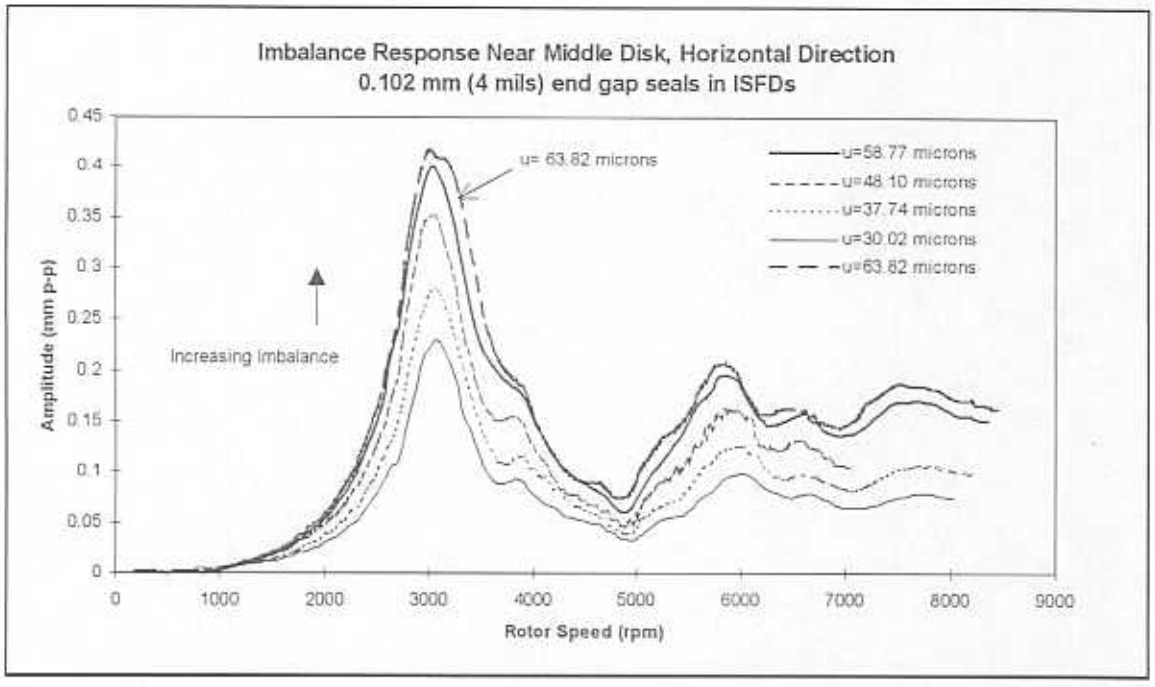

Figure 15b. Imbalance response of the test rotor supported on sealed *ISFDs* for different levels of imbalance. Vertical and horizontal directions. Measurements at near middle disk. 0.102 mm (4 mils) end gap seals.

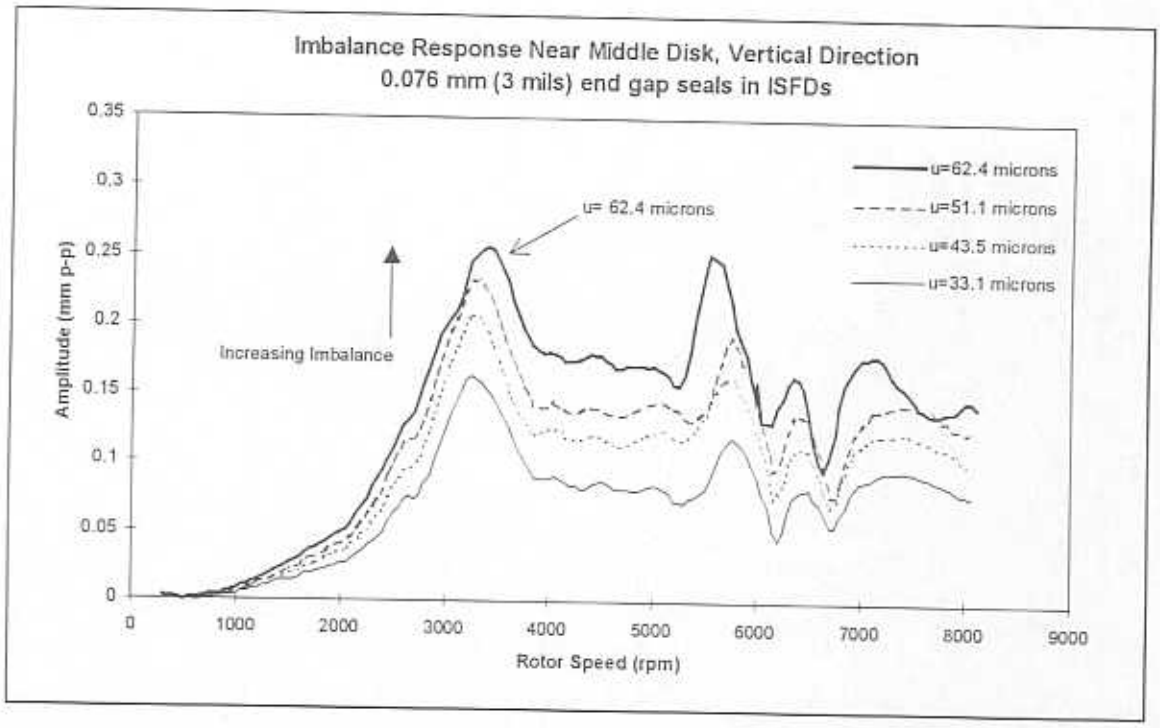

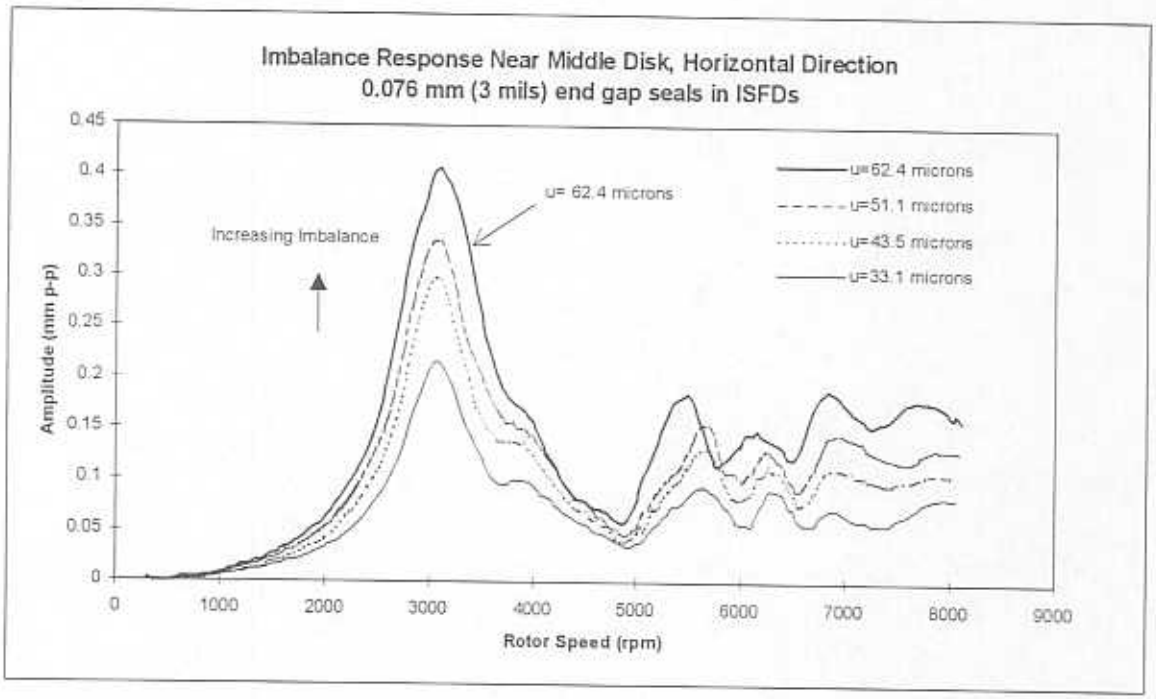

Figure 15c. Imbalance response of the test rotor supported on sealed *ISFDs* for different levels of imbalance. Vertical and horizontal directions. Measurements at near middle disk. 0.076 mm (3 mils) end gap seals.

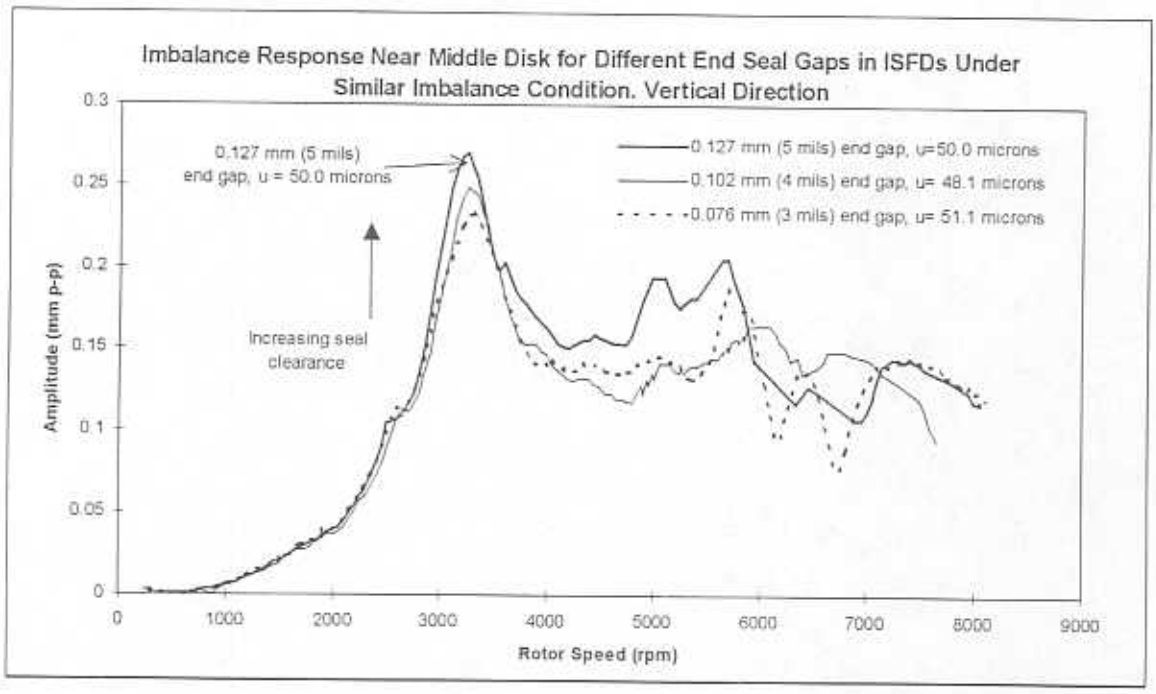

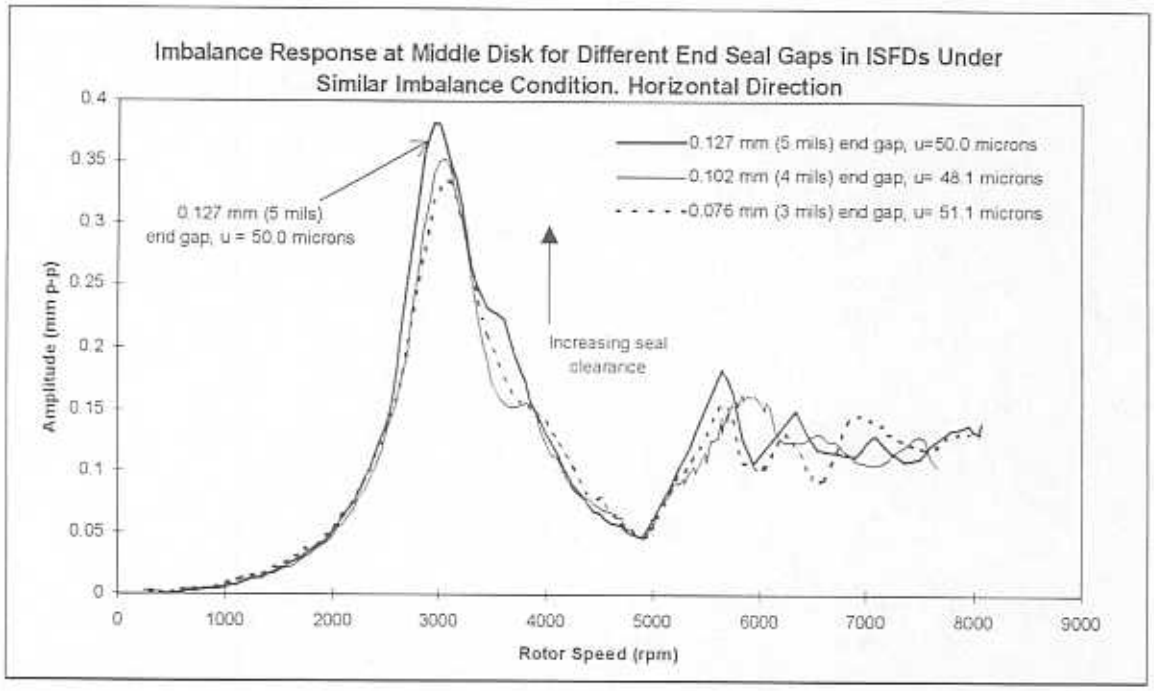

Figure 16. Comparisons of rotor imbalance responses near the middle disk for different end seal and gaps for similar imbalance conditions.

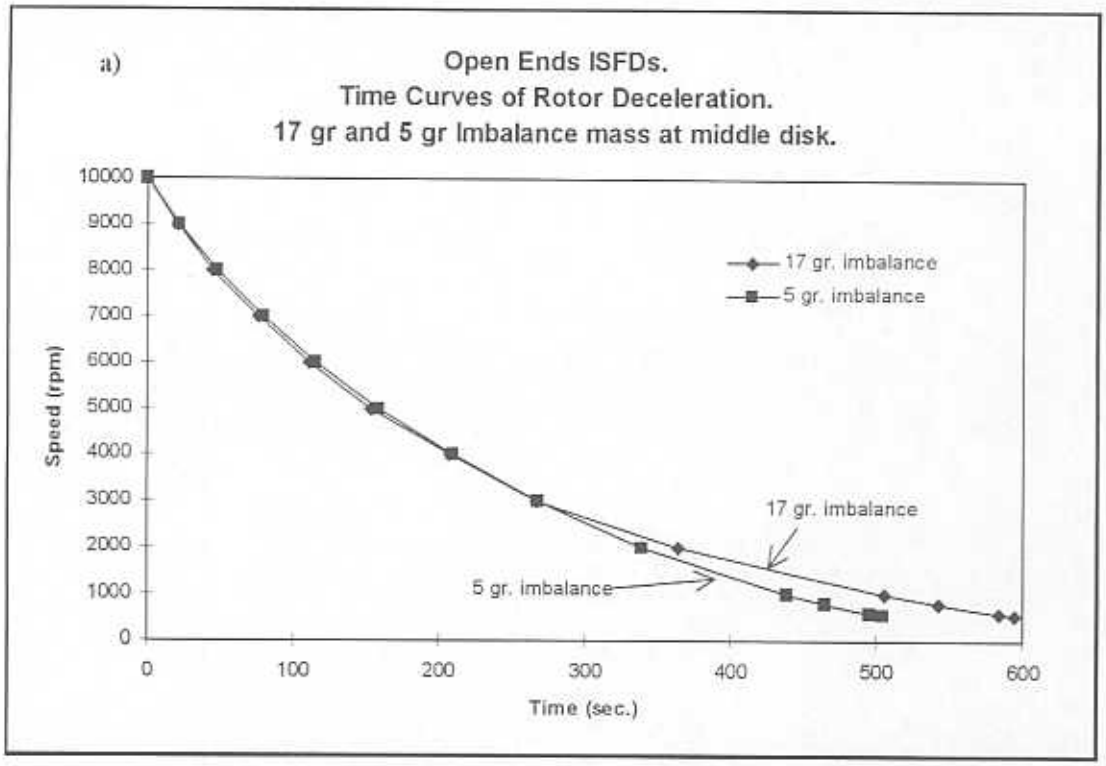

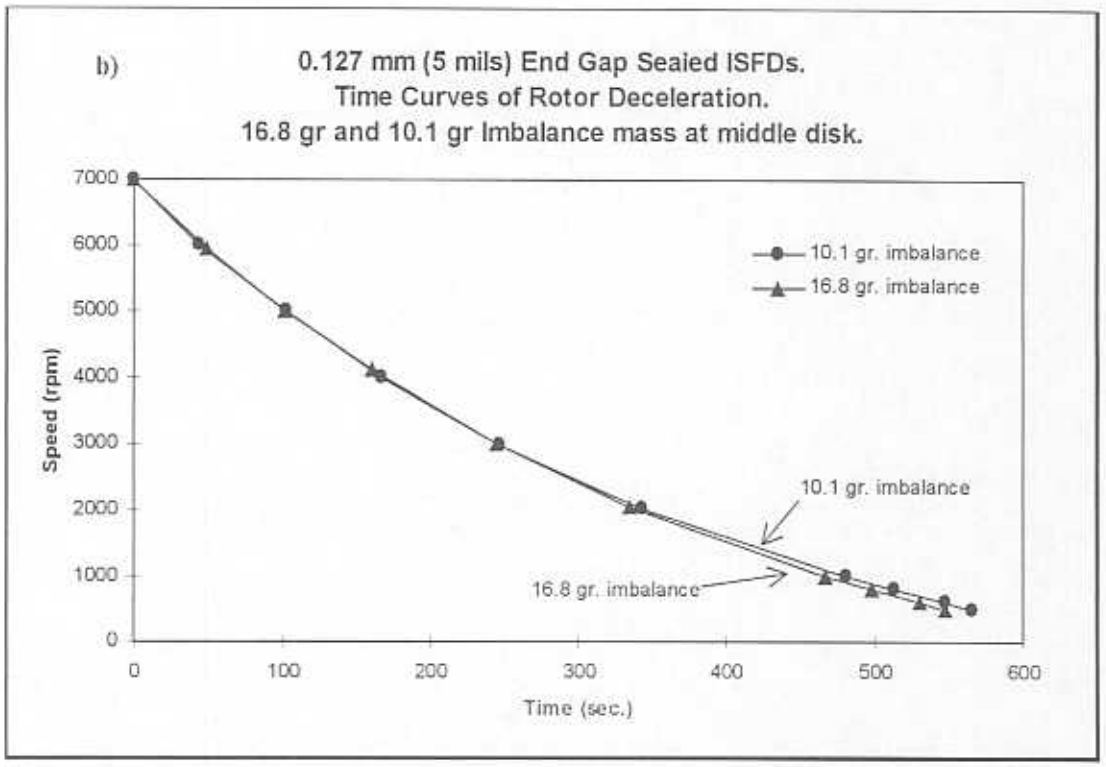

Figure 17. Rotor speed decay curves for different imbalance conditions.
a) Open ended *ISFDs.*
b) 0.127 mm (5 mils) end gap seals on *ISFDs.*

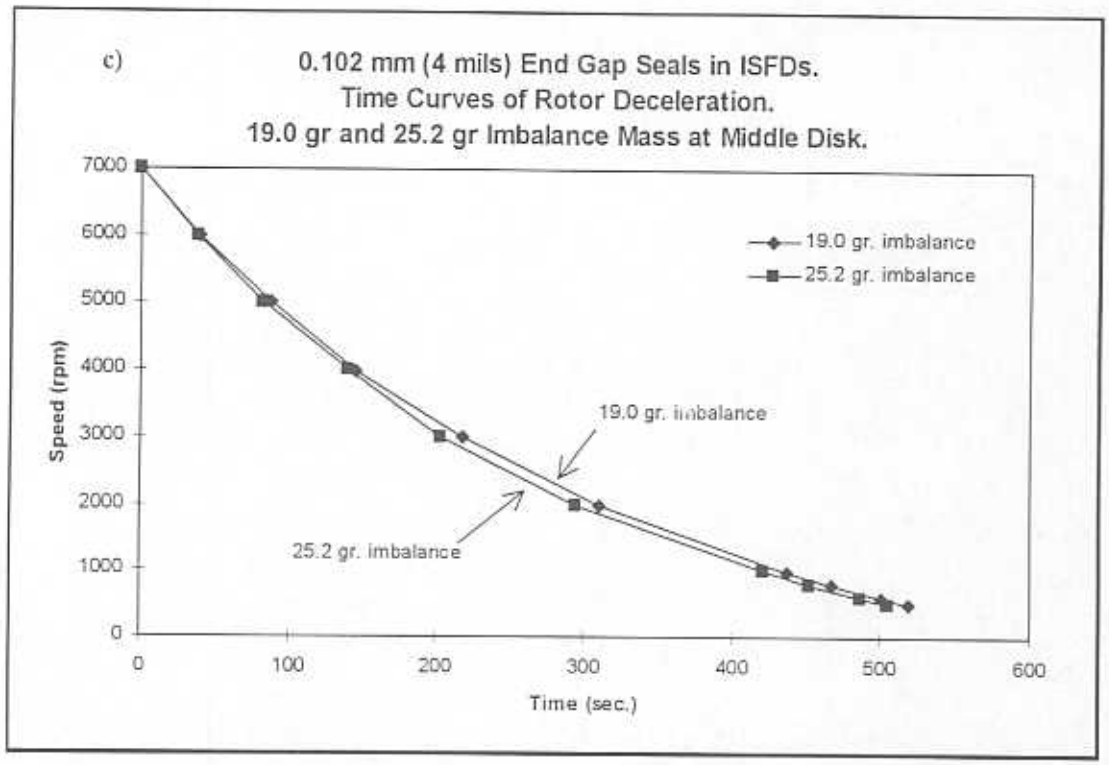

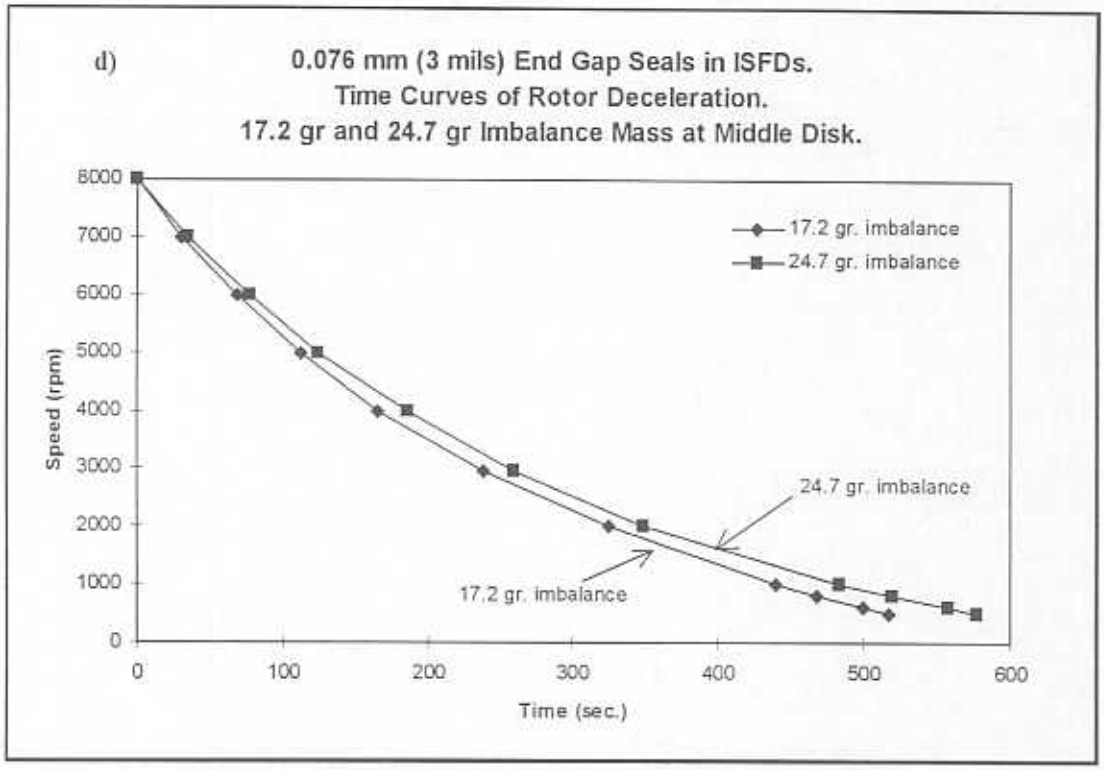

Figure 17. Rotor speed decay curves for different imbalance conditions.
c) 0.102 mm (4 mils) end gap seals on *ISFDs*.
d) 0.076 mm (3 mils) end gap seals on *ISFDs*.

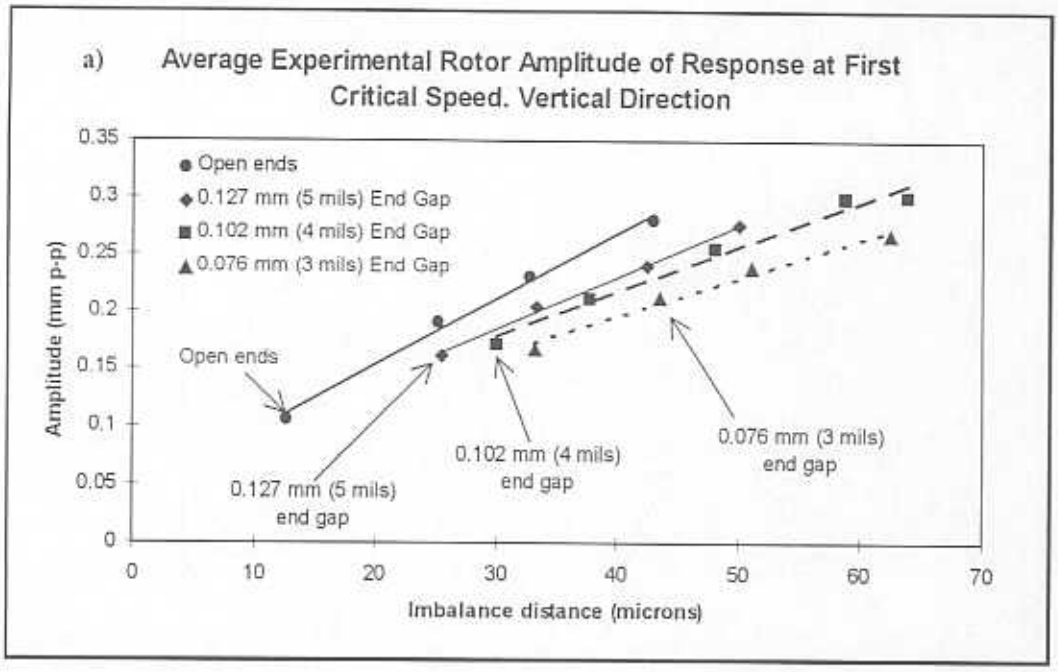

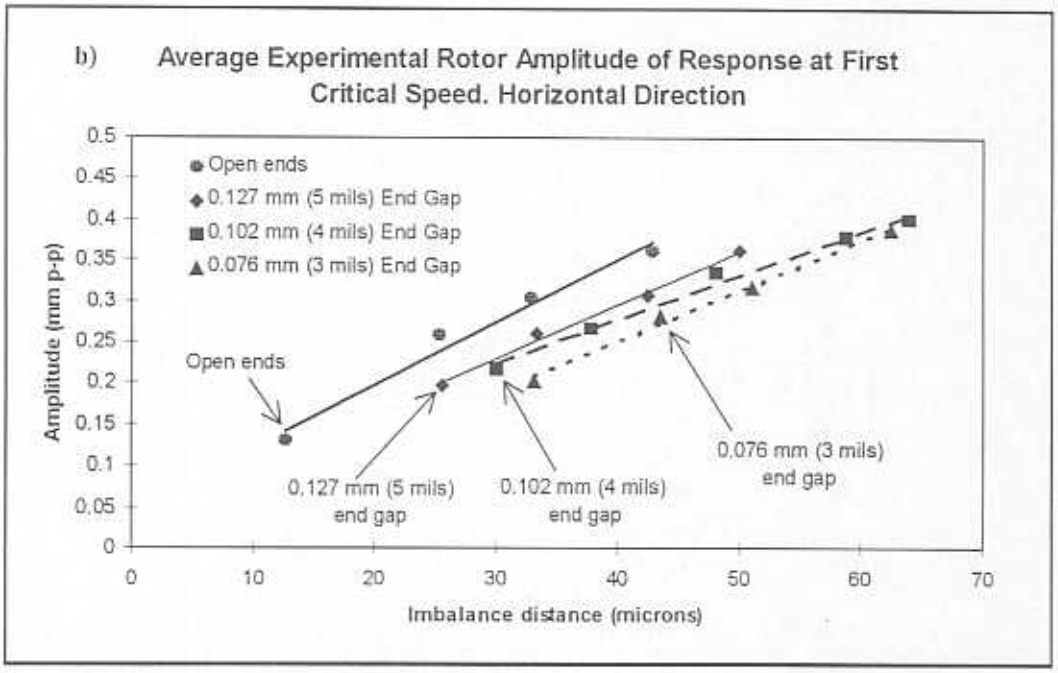

Figure 18. Average rotor amplitude of response at first critical speed versus imbalance distance for different end seal gaps on integral *SFDs*.
a) Vertical.
b) Horizontal.

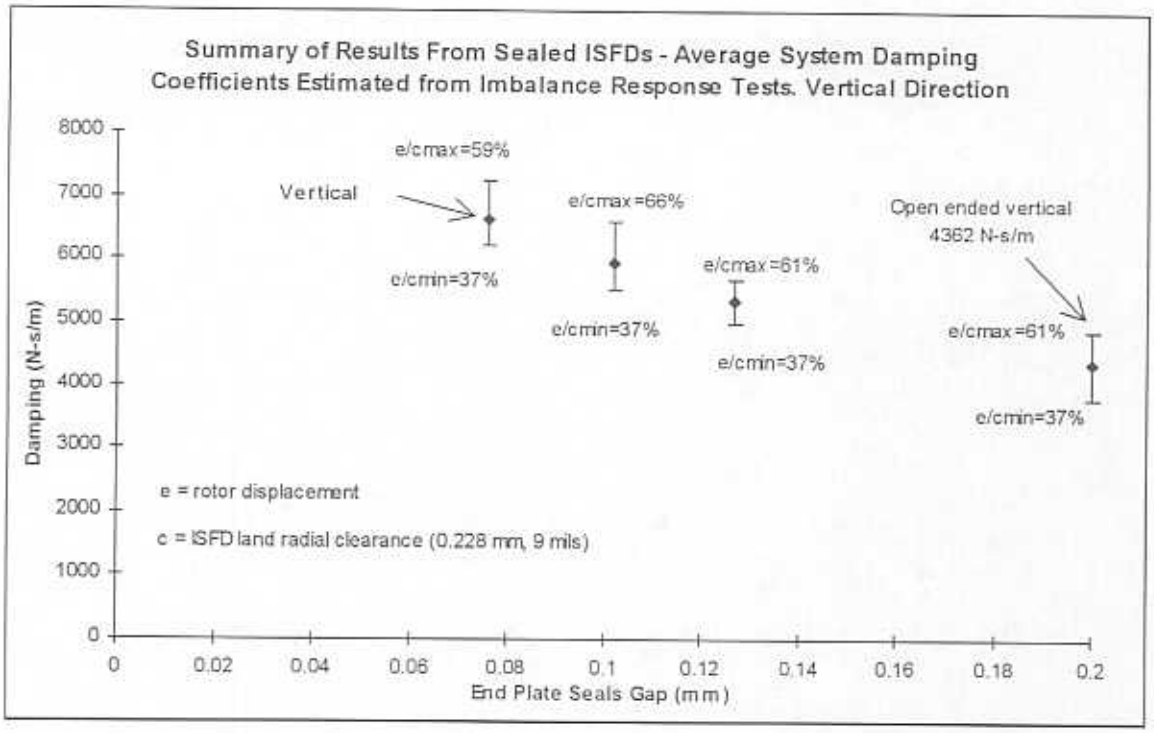

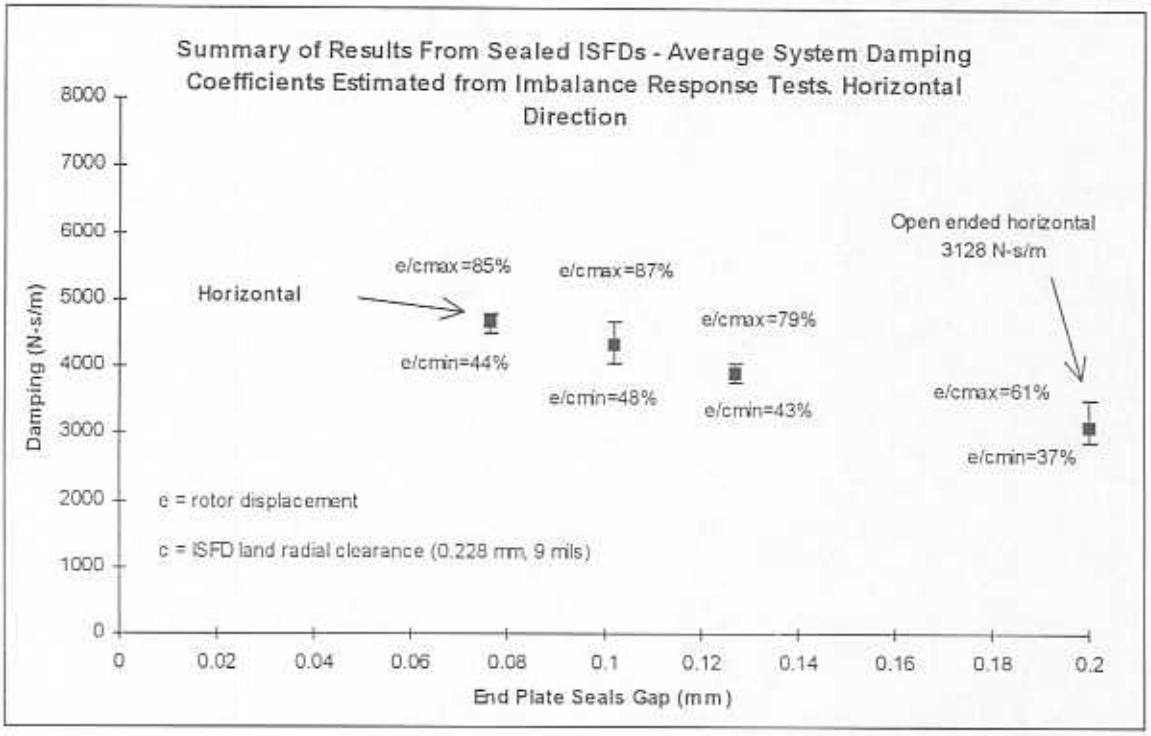

Figure 19. Summary of average system damping coefficients versus end seal gaps as estimated from rotor imbalance response tests including the maximum and minimum ranges of orbit eccentricity for every seal condition.

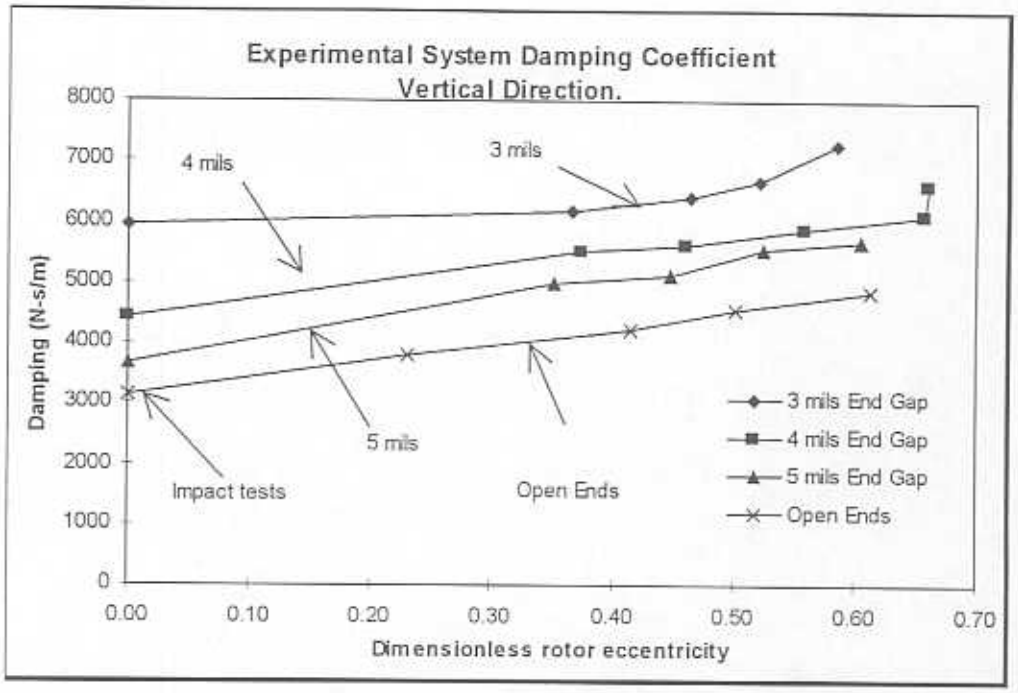

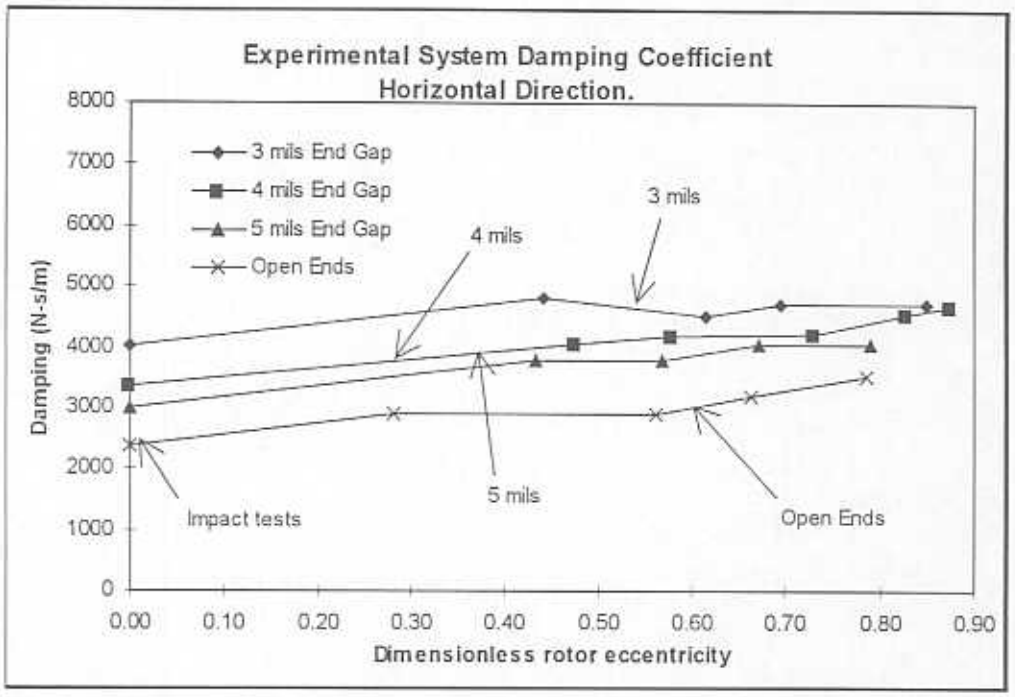

Figure 20. Experimental system damping coefficient estimated from rotor imbalance response versus rotor eccentricity, including results from impact response tests (zero eccentricity).

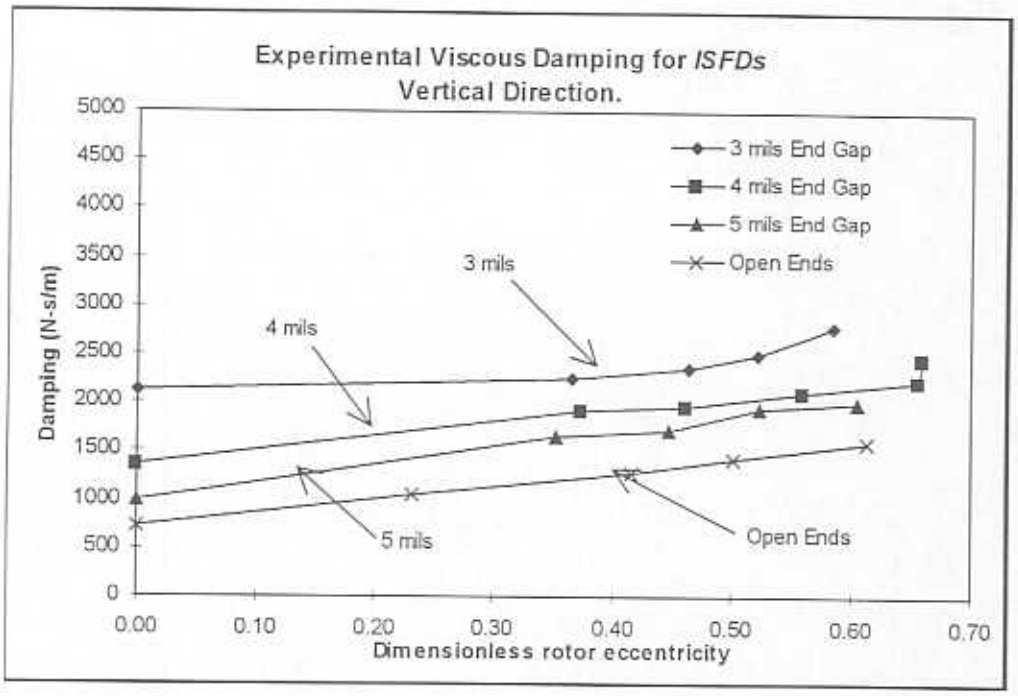

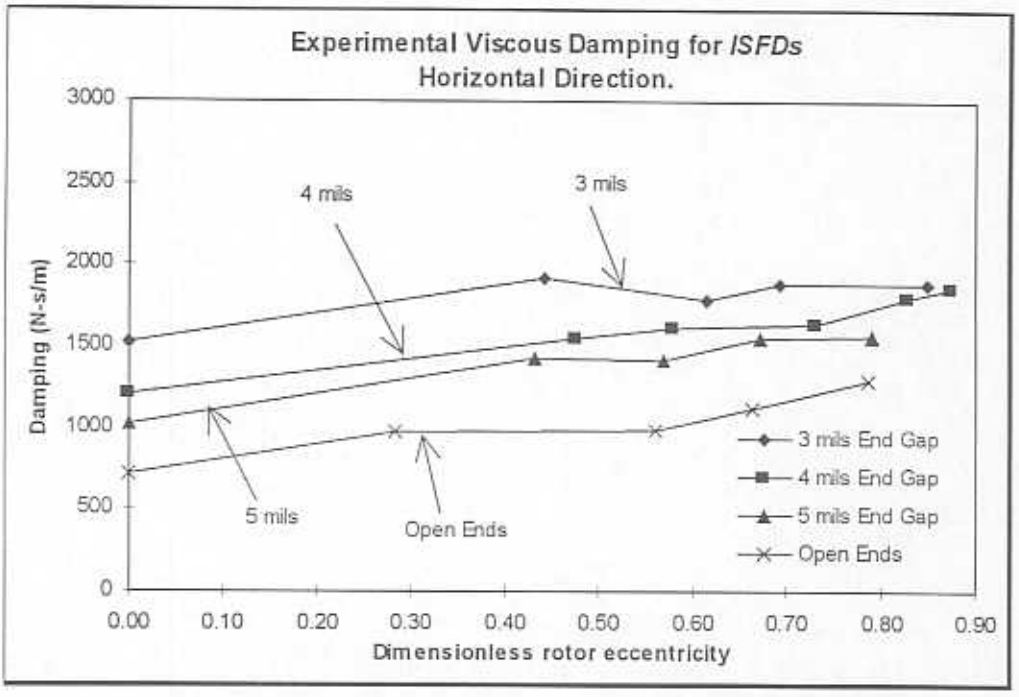

Figure 21a. Experimental damping coefficients for each *ISFD*.
Damping coefficients in physical units.

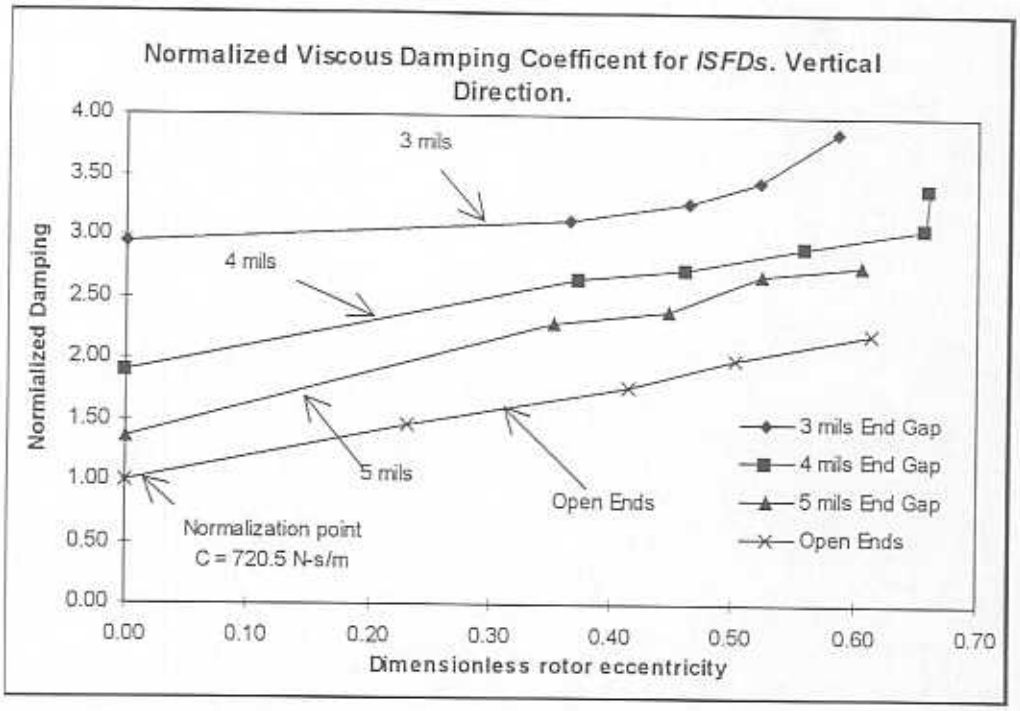

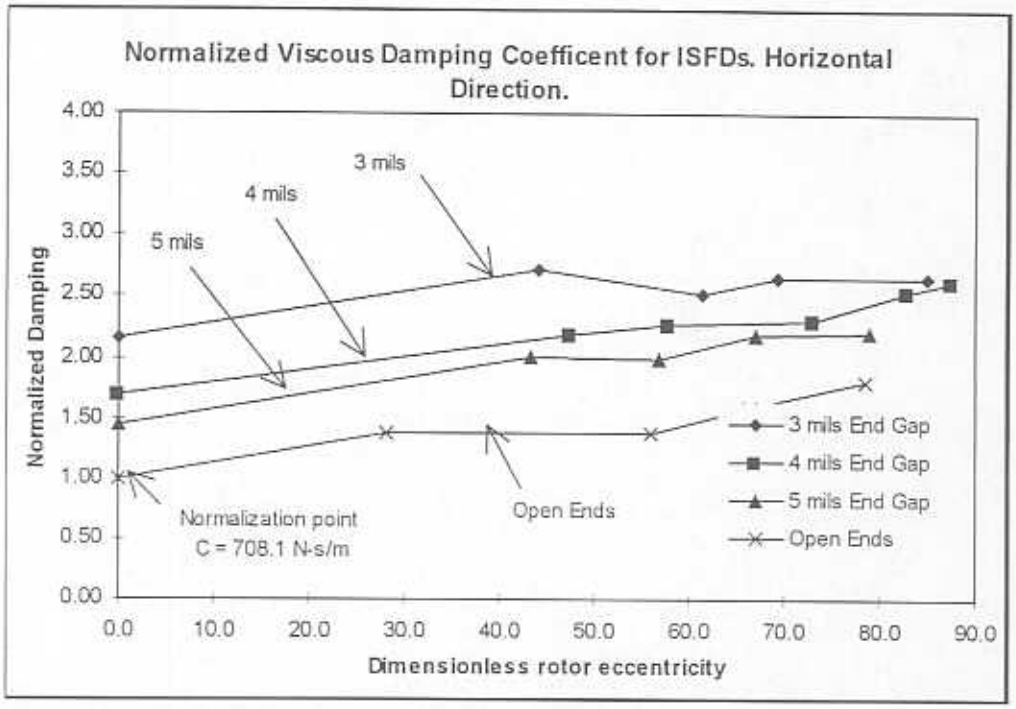

Figure 21b. Experimental damping coefficients for each *ISFD*.
Normalized damping coefficients with respect to
the open ended *ISFDs* damping values from impact tests.

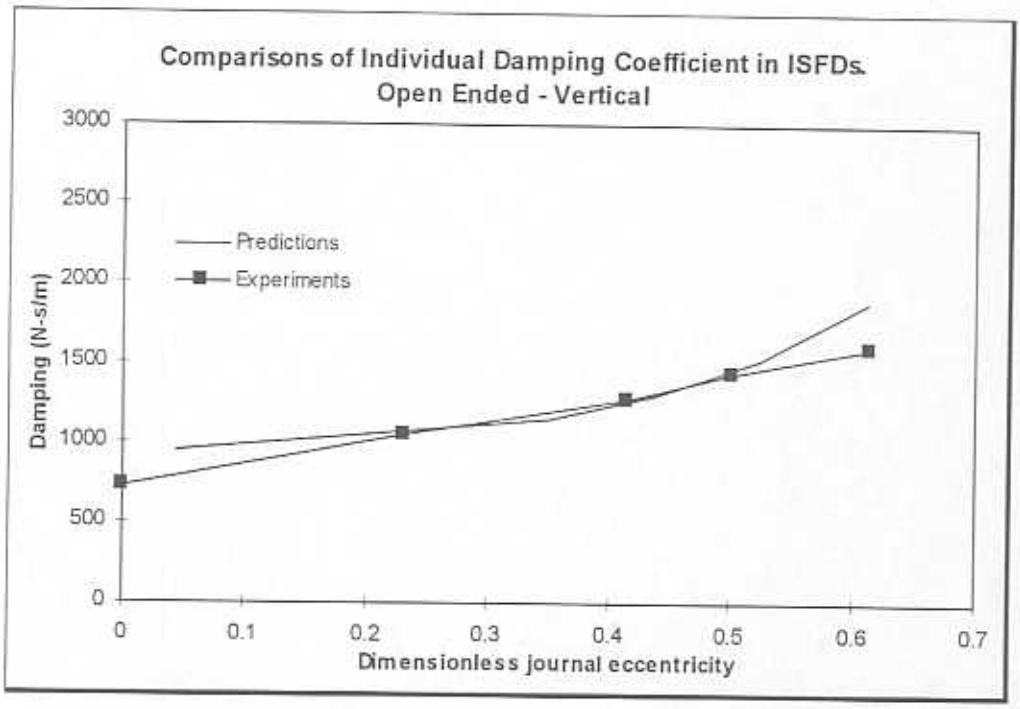

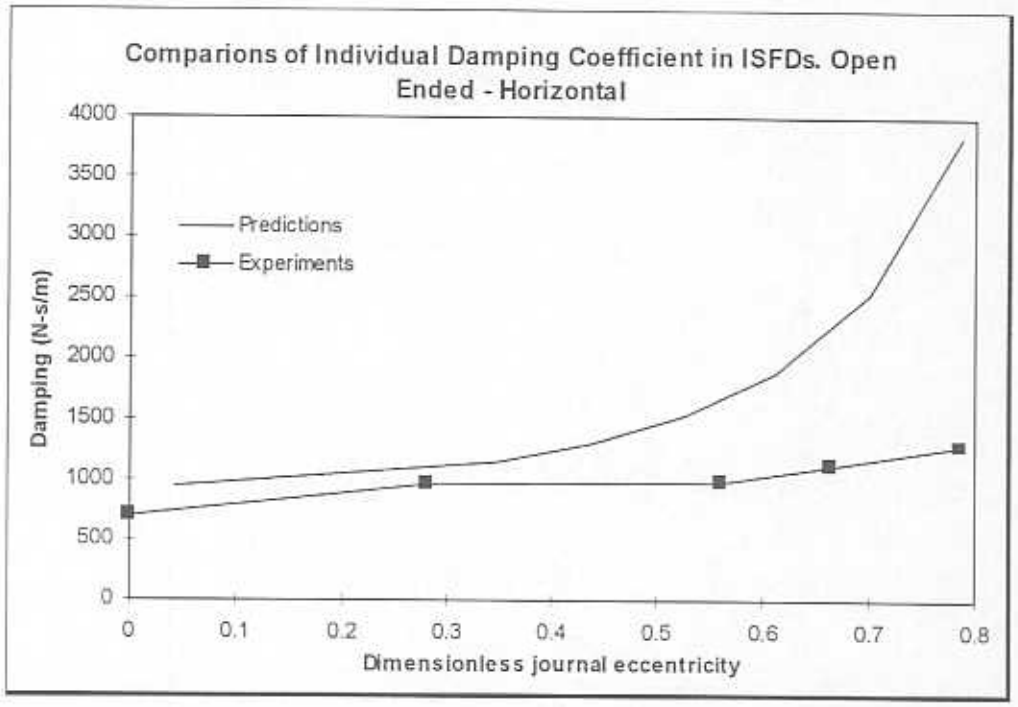

Figure 22a. Comparisons of experimental and predicted damping coefficients for the *ISFDs* Open ended configuration, full film model.

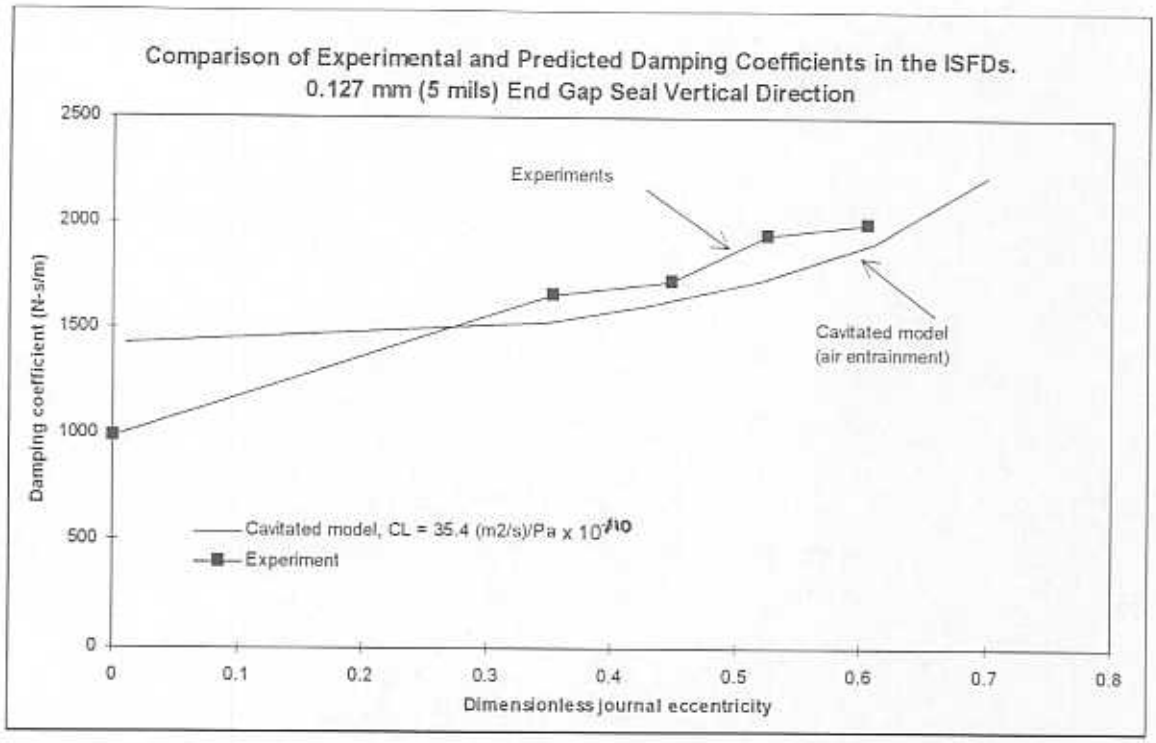

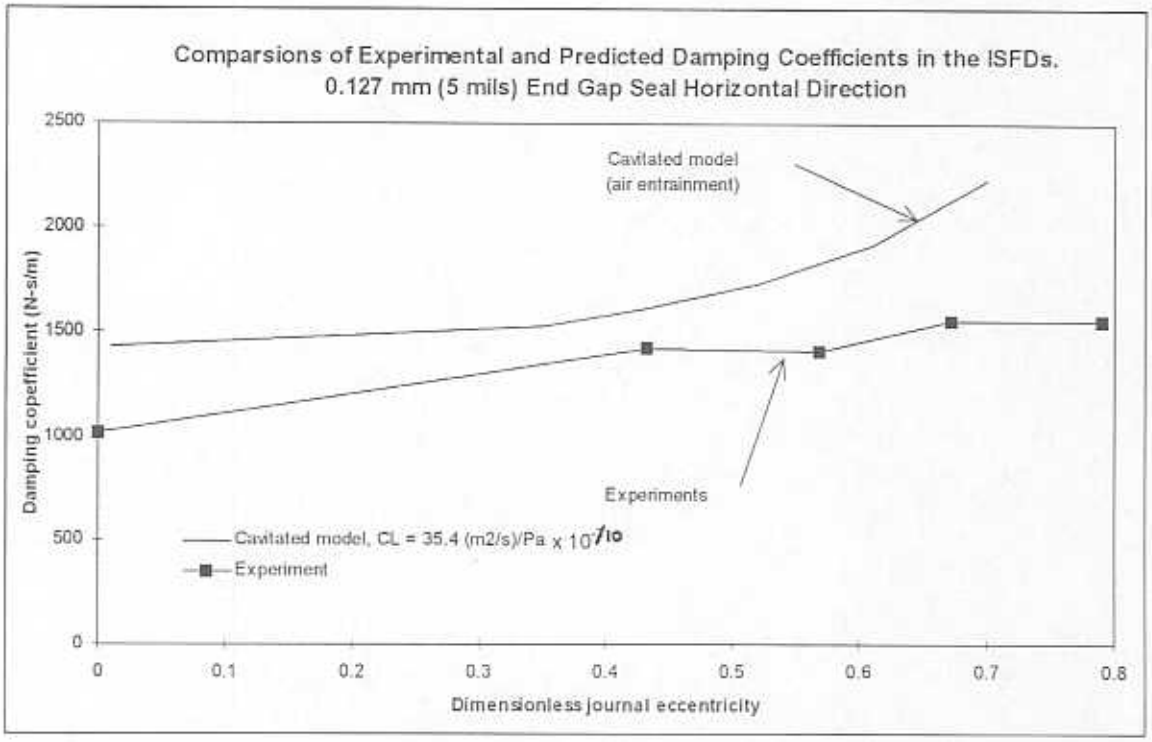

Figure 22b. Comparisons of experimental and predicted damping coefficients for the *ISFDs* 0.127 mm (5 mils) end gap seal.

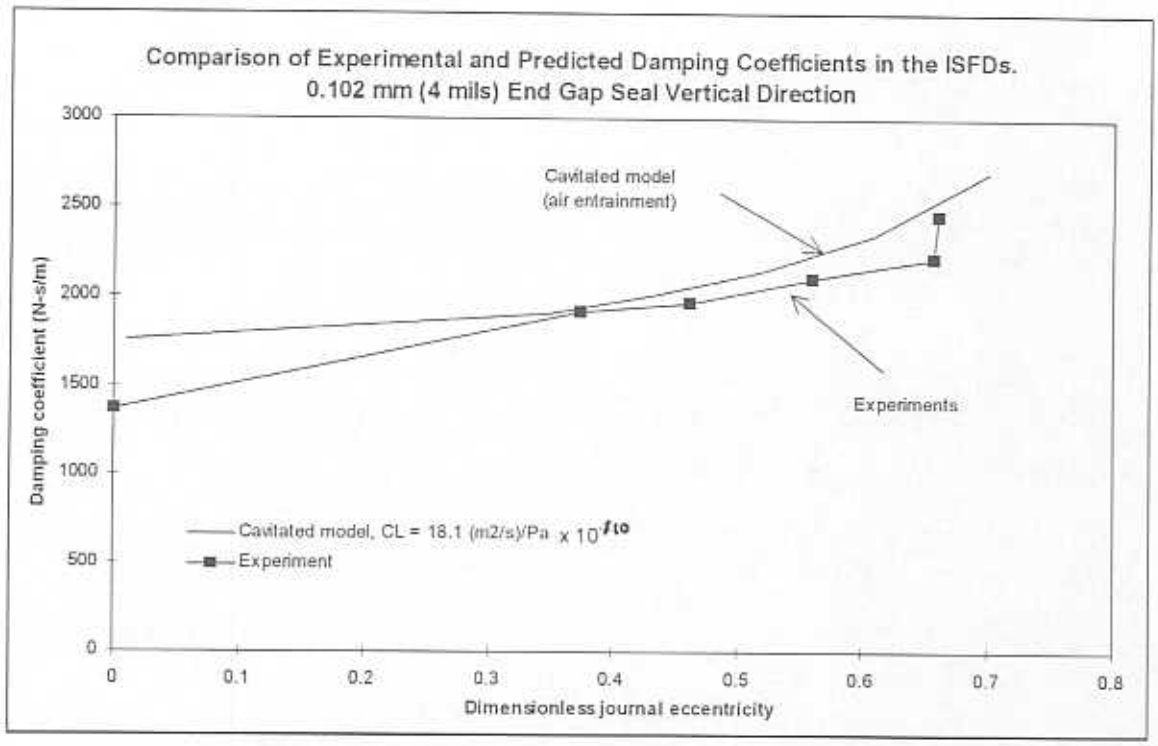

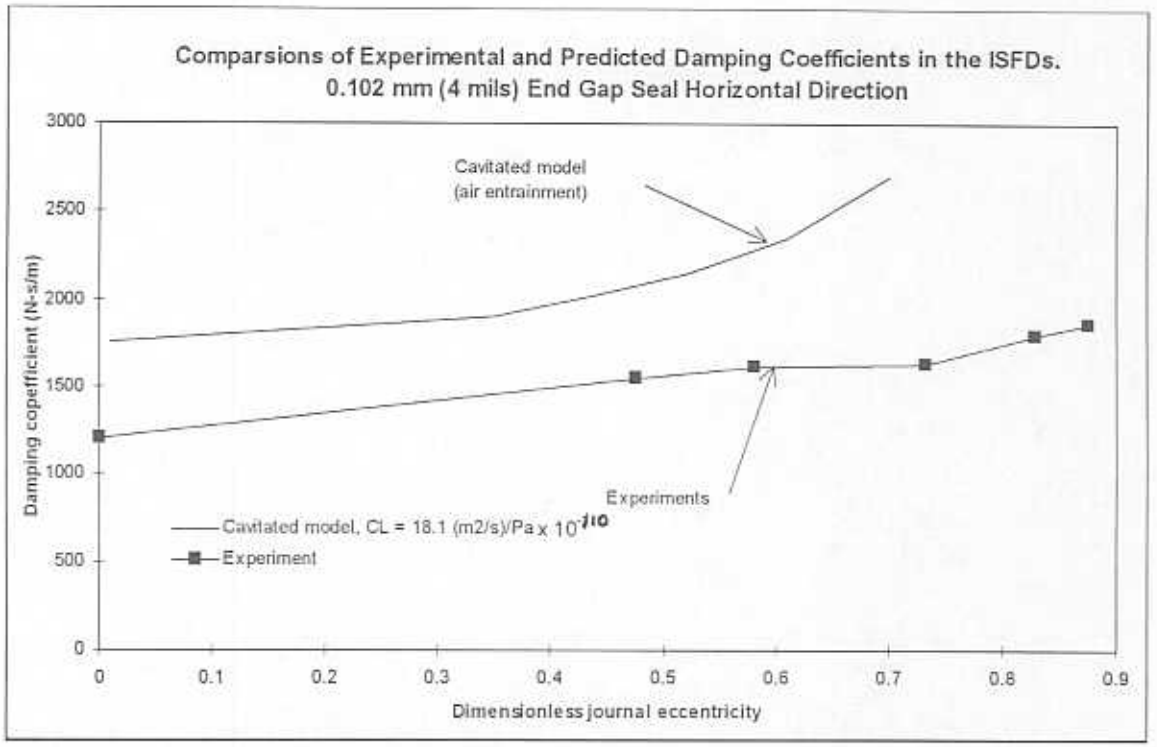

Figure 22c. Comparisons of experimental and predicted damping coefficients for the *ISFDs* 0.102 mm (4 mils) end gap seal.

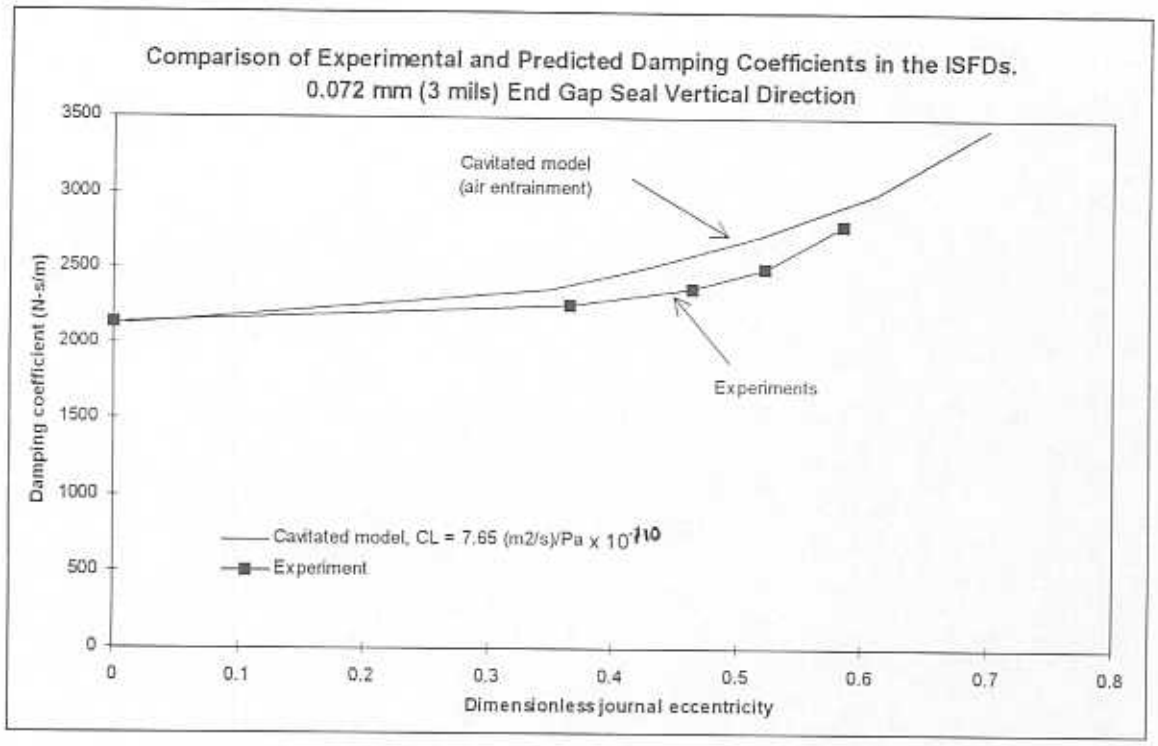

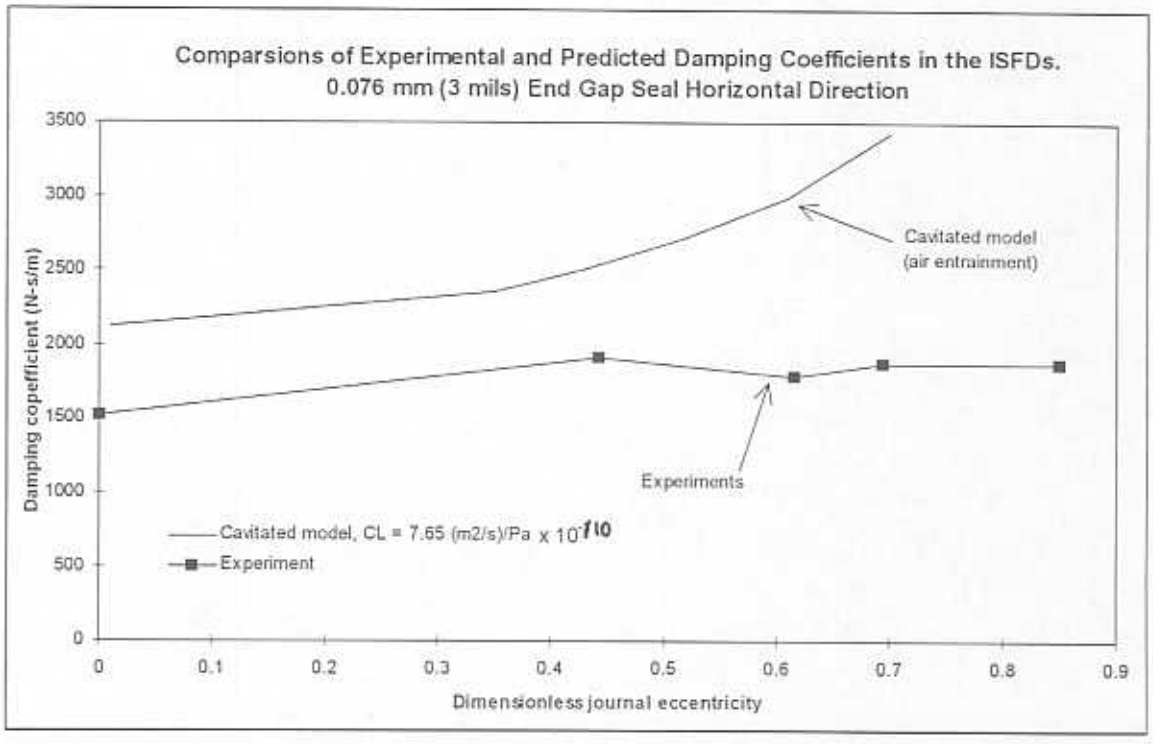

Figure 22d. Comparisons of experimental and predicted damping coefficients for the *ISFDs* 0.076 mm (3 mils) end gap seal.

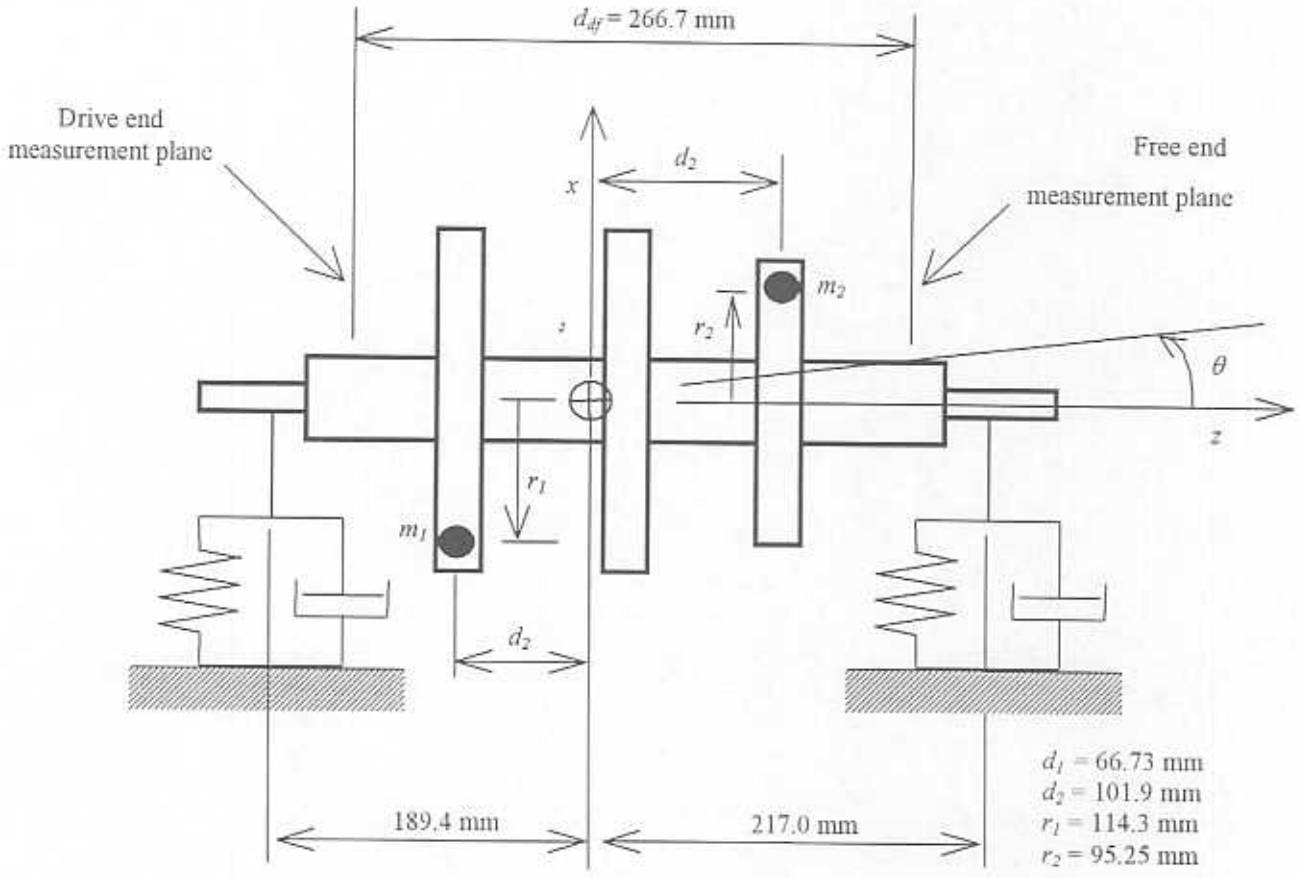

$$J_{xz} = m_1 d_1 r_1 + m_2 d_2 r_2$$

Figure 23. Position of imbalance masses on rotor disks producing an excitation moment of inertia.

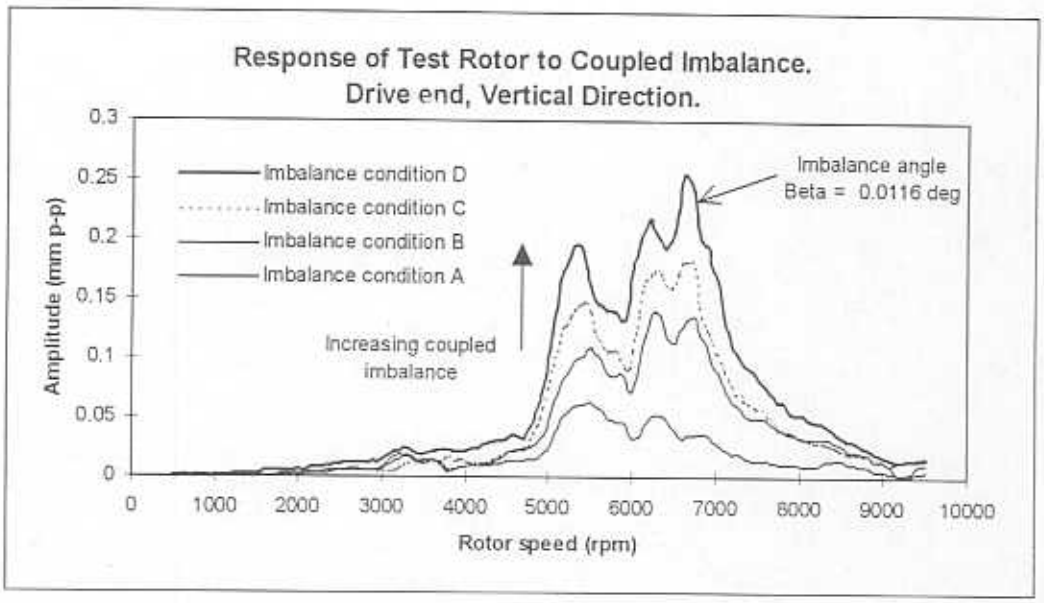

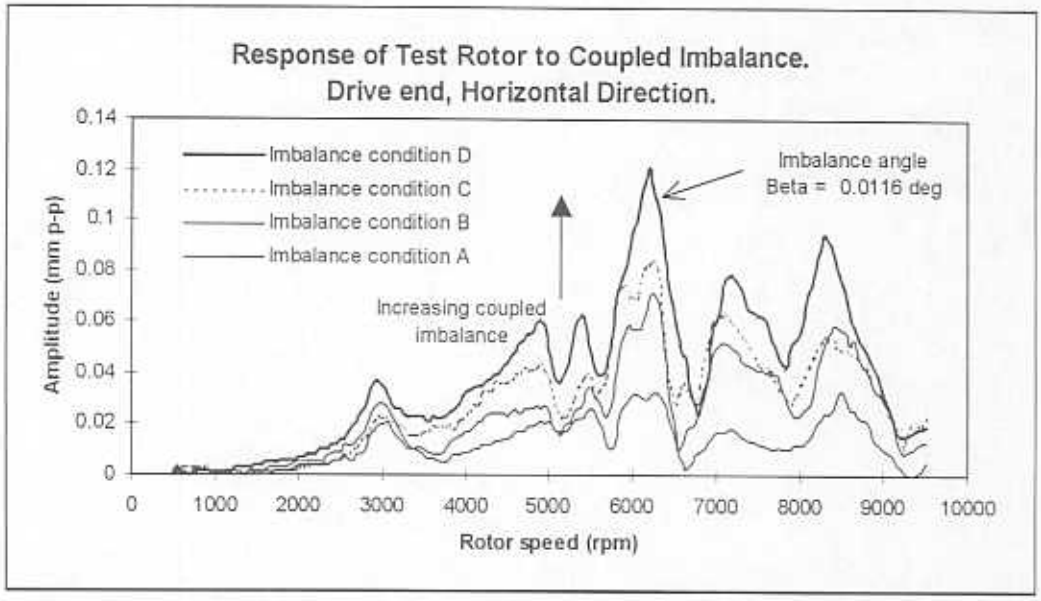

Figure 24. Experimental rotor response to different levels of couple imbalance.
a) Drive end.

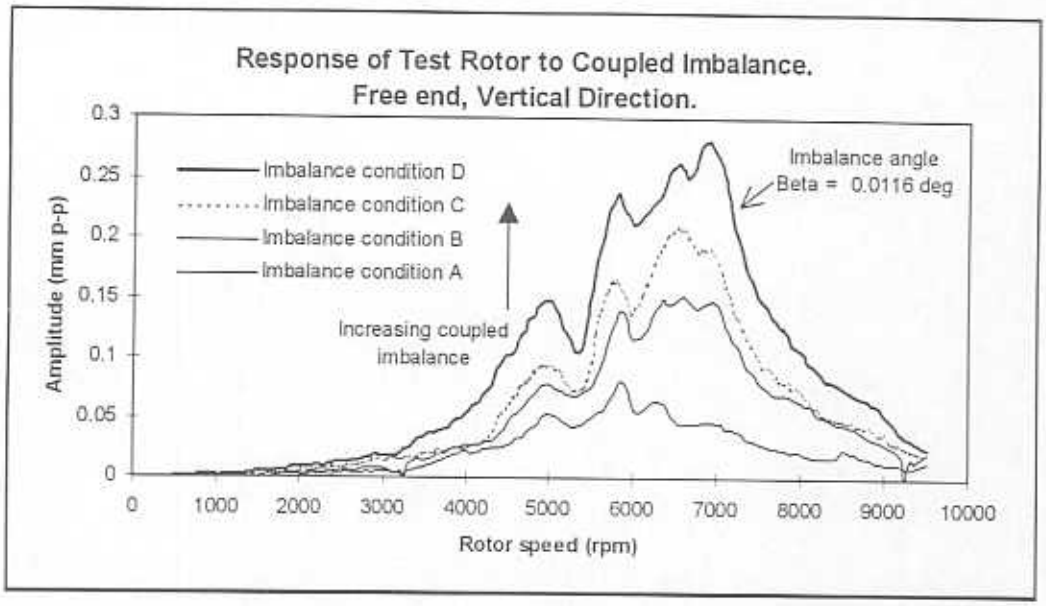

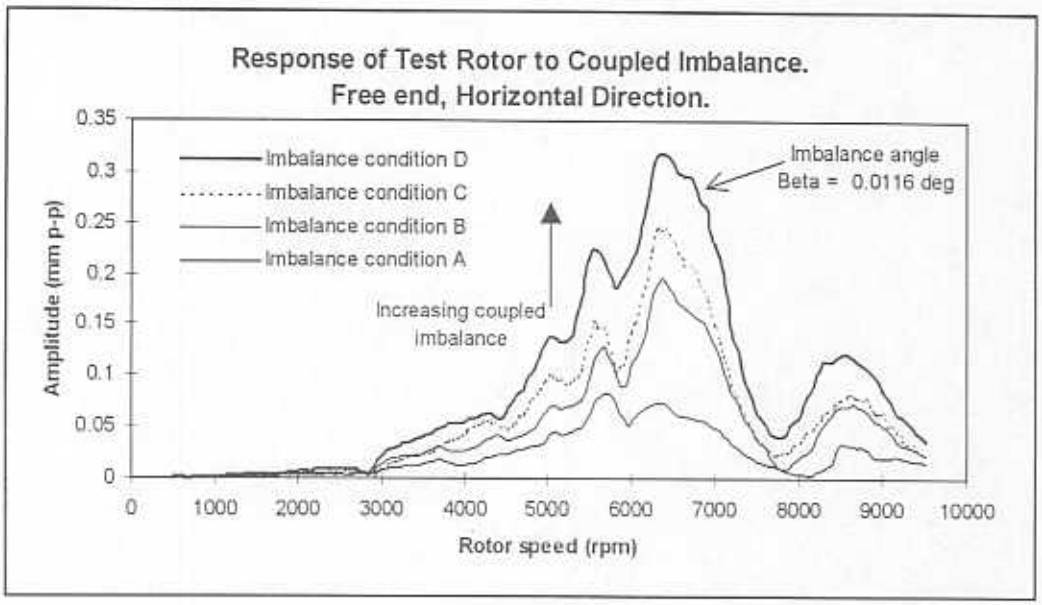

Figure 24. Experimental rotor response to different levels of couple imbalance.
b) Free end.

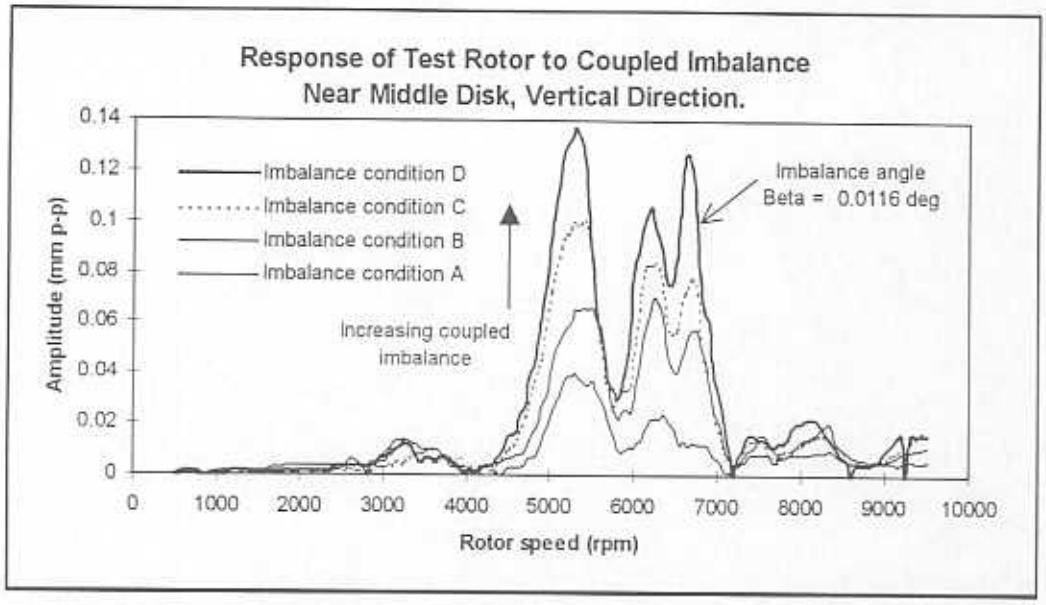

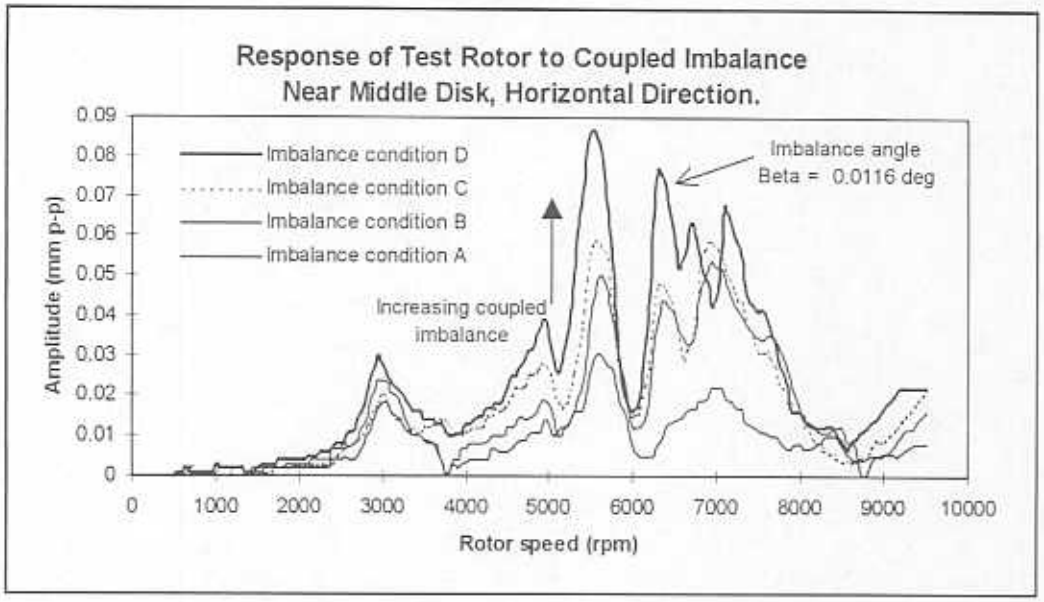

Figure 24. Experimental rotor response to different levels of couple imbalance.
c) Near middle disk.

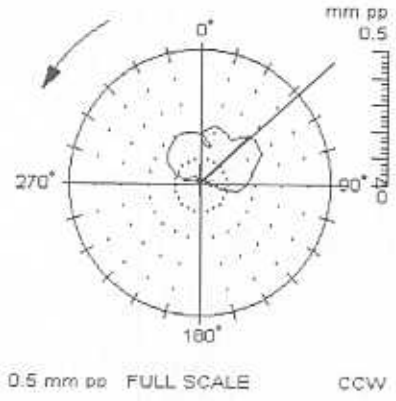

drive end vertical

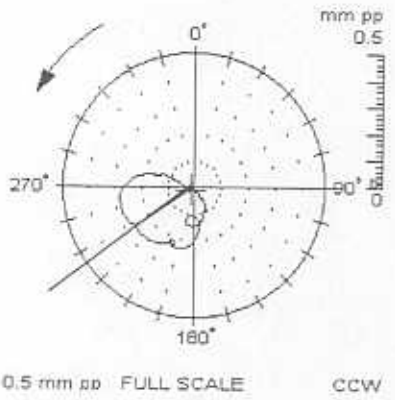

free end vertical

a) Vertical direction. 6600 rpm.

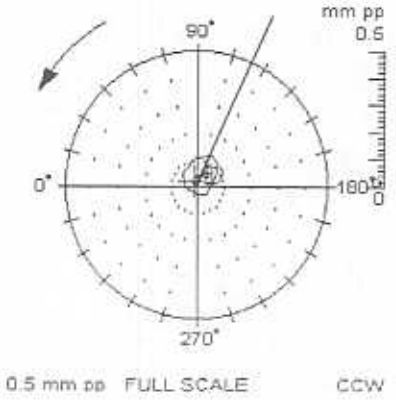

drive end vertical

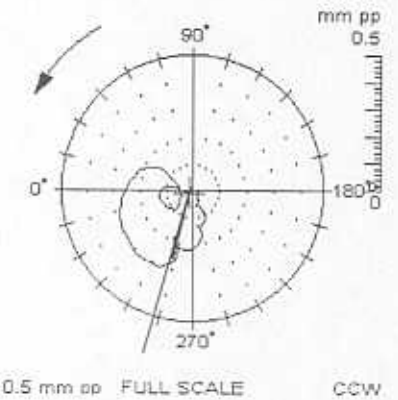

free end vertical

b) Horizontal direction. 6200 rpm.

Figure 25. Polar plots of synchronous rotor response at the free and drive ends. Imbalance condition D (excitation angle $\beta = 0.0116°$).

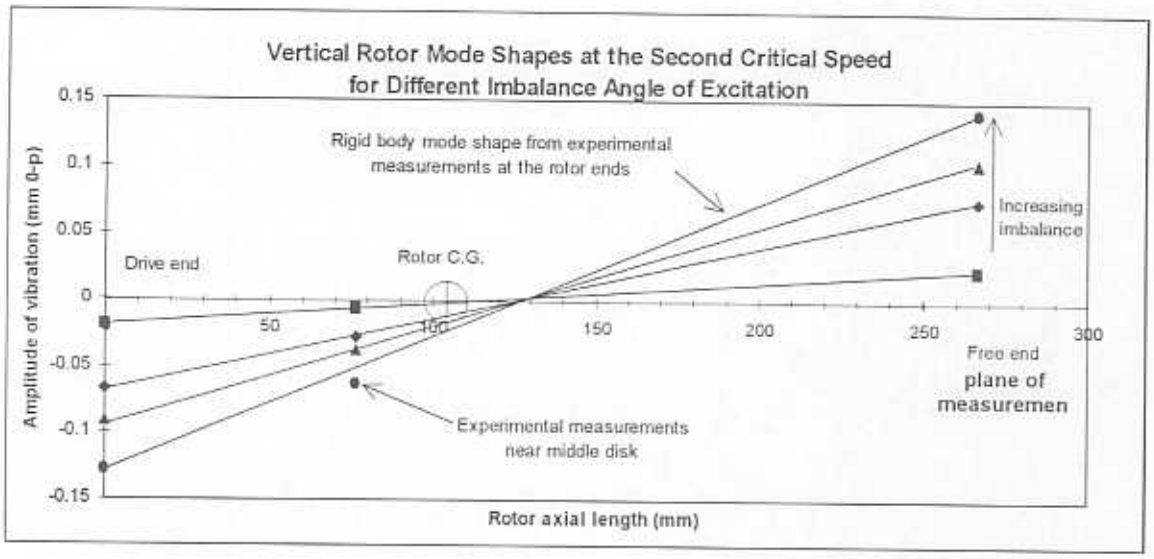

a) Vertical

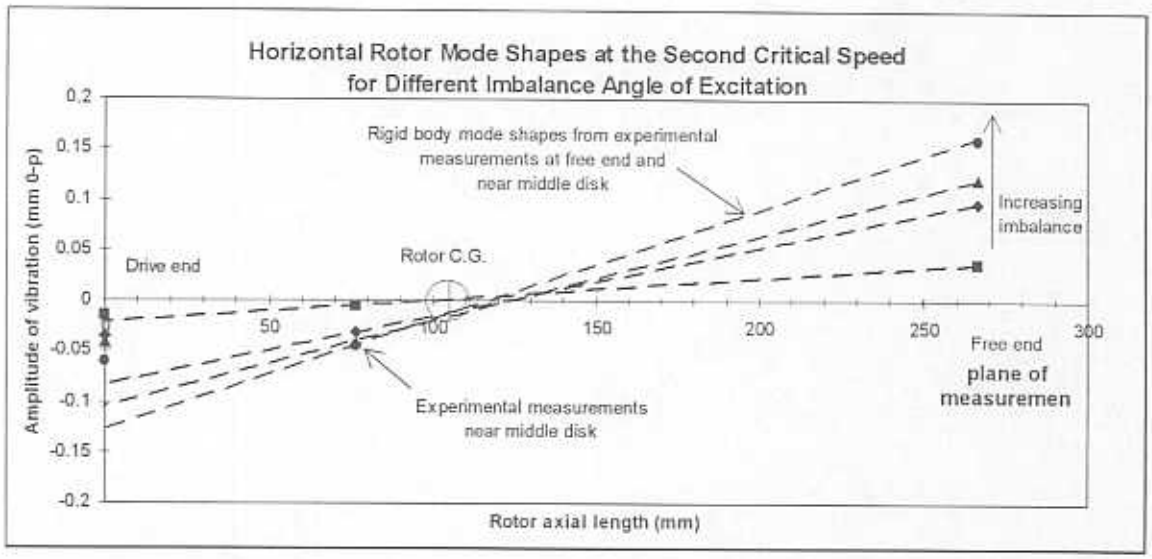

b) Horizontal

Figure 26. Estimated rotor response shapes at the second critical speed (conical mode) for increasing levels of couple imbalance.

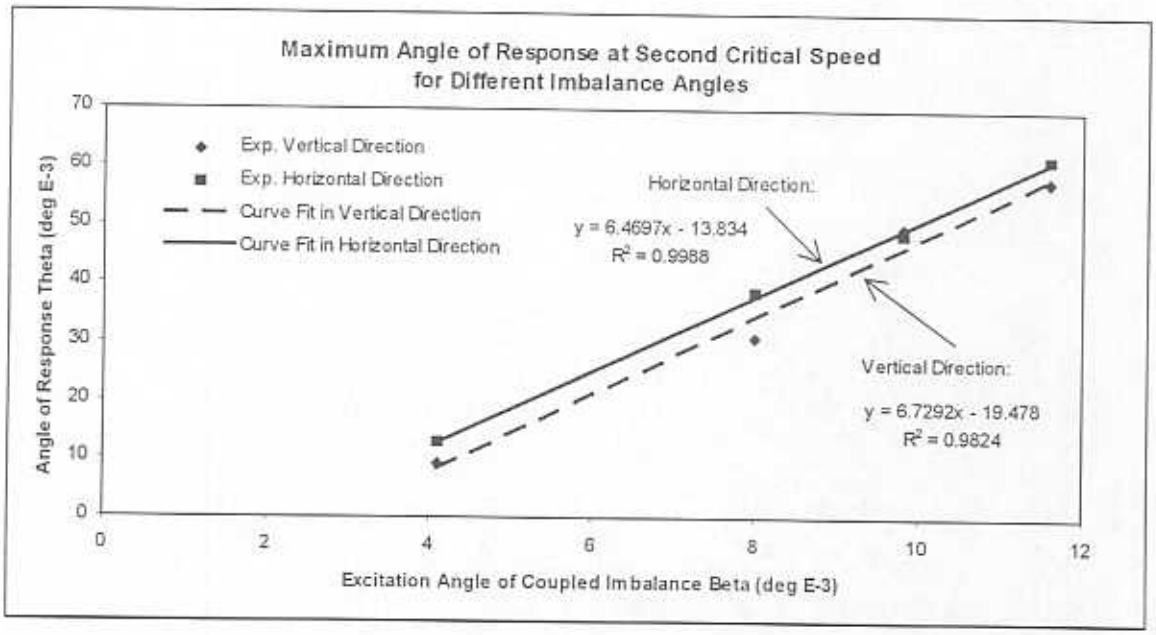

Figure 27. Maximum angle of rotor response at second critical speed versus couple imbalance angle.

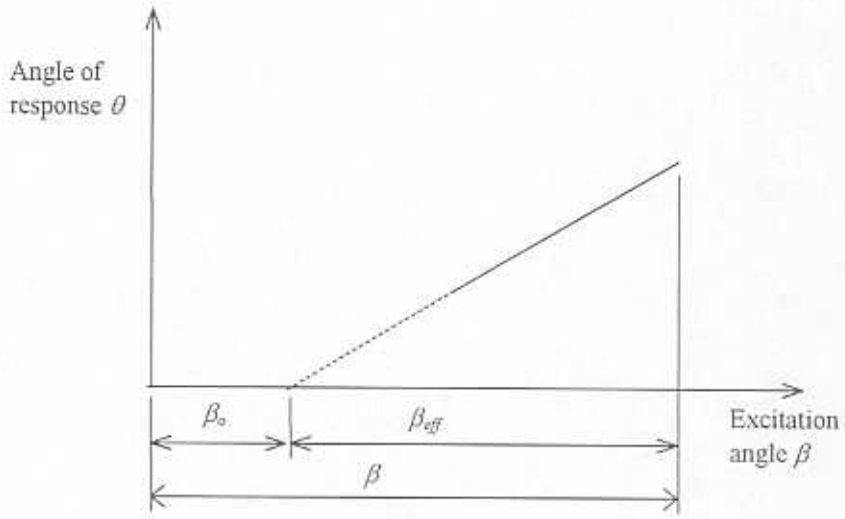

Figure 28. Schematic representation of reduction process to account for the unidentified source of angular excitation at second critical speed.

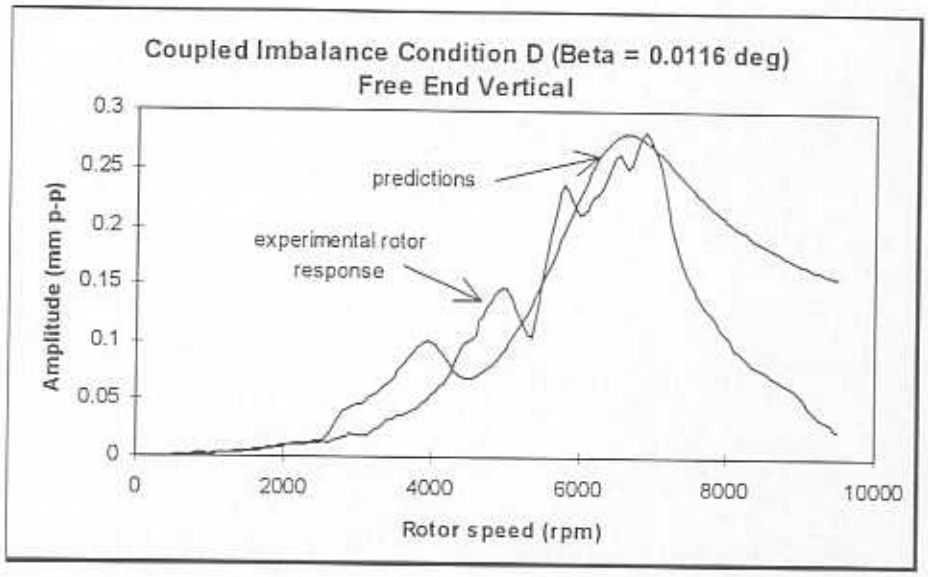

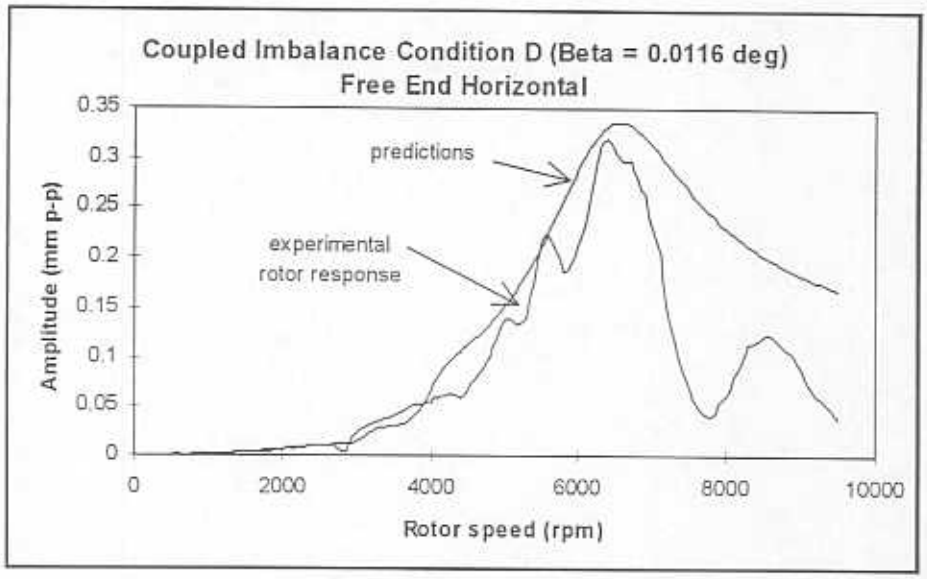

Figure 29a. Comparison of experimental and theoretical rigid rotor response to couple imbalance. ($\beta = 0.0116°$). Free end.

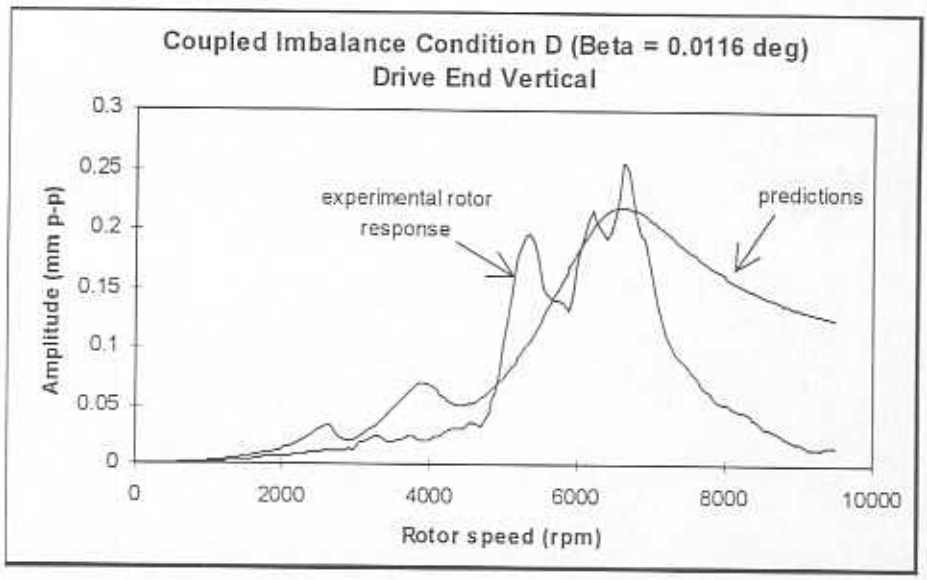

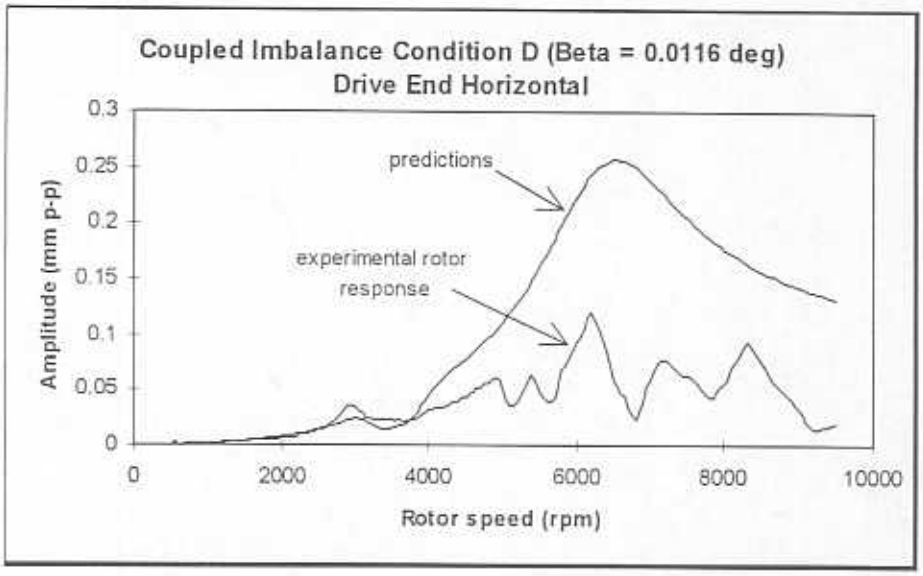

Figure 29b. Comparison of experimental and theoretical rigid rotor response to couple imbalance ($\beta = 0.0116°$). Drive end.

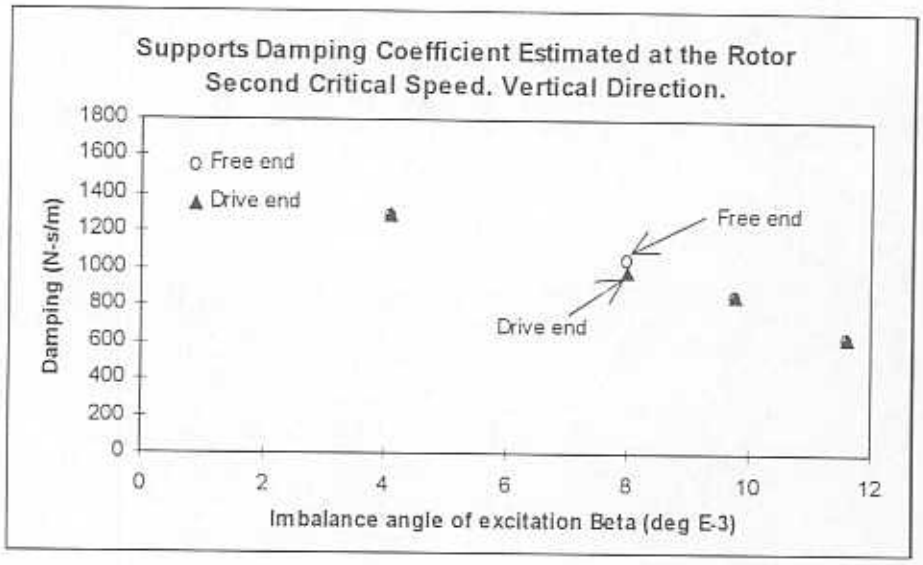

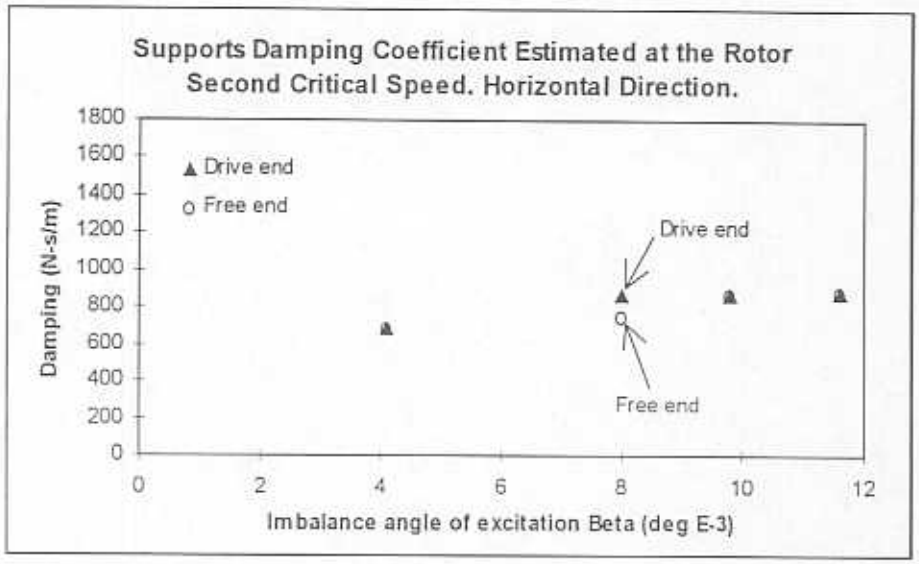

Figure 30. Support damping coefficients versus imbalance angle of excitation β estimated from rotor response to couple imbalance at the second critical speed.

REFERENCES

Botman, M., 1976, "Experiments on Oil-Film Dampers for Turbomachinery," Transactions of the ASME, *Journal of Engineering for Power*, July, pp. 393-399.

Childs, D. W., 1993, "Turbomachinery Rotordynamics", Wiley, pp. 88-92.

Chu, F., and R. Holmes, 1996, "The Effect of Squeeze Film Dampers on the Unbalance Response and Stability of a Flexible Rotor", presented at the International Gas Turbine and Aeroengine Congress and Exhibition, UK, ASME paper No. 96-GT-377.

Dede, M. M., M. Dogan, and R.Holmes, 1985, "The Damping Capacity of a Sealed Squeeze Film Bearing," Transactions of the ASME, *Journal of Tribology*, Vol. 107, July, pp. 411-418.

De Santiago, O., J. Oliveras, and L. San Andres, 1997, "Imbalance Response of a Rotor Supported on Integral Open Ends *SFDs*," Turbomachinery Research Consortium Annual Report, Texas A&M University, TRC-SFD-2-97, April.

Ewins, D. J., 1986, "Modal Testing: Theory and Practice," Research Studies Press, pp. 25-27.

Feder, E., P. N Bansal, and A. Blanco, 1977, "Investigation of Squeeze Film Damper Forces Produced by Circular Centered Orbits," presented at the Gas Turbine Conference, Philadelphia, PA, ASME paper No. 77-GT-27.

Jones, M. G., 1973, "An experimental Investigation of Squeeze Film Hydrodynamics," *Report No. R. 320*, National Gas Turbine Establishment, Ministry of Defense (England), Jan.

Kuzdzal, M. J., and J. F. Hustak, 1996, "Squeeze Film Damper Bearing Experimental VS Analytical Results for Various Damper Configurations," *Proceedings of the 25th Turbomachinery Symposium*, Houston, TX, pp 57-70.

Marmol, R. A., and J. M. Vance, 1978, "Squeeze Film Damper Characteristics for Turbine Engines," Transactions of the ASME, *Journal of Mechanical Design*, Vol. 100, Jan., pp 130-146.

Mohan, S., and E. J. Hahn, 1974, "Design of Squeeze Film Damper Supports for Rigid Rotors," Transactions of the ASME, Transactions of the ASME, *Journal of Engineering for Industry*, Vol. 96, Aug., pp. 976-982.

Murphy, B. T., S. M. Manifold, and J. R. Kitzmiller, 1996, "Compulsator Rotordynamics and Suspension Design," *8th electromotive Launcher Symposium*, Baltimore, MD, April, pp. 21-24.

San Andrés, 1997, "Personal Research Notes".

San Andrés, L., and D. Lubell, 1996, "Unbalance Response of a Test Rotor Supported on Squeeze Film Dampers," ASME paper 97-GT-12.

San Andrés, L., and J. M. Vance, 1984, "Finite Length Correction Factors for Squeeze Film Dampers Executing Circular Centered Orbits - With Effects of End Seals and Fluid Inertia Approximately Accounted for," Turbomachinery Research Consortium Report No. 107, Texas A&M University.

Simandiri, S., and E. J. Hahn, 1979, "Experimental Evaluation of the Predicted Behavior of Squeeze Film Bearing Supported Rigid Rotors," *Journal Mechanical Engineering Science*, Vol 21, No. 6, pp. 439-451.

Thomsen, K. K., and H. Andersen, 1974, "Experimental Investigation of a Simple Squeeze Film Damper," Transactions of the ASME, *Journal of Engineering for Industry*, Vol. 96, May, pp 427-430.

Tonnesen, J., 1976, "Experimental Parametric Study of a Squeeze Film Bearing," Transactions of the ASME, *Journal of Lubrication Technology*, Vol. 98, April, pp. 206-213.

Vance J. M., and A. J. Kirton, 1974, "Preliminary Investigation of the Dynamic Force Response Coefficients for Squeeze Film Bearing Dampers," *US Army Research Office*, Grant Number DAHCO4-74-60048, Nov.

Vance, J. M., and A. J. Kirton, 1975, "Experimental Measurement of the Dynamic Force Response of a Squeeze Film Bearing Damper," Transactions of the ASME, *Journal of Engineering for Industry*, Vol. 97, Nov., pp. 1282-1290.

Zeidan, F. Y., 1995, "Applications of Squeeze Film Dampers," *Turbomachinery International*, Sept/Oct., pp. 50-53.

Zeidan, F. Y., L. San Andrés, J. M. Vance, 1996, "Design and application of squeeze film dampers in rotating machinery," *Proceedings of the 25th Turbomachinery Symposium*, Houston, TX, pp 169-188.

APPENDIX A
IMBALANCE RESPONSE OF A RIGID ROTOR ON ELASTIC SUPPORTS

Governing Equations

Consider a rigid body (rotor) in rotational and translational motion. The linear momentum equations are (Childs, 1993):

$$m\ddot{R}_X = f_X + F_X + ma_X\dot{\phi}^2 + ma_Y\ddot{\phi}$$
$$m\ddot{R}_Y = f_Y + F_Y + ma_Y\dot{\phi}^2 + ma_X\ddot{\phi}$$

where

$$a_X = a_x\cos\phi + a_y\sin\phi$$
$$a_Y = a_x\sin\phi + a_y\cos\phi$$

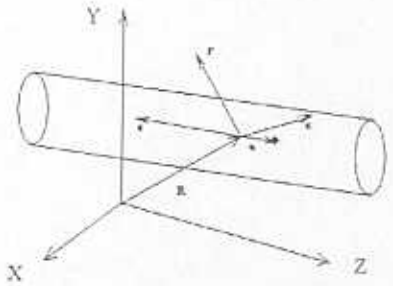

are given by the Euler angles,
(x,y,z) is a coordinate system fixed to the rigid body;
(X,Y,Z) is a fixed (inertial) coordinate system in space;
the vector R locates the origin of the rotating system;
the vector a locates the center of mass of the body with respect to the rotating coordinate system;
(f_x, f_y) and (F_x, F_y) are the components of the external and bearing forces acting on the rigid body;
ϕ is the rotational speed of the body about z;
and m is the rotor mass.

The moment of momentum equations about the origin of the inertial coordinate system are (Childs, 1993):

$$J\ddot{\beta}_X = m_X + M_X - \bar{J}\dot{\beta}_Y\dot{\phi}^2 - J_{YZ}\dot{\phi}^2 + J_{XZ}\ddot{\phi}$$
$$J\ddot{\beta}_Y = m_Y + M_Y + \bar{J}\dot{\beta}_X\dot{\phi}^2 + J_{XZ}\dot{\phi}^2 + J_{YZ}\ddot{\phi}$$

where J and $\bar{J}$ and are the diametrical (transverse) and polar moment of inertia, (m_x, m_y) and (M_x, M_y) are the components of the external applied moment and the bearing reaction moments acting on the body.

The stationary components of the products of inertia related to their rotor-fixed components are:

$$J_{XZ} = J_{xz}\cos\phi - J_{yz}\sin\phi$$
$$J_{YZ} = J_{xz}\sin\phi + J_{yz}\cos\phi$$

where J_{xz} and J_{yz} are constant in time.

Evaluation of Bearing Forces

The bearing reaction forces and moments in the X-Z plane (F_x and M_y), in terms of the bearing stiffness and damping coefficients are as follow:

$$\begin{bmatrix} F_X \\ M_Y \end{bmatrix} = -[K_X]\begin{bmatrix} R_X \\ \beta_Y \end{bmatrix} - [C_X]\begin{bmatrix} \dot{R}_X \\ \dot{\beta}_Y \end{bmatrix}$$

where the stiffness and damping matrices are:

$$[K_X]=\begin{bmatrix} (K_{xxL}+K_{xxR}) & (K_{xxL}d_L-K_{xxR}d_R) \\ (K_{xxL}d_L-K_{xxR}d_R) & (K_{xxL}d_L^2+K_{xxR}d_R^2) \end{bmatrix}$$

and

$$[C_X]=\begin{bmatrix} (C_{xxL}+C_{xxR}) & (C_{xxL}d_L-C_{xxR}d_R) \\ (C_{xxL}d_L-C_{xxR}d_R) & (C_{xxL}d_L^2+C_{xxR}d_R^2) \end{bmatrix}$$

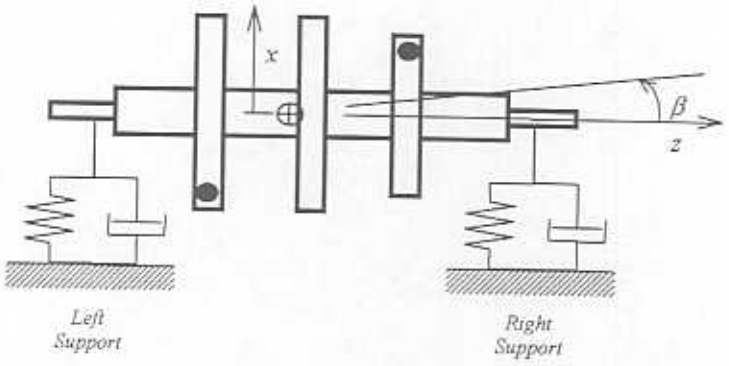

where K is stiffness, C is damping, d is the distance to the rotor $C.G.$ and the subindexes xx denote direct stiffness and damping in the X direction, while R and L stand for right and left bearing. The bearing reaction forces and moments in the Y-Z plane are defined in the same way.

Equations of Motion in Matrix Form

Substituting the definitions of the bearing forces into the momentum equations and representing them in matrix form yields:

Motion on the X-Z plane:

$$\begin{bmatrix} m & 0 \\ 0 & J \end{bmatrix}\begin{bmatrix} \ddot{R}_X \\ \ddot{\beta}_Y \end{bmatrix}+[K_X]\begin{bmatrix} R_X \\ \beta_Y \end{bmatrix}+[C_X]\begin{bmatrix} \dot{R}_X \\ \dot{\beta}_Y \end{bmatrix}=\begin{bmatrix} f_X \\ m_Y \end{bmatrix}+\begin{bmatrix} 0 \\ \dot{\phi}\bar{J}\dot{\beta}_X \end{bmatrix}+\begin{bmatrix} ma_X\dot{\phi}^2+ma_Y\ddot{\phi} \\ \dot{\phi}^2J_{XZ}+\ddot{\phi}J_{YZ} \end{bmatrix}$$

Motion on the Y-Z plane:

$$\begin{bmatrix} m & 0 \\ 0 & J \end{bmatrix}\begin{bmatrix} \ddot{R}_Y \\ \ddot{\beta}_X \end{bmatrix}+[K_Y]\begin{bmatrix} R_Y \\ \beta_X \end{bmatrix}+[C_Y]\begin{bmatrix} \dot{R}_Y \\ \dot{\beta}_X \end{bmatrix}=\begin{bmatrix} f_Y \\ m_X \end{bmatrix}+\begin{bmatrix} 0 \\ \dot{\phi}\bar{J}\dot{\beta}_Y \end{bmatrix}+\begin{bmatrix} ma_Y\dot{\phi}^2+ma_X\ddot{\phi} \\ \dot{\phi}^2J_{YZ}+\ddot{\phi}J_{XZ} \end{bmatrix}$$

If the rotor runs at constant speed, $\phi=\omega t$, $\dot{\phi}=\omega$, $\ddot{\phi}=0$. Reordering terms in the above equations and supposing no external forces yields:

Motions on the X-Z plane:

$$[M]\begin{bmatrix} \ddot{R}_X \\ \ddot{\beta}_Y \end{bmatrix}+[K_X]\begin{bmatrix} R_X \\ \beta_Y \end{bmatrix}+[C_X]\begin{bmatrix} \dot{R}_X \\ \dot{\beta}_Y \end{bmatrix}+\omega\begin{bmatrix} 0 & 0 \\ 0 & -\bar{J} \end{bmatrix}\begin{bmatrix} \dot{R}_X \\ \dot{\beta}_X \end{bmatrix}=\omega^2\begin{bmatrix} ma_X \\ J_{XZ} \end{bmatrix}$$

Motions on the Y-Z plane:

$$[M]\begin{bmatrix} \ddot{R}_Y \\ \ddot{\beta}_X \end{bmatrix}+[K_Y]\begin{bmatrix} R_Y \\ \beta_X \end{bmatrix}+[C_Y]\begin{bmatrix} \dot{R}_Y \\ \dot{\beta}_X \end{bmatrix}+\omega\begin{bmatrix} 0 & 0 \\ 0 & -\bar{J} \end{bmatrix}\begin{bmatrix} \dot{R}_Y \\ \dot{\beta}_Y \end{bmatrix}=\omega^2\begin{bmatrix} ma_Y \\ J_{YZ} \end{bmatrix}$$

Defining new matrices:

$$\overline{M}=\begin{bmatrix}[M] & \overline{0}\\ \overline{0} & [M]\end{bmatrix},\ \overline{K}=\begin{bmatrix}[K_X] & \overline{0}\\ \overline{0} & [K_Y]\end{bmatrix},\ \overline{C}=\begin{bmatrix}[C_X] & \overline{0}\\ \overline{0} & [C_Y]\end{bmatrix},\ G=\begin{bmatrix}0 & 0 & 0 & 0\\ 0 & 0 & 0 & -J\\ 0 & 0 & 0 & 0\\ 0 & -J & 0 & 0\end{bmatrix}$$

$$\overline{0}=\begin{bmatrix}0 & 0\\ 0 & 0\end{bmatrix},\quad Z=\left[R_X,\beta_Y,R_Y,\beta_X\right]^T$$

the above equations can be combined into a single one:

$$\overline{M}\ddot{Z}+\overline{K}Z+\left[\overline{C}+\omega G\right]\dot{Z}=\omega^2\begin{bmatrix}ma_X\\ J_{XZ}\\ ma_Y\\ J_{YZ}\end{bmatrix} \qquad (1)$$

Eigenanalysis

The eigenvalues are speed dependent (term ωG) and are obtained by making zero the right hand side of the equation (1).

$$\overline{M}\ddot{Z}+\overline{K}Z+\left[\overline{C}+\omega G\right]\dot{Z}=0$$

The eigenanalysis yields 2x4 eigenvalues of the form $[\lambda_i \pm j\omega_{di}]$, $i = 1,\ldots,4$ corresponding to the eigenvalues for 2 translation motions (X-Z and Y-Z planes) and 2 rotations (about X and Y axis).

The Mathcad® sheet "eigenanalysis of rigid rotor" performs the eigenanalysis of the rigid rotor mounted on the integral SFDs. Mass and length are measured values, the moments of inertia are from the XLRotor® model and the values of stiffness and damping are experimentally estimated values.

Steady State Rotor Response

At steady state, the term

$$\omega^2\begin{bmatrix}ma_X\\ J_{XZ}\\ ma_Y\\ J_{YZ}\end{bmatrix}=\omega^2\begin{bmatrix}m(a_x\cos\omega t-a_y\sin\omega t)\\ J_{xz}\cos\omega t-J_{yz}\sin\omega t\\ m(a_y\cos\omega t+a_x\sin\omega t)\\ -J_{yz}\cos\omega t-J_{xz}\sin\omega t\end{bmatrix}=\omega^2\left[f_c\cos\omega t+f_s\sin\omega t\right]$$

where

$$f_c=\left[ma_x,J_{xz},ma_y,-J_{yz}\right]^T$$
$$f_s=\left[-ma_y,-J_{yz},ma_x,-J_{xz}\right]^T$$

Let

$$Z=Z_c\cos\omega t+Z_s\sin\omega t$$

where Z_c and Z_s are real valued matrixes.

Taking the correspondent derivatives of Z, equation (1) can be split into 2 equations (one for the sine and one for the cosine terms f_c and f_s). Multiplying the equation corresponding to f_s by the imaginary unit j and adding up the equations again, yields the single equation:

$$\left[\overline{K}+\omega^2\,\overline{M}\right]\left[Z_c+j\,Z_s\right]-\omega\left[\overline{C}+\omega G\right]\left[jZ_c-Z_s\right]=\omega^2\left[f_c+f_s\right];$$

if $\hat{Z}=Z_c+j\,Z_s$ and $\hat{f}=f_c+j\,f_s$

$j\hat{Z}=j\,Z_c-Z_s$

and

$$\left[\overline{K}-j\,\omega\left[\overline{C}+\omega G\right]-\omega^2\,\overline{M}\right]\hat{Z}=\omega^2\,\hat{f};$$

Rename:

$$\hat{K}_d=\left[\overline{K}-j\,\omega\left[\overline{C}+\omega G\right]-\omega^2\,\overline{M}\right];$$

then:

$$\hat{Z}=\omega^2\hat{K}_d^{-1}\,\hat{f}$$

and the response in real coordinates is:

$$Z=\frac{1}{2}\left[\hat{\bar{Z}}\,e^{j\omega t}+\hat{Z}\,e^{-j\omega t}\right]$$

Recall that the above is the response of the rotor at the *C.G.* The response of the rotor at different locations can be recovered by:

$$A_X=\sqrt{(X_c)^2+(X_s)^2} \qquad A_Y=\sqrt{(Y_c)^2+(Y_s)^2}$$

where

$$X_c=Re(R_X+d\,\beta_Y)$$
$$X_s=Im(R_X+d\,\beta_Y)$$
$$Y_c=Re(R_Y+d\,\beta_X)$$
$$Y_s=Im(R_Y+d\,\beta_X)$$

and d is the distance to the plane of the response from the *C.G.*
Recall that

$$Z=\left[R_X,\beta_Y,R_Y,\beta_X\right]^T$$

The phase angles of the response are:

$$tan\,\phi_X=\frac{X_s}{X_c} \qquad tan\,\phi_Y=\frac{Y_s}{Y_c}$$